Chapter 3
Universal Properties of Relaxation and Diffusion in Interacting Complex Systems

3.1 Introduction

This book is principally concerned with the dynamics of glass forming in relation to the glass transition problem. Glass-forming substances and systems are usually constituted of densely packed structural units interacting with anharmonic potentials. Consequently, the view of the author is that relaxation and diffusion of glassformers has to be treated with emphasis on the many-body nature of the irreversible process. At any fixed temperature T and pressure P, the dynamics and properties originating from the many-body relaxation is already a challenging problem to be solved first, before the changes observed on varying T and P are to be accounted for. Examples taken from some of the properties of neat and homogeneous glassformers at fixed T and P discussed in Chapter 2 include the following: (i) the Kohlrausch α-correlation function $\exp\left[-(t/\tau_\alpha)^{1-n}\right]$ for the structural α-relaxation when $\tau_\alpha >> 1$ps; (ii) the Kohlrausch α-correlation function replaced by the linear exponential function at times shorter than t_c (≈ 2 ps for molecular glassformers, and much longer for colloidal particle suspensions); (iii) the $Q^{-2/(1-n)}$ scattering vector dependence of τ_α; (iv) the appearance of the universal Johari-Goldstein (JG) relaxation strongly connected to the α-relaxation as seen from NMR study and by the ratio of its relaxation time τ_{JG} to τ_α correlated with n and approximately given by the relation $\log(\tau_\alpha/\tau_{JG}) = n(\log\ \tau_\alpha + 11.7)$ for molecular glassformers; and (iv) caged relaxation at shorter times exemplified by the nearly constant loss (NCL) which is terminated at longer times of the order of τ_{JG} by the universal JG relaxation. These properties at fixed T and P, plus more discussed in Chapter 2 apparently all controlled by n, are indications of the manifestation of many-body relaxation, and most challenging to be solved.

Glass transition compounds the difficulty of the problem by requiring further consideration of the change of the many-body relaxation with changes of T and P. The latter bring in changes of their conjugate thermodynamic variables including entropy S and specific volume V. All these changes of T, P, V, and S force modification of the many-body relaxation and spawn more conspicuous properties such as (i) decrease of V (or free volume) and increase of S (or configuration entropy S_c); (ii) VFTH temperature dependence (including its inadequacy) of τ_α; (iii) T_g-scaled

K.L. Ngai, *Relaxation and Diffusion in Complex Systems*, Partially Ordered Systems,
DOI 10.1007/978-1-4419-7649-9_3, © Springer Science+Business Media, LLC 2011

T dependence of τ_α or "fragility," (iv) the breakdown of the Stokes-Einstein (SE) relation and the Debye-Stokes-Einstein (DSE) relation (onset and T dependence), and (v) T dependence of n. These are traditionally the properties of glassformers that researchers have exclusively focused on to construct theories of glass transition such as the free volume theory, the configuration entropy theory of Adam-Gibbs, their generalizations, and some modern approaches. These theories can explain the rapid increase of τ_α on cooling and compressing leading to glass transition but leave out the rich dynamic properties of the α-relaxation untouched, not even those at fixed T and P that are worth consideration (see Sections 2.2.1–2.2.5 on α-relaxation). The multiple subsections in Sections 2.3 have presented many different experimental facts demonstrating that the JG β-relaxation is universal, fundamental, and inseparable from any consideration of the structural α-relaxation. None of the traditional theories of glass transition have considered the JG β-relaxation and its connection to the α-relaxation. Neither are the more recent theories including those bringing into consideration the dynamic heterogeneous nature of the α-relaxation from the breakdown of SE and DSE relations, nor are the theory focusing on the fast relaxation while molecules are still caged. Here, I remind the readers of one of the many examples of the connection between the JG β-relaxation and the α-relaxation discussed in Section 2.3. This example is the invariance of the α-dispersion (or n) as well as the ratio τ_α/τ_{JG} to various combinations of T and P while keeping τ_α constant. Also, both τ_α and τ_{JG} are functions of the *same* product variable TV^γ. These new experimental findings provide further evidence for the many-body nature of the α-relaxation and the universal JG β-relaxation is its precursor and originator. However, none of the past and recent theories mentioned above has provided explanation for these new and important findings. As far as the author knows, the coupling model (CM) is the only model having the equivalent of the JG β-relaxation in the primitive relaxation, the device via the CM equation (2.68) to capture and explain many of the effects of many-body relaxation on the structural α-relaxation, and the capability of addressing all the dynamic processes in order of increasing time from caged relaxation (NCL), JG secondary to the structural α-relaxation, and their inter-relations.

If the above discussion restricted to glass-forming materials is not sufficient to support the call for incorporating many-body relaxation into the theory of glass transition, I shall bring in some dynamic properties of other interacting systems which are not glass forming or in which the interest of the process in the system is not in glass transition per se. If the physics of many-body relaxation and diffusion is fundamental, the properties of the dynamics manifested will show up analogously in these various non-glass-forming interacting systems. It is therefore a worthwhile undertaking to broaden the study of glass-forming materials by bringing in these other processes in different systems. For the past three decades, the author has actively engaged in the study of relaxation and diffusion in several fields which are unrelated to the glass transition problem. This is partly motivated by the CM, which is supposedly applicable to relaxation in many-body interacting systems in general. But, the higher motivation is to explore the possibility that *relaxation in interacting many-body systems exhibits universal properties*. If indeed the properties of many-body relaxation are universal, it would be an important discovery that has

immediate impact on various scientific disciplines. To accomplish this goal, we can take advantage of the properties of the α-relaxation and JG β-relaxation of glassformers matching the concepts and predictions of CM discussed in Chapter 2 by using them as guides to look for parallels in other interacting many-body systems.

First is the crossover of the correlation function from linear exponential relaxation $\exp(-t/\tau_0)$ to Kohlrausch stretched exponential relaxation $\exp\left[-(t/\tau)^{1-n}\right]$ in a neighborhood of some time t_c. Second is to find the equivalent of the primitive relaxation (or the analogue of the JG relaxation in glassformers) either directly or by identification with a feature in the experiment data or molecular dynamics simulation. Third is to validate the relation between the primitive relaxation time τ_0 and the observed many-body relaxation time τ given by the equation

$$\tau = [t_c^{-n}\tau_0]^{\frac{1}{1-n}}, \tag{3.1}$$

and the relation becomes quantitative if t_c is known. Even without knowing the exact value of t_c, the predicted dependence of τ on various variables U given by

$$\tau\,(U) \propto [\tau_0\,(U)]^{1/(1-n)} \tag{3.2}$$

can be tested against experiment. In some cases, dependences of τ on more than one variable U are predicted by the same n, thus making the test by experiment even more stringent and satisfying. The dependence of τ_0 on U is not anomalous because it is the relaxation time of simple (not many-body) relaxation and either is known from basic theory or can be independently determined by experiment or simulations in situations where many-body effects are eliminated. If successful, Eq. (3.2) serves to explain the observed dependence of τ on U, which is often found to be anomalous in other interacting systems similar to those we have seen in glassformers in Chapter 2. The success can be viewed as evidence of a strong connection between τ and τ_0, like that found between τ_α and τ_{JG} or τ_0 (since $\tau_{JG} \approx \tau_0$) in glassformers.

Because the anomalous dependence of $\tau(U)$ comes from raising $\tau_0(U)$ to the superlinear power $1/(1-n)$ in Eqs. (3.1) and (3.2), the degree of the abnormality increases with increasing n. This offers multiple checks of Eqs. (3.1) and (3.2) by experiment by increasing or decreasing the interaction even in the same system. Depending on the system, it can be accomplished in different ways such as increasing or decreasing concentration, temperature, association, chemical cross-links, changing the other component in binary mixtures, and densification.

Indeed, my collaborators and I as well as other researchers independently have found anomalous dynamic properties in interacting systems which are analogues to those of glassformers discussed in Chapter 2. In particular, the dispersion of the relaxation or the diffusion governs or correlates with the anomalous properties. The collection of experimental data in various systems of different fields shows analogous dynamic properties and hence is a strong evidence supporting the presence of the many-body relaxation in interacting systems and the dynamics manifested is universal and fundamental. Moreover, these analogous anomalous properties can be explained by the CM.

Complete and detailed description of this large collection of data cannot be made in this book because this would make the size of this book unduly large. Therefore selected sets of data are presented, and most of them are just briefly described and the corresponding explanations by the CM given here are also abbreviated. References are given for the interested reader to look for the details. A few sets of data have been presented before in Chapter 2 for specific purpose, not the same as in this chapter, which is to demonstrate the universal relaxation properties of different interacting systems.

Attempt is made to present the similar properties in other systems as much as possible in about the same order as introduced in Chapter 2 for the relaxation processes in glass-forming materials and systems. This way makes it easier for the reader to find and collate the properties to correspond to the glass-forming systems, all of which are the vestige of many-body dynamics in relaxation of interacting systems with glass-forming substances as a special class.

3.2 Universal Properties

3.2.1 The Kohlrausch Stretched Exponential Correlation Function $\exp[-(t/\tau)^{1-n}]$

Materials of interest in research on relaxation and diffusion these days vary greatly in chemical structure and physical type. However, many of them share one common characteristic and that is the relaxing or diffusing units have mutual interactions with each other. The simplest class consists of relaxation and diffusion processes in bulk materials that involve identical interacting units with no other complications, such as identical molecules in glass-forming viscous liquid, colloidal particles nearly all of the same size in colloidal suspensions [141–143], identical mobile ions in crystalline or polycrystalline [283, 1060, 1482–1486], vitreous, or molten ionic conductors [54–56, 115(b), 147, 232, 279–295, 1056–1059], and a monodisperse entangled polymer melts where all polymer chains have the same repeat unit and are of the same length [359, 360, 837]. In these ideal cases, the time correlation function of the many-body relaxation is well described by the Kohlrausch function as in the case of bulk and neat glassformers. Liquid or glassy state is not required to have the Kohlrausch correlation function as exemplified by the Li ion motion in polycrystalline $LiAlSi_2O_6$ (β-spodumene) [283, 1485, 1060] and in the crystalline ion conductors such as Na β-alumina [1486], $Li_{0.18}La_{0.61}TiO_3$ (LLTO) [1483], and yttria-stabilized zirconia (YSZ), an oxygen ion conductor of fluorite structure used commercially as electrolytes in solid oxide fuel cells [1482, 1484]. These crystalline cases elucidate that ion-ion interaction rather than randomness is principally responsible for the slowing and stretching of the relaxation.

However, one must be aware that some materials and systems have built-in disorder, randomness, or fluctuation. Examples include concentration fluctuations in miscible blends of two different liquids or polymers, random copolymers, ionic

conductors containing two different kinds of mobile ions, and polydisperse polymer melts with a broad distribution of chain lengths. Spatial heterogeneity of various kinds includes liquid or polymer nanoconfined by wall, free-standing, or supported ultrathin polymer films, repeat units of a cross-linked (semicrystalline) polymer located at different distances from the junction points (the crystalline-amorphous boundaries), and density fluctuations present in the non-equilibrium glassy state. In these more complicated cases, the frequency dispersion of the observed relaxation is broadened by these factors in addition to many-body relaxation originating from interactions. The resulting dispersions often deviate from those of the Kohlrausch function. In the event when it can be forced fitted by a Kohlrausch function, the value of n appearing in the exponent $\beta \equiv (1 - n)$ of the Kohlrausch function does not reflect that coming exclusively from many-body relaxation and should not be used in Eqs. (3.1) and (3.2) to make predictions. Bearing this caution in mind, we can also consider the more complicated materials where there is mutual interaction between the units. We are not interested in relaxation of systems where the dispersions are solely due to disorder, randomness, or fluctuation, because no new physics is involved.

3.2.1.1 Mean-Square Displacement of Diffusion in Interacting Systems

Glass-Forming Systems

For systems exhibiting diffusion in space, many-body effects are more explicitly shown by the mean-square displacement (MSD) $< r^2(t) >$ as a function of time. Normal diffusion will have $< r^2(t) >= 6Dt$ for all times, a result that follows from exponential correlation function for diffusion or random walk. The actual $< r^2(t) >$ of interacting systems deviates from this simple time dependence. Previously in Section 2.2.1.1, the subdiffusion having a fractional power law dependence of $< r^2(t) > \propto t^{1-n}$ has been shown to be present at times before $< r^2(t) >$ crosses over to the terminal steady-state diffusion at long times and the dependence $< r^2(t) >= 6Dt$ takes over. Such is in the case of the results of solvent in polymer solutions from dynamic lattice liquid simulation [327, 328] (see Fig. 7) and also of the dynamic light-scattering data of colloidal particle suspensions with $\phi = 0.465$ (see Fig. 9). Preceding the subdiffusion is the primitive diffusion with $< r^2(t) >= 6D_0t$ in these two systems. From the transition from primitive to subdiffusion, one can determine the crossover time t_c of the coupling model (CM). In terms of correlation times τ and τ_0 and the elementary diffusion length R, we have $D = R^2/\tau$ and $D_0 = R^2/\tau_0$, respectively. The CM equations (2.12) or (2.14) between τ and τ_0 provide a relation between D and D_0.

Here we add the results from the molecular dynamics simulation of glass-forming binary Lennard-Jones particles by Donati et al. [321]. The $< r^2(t) >$ data from this paper are shown in Fig. 275. At the highest temperature of 0.5495 as well as the lowest temperature of 0.4510 (in L-J unit), subdiffusion having the fractional power law dependence of $< r^2(t) > \propto t^{1-n}$ with $(1 - n) = 0.77$ appears at earlier times before the terminal free diffusion with $< r^2(t) >= 6Dt$ takes over. The onset time of

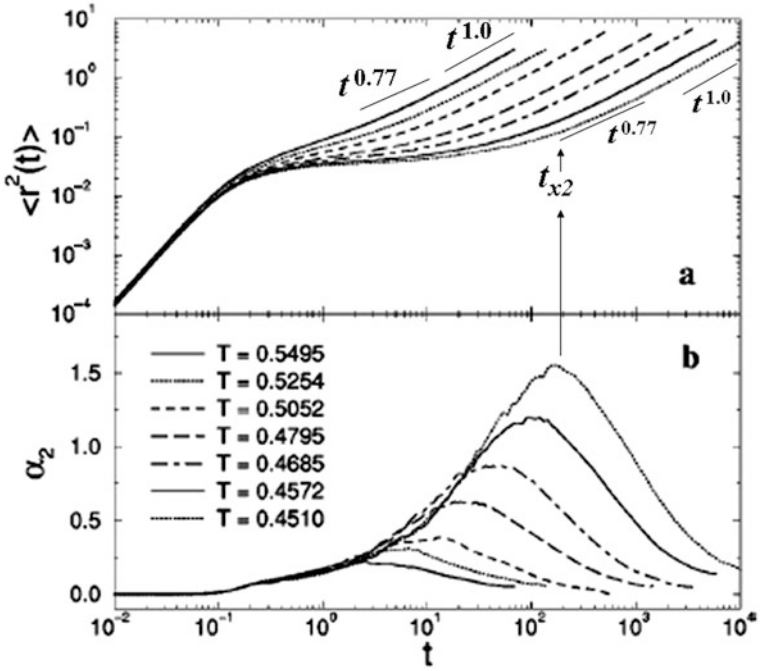

Fig. 275 (**a**) Mean-square displacement $< r^2(t) >$ of the A particles of binary L-J liquid vs. time for several values of T. (**b**) Non-Gaussian parameter $\alpha_2(t)$ vs. time for the same values of T as in (**a**). From Donati et al. [321], and reproduced by permission

the subdiffusion is denoted by t_{x2} and its location for $T = 0.451$ is indicated approximately by the arrow in Fig. 275. At lower temperatures, the particles are initially caged, and the caged dynamics contributes a power law $< r^2(t) > \propto t^{\gamma}$ to the MSD with $\gamma << 1$ or a nearly constant loss (NCL) with frequency dependence $\omega^{-\gamma}$ to the susceptibility $\chi''(\omega)$. In order of time, the caged dynamics term $< r^2(t) > \propto t^{\gamma}$ is followed by the subdiffusion term $< r^2(t) > \propto t^{1-n}$ and in turn by the terminal diffusion term $< r^2(t) >= 6Dt$. The value of the fractional power (1-n) of the subdiffusion is comparable to the stretch exponent β in the Kohlrausch function used to fit the intermediate scattering function $F_s(q, t)$ for $q = q_{\max}$ [321]. On decreasing temperature, the term $< r^2(t) > \propto t^{\gamma}$ persists to longer times, accompanied by decrease in both $< r^2(t) >$ and the exponent γ reflecting increasing degree of caging. At $T = 0.451$, γ is about 0.1. This description of dynamics from the simulations is along the line as in Chapter 2. It needs to be pointed out that the same results from simulations of the binary LJ mixtures were interpreted by others [265, 321] in terms of the idealized mode coupling theory (MCT). In fact these results were considered as verification of the predictions of the original version of MCT, although it cannot explain the dynamic lattice liquid simulation results and the dynamic light-scattering data of colloidal particle suspensions with $\phi = 0.465$.

For diffusion in d-dimension, $F_s(q,t)$ was sometimes approximated by

$$F_s(q,t) \approx \exp\left[-\frac{q^2}{2}\langle r^2(t)\rangle/2d + \frac{q^4}{2}\left(\frac{\langle r^2(t)\rangle}{2d}\right)^2 \alpha_2(t)\right], \tag{3.3}$$

where the non-Gaussian parameter $\alpha_2(t)$, given before by Eq. (1.125), is a measure of the deviation from the Gaussian dynamics, because it vanishes when the dynamics is Gaussian. Shown in Fig. 275(b) is $\alpha_2(t)$ obtained by Donati et al. from their simulations of binary L-J mixture. It exhibits a peak and the maximum of $\alpha_2(t)$ occurs close to t_{x2}, the onset time of subdiffusion, which is demonstrated for $T = 0.451$ by the vertical arrow in Fig. 275. We have seen before from several examples in Section 2.3.2.33 that t_{x2} is a few times longer than the primitive relaxation time τ_0. This, together with the location of t_{x2} for $T = 0.451$, suggests possibly that $\tau_0 \approx 100$ (L-J units). From the discussion in Section 2.2.1.1, t_c of the binary L-J particles is about 1. Donati et al. fitted $F_s(q_{max},t)$ to the Kohlrausch function having stretched exponent $(1-n) = 0.75$ and $\tau = 655$. The approximate values of these parameters are consistently related by the CM equation (2.14) $\tau = \left[(t_c)^{-n}\tau_0\right]^{1/(1-n)}$.

The MSD $< \Delta x^2(\Delta t) >$ and the non-Gaussian parameter $\alpha_2(\Delta t)$ of colloidal particle suspensions determined by confocal microscopy at various volume fractions ϕ [141] show the same behavior as the L-J system. These quantities for $\phi = 0.56$ have been shown before in Fig. 247 in connection with the nearly constant loss (i.e., the initial plateau in the MSD) from caged dynamics and the primitive relaxation time indicated by Δt when a typical particle changes position and leaves the cage, which is about 500 s for $\phi = 0.56$. The subdiffusion with $< \Delta x^2(\Delta t) > \propto (\Delta t)^{1-n}$ and its onset at t_{x2} are illustrated in the figure. Also shown is the initial plateau having $< \Delta x^2(\Delta t) > \propto (\Delta t)^{0.13}$, contributed by motions of particles trapped in anharmonic cages, which gives rise to the susceptibility $\chi''(\omega)$ having the frequency dependence of $\omega^{-0.13}$ (i.e., the NCL). For the sake of easy comparison of binary L-J mixtures and Li^+ ions in Li_2SiO_3 with the MSD at different temperatures to be discussed below, the $< \Delta x^2(\Delta t) >$ for $\phi = 0.46$ and 0.52 are shown together with $\phi = 0.56$ in Fig. 276. Returning to Fig. 247, the inset therein presents the time dependence of the non-Gaussian parameter $\alpha_2(\Delta t)$, which also peaks at t_{x2} as in the case of the binary L-J mixture.

Ion Dynamics in Glassy Ionic Conductor

All the examples given above are glass-forming systems, and the similarity of the MSD of some of them may not be surprising. Now we present the MSD of other interacting systems unrelated to glass transition, and the remarkable thing is that they are also similar. The similarity has repercussion on theoretical interpretation of the dynamics in some of the systems, which will become clear later.

Historically, Kohlrausch studied the electrical relaxation of a Leyden jar (an alkali silicate glassy ionic conductor) in 1854 at Göttingen [2, 3] in which he found that the time decay of ionic conductivity relaxation has the stretched exponential

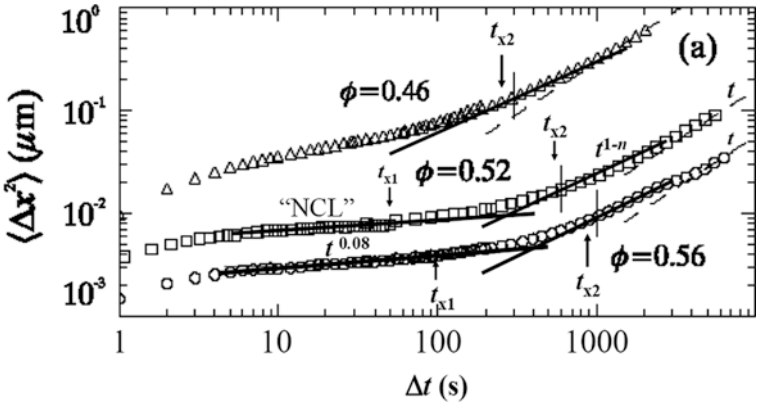

Fig. 276 Mean-square displacements of colloidal particles in suspension from Weeks and Weitz [800]. The *diagonal dashed straight lines* indicate estimates for $<\Delta x^2(\Delta t)>\sim 2Dt$. The *solid lines* indicate $<\Delta x^2(\Delta t)>\propto (\Delta t)^{1-n}$ starting at about t_{x2}. The NCL regime is depicted by the nearly flat line representing $<\Delta x^2(\Delta t)>\propto (\Delta t)^c$ with c small in the range from 0.08 to 0.13. This power law terminates at t_{x1}. *Vertical bars* indicate estimate of the cage rearrangement timescale Δt^* by finding the maximum of the non-Gaussian parameter. The proximity of Δt^* to t_{x2} is clear from the figure. The primitive or independent relaxation time τ_0 calculated by the CM equation is near t_{x2} [1058]

time dependence given by Eq. (1.1). If scientific activity in ionic conductivity relaxation and diffusive transport in glasses is considered to have started by Kohlrausch, then by now the research field is about 160 years old. Many research efforts in this area since then will not be mentioned here, except those having results on the ion dynamics that brings out the universal dynamic properties. The first example is the dynamics of mobile ions in glassy ionic conductors. Habasaki and coworkers have carried out molecular dynamics simulations of Li ion dynamics in the metasilicate glass Li_2SiO_3 since 1997, and many properties have been uncovered [468–472, 475, 802, 1058]. The $<r^2(t)>$ and $\alpha_2(t)$ of Li ion motions at different temperatures is shown in Fig. 277.

There is hardly any difference in their behaviors as functions of time and change with temperature as the binary L-J mixture and the colloidal particles (on changing volume fraction). In particular, prior to the free diffusion is the presence of the subdiffusion term $<r^2(t)>\propto t^{1-n}$ which is preceded by the caged dynamics term $<r^2(t)>\propto t^c$. The data at 700 K in the main figure show the subdiffusion $<r^2(t)>\propto t^{0.64}$ and its onset time at t_{x2} in between 20 and 30 ps. This is about the same time at which $\alpha_2(t)$ at 700 K peaks as indicated in the figure. The same is true for other temperatures. The exponent c of caged dynamics term $<r^2(t)>\propto t^c$ is 0.11 or 0.13, which is about the same as that of the binary L-J mixture (Fig. 275) and the colloidal particles with $\phi = 0.56$ (Fig. 247 and 276).

The self-part of the van Hove function, discussed in Chapter 1 and defined before in Eq. (1.112) by $G_s(\vec{r},t) = (1/N)\sum_{i=1}^{N}\langle\delta(\vec{r}_i(t)-\vec{r}_i(0)-\vec{r})\rangle$, of the Li ions obtained

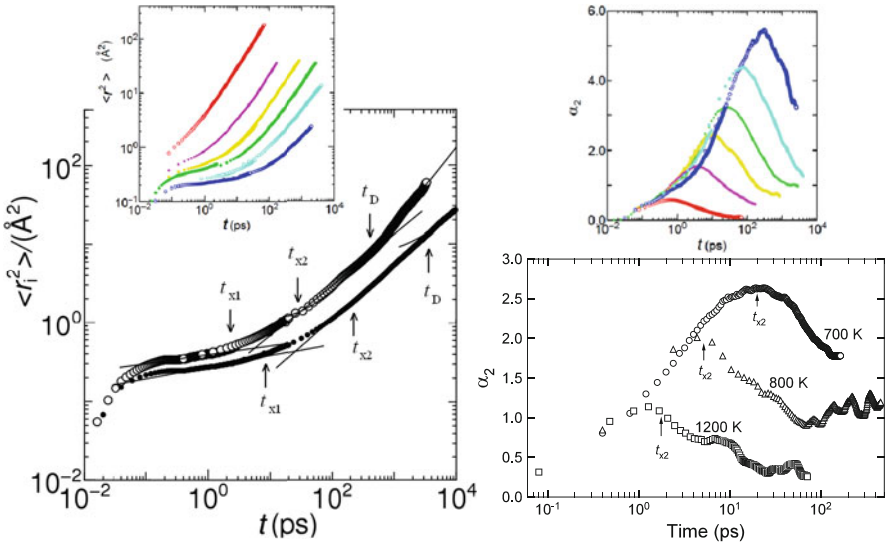

Fig. 277 (*Left*) MSD of Li^+ ions in Li_2SiO_3 at 600 K (*lower*) and 700 K (*upper*). The t_{x1}, t_{x2}, and t_D are crossover times that separate out the four time regimes explained in the text. $t_{x1} \approx 2$ ps at 700 K and $t_{x1} \approx 10$ ps at 600 K. The *inset* shows the MSD of Li ions at 1673, 1000, 800, 700, 600, and 500 K from top to bottom. (*Right*) The non-Gaussian parameter $a_2(t)$ for Li^+ ions in Li_2SiO_3 calculated from their time-dependent displacement distribution function at 700, 800, and 1200 K (*lower panel*) and at 1673, 1000, 800, 700, 600, and 500 K from *bottom* to *top* (*upper panel*). At higher temperatures, the maximum of $a_2(t)$ for the Li^+ ions moves to shorter times and at all temperatures the maximum is located near t_{x2}

by the molecular dynamic simulations [1487–1489] is shown for different times within four time regimes in Figs. 278(a)–(d). The times in the four time regimes are (1) 0.40, 0.8, and 1.6 ps ($t < t_{x1}$); (2) 3.2, 6.4, 12.8, and 25.6 ps ($t_{x1} < t \approx t_{x2}$); (3) 40, 80, 160, and 200 ps ($t_{x2} < t < \tau$); and (4) 400, 800, and 1600 ps ($t > \tau$). Here $\tau \approx 229$ ps is the stretched exponential relaxation time of the incoherent scattering function $F_s(k,\ t)$ for $k = 2\pi/3\,(\mathring{A}^{-1})$. Such k is chosen because it corresponds to $\sqrt{\langle r^2 \rangle} \approx 3\,\mathring{A}$, the distance between Li sites. This together with $(1-n) \equiv \beta = 0.64$, $t_c = 1$ ps, and the CM equation (3.1) enables us to calculate τ_0 and the result is 32 ps, which is an order of magnitude longer than t_{x1} but is nearly the same as $t_{x2} \approx 27$ ps. The onset of terminal diffusion with $< r^2(t) > \propto t^{1.0}$ starts at $t_D \approx 400$ ps, which is slightly longer than $\tau \approx 229$ ps.

$G_s(r, t)$ of Li^+ ions has similar dependences on space and time as the same function of the binary L-J mixture [321] and the analogous distribution function $P(\Delta x)$ of colloidal particles [141]. Furthermore, the Li ion dynamics is heterogeneous with the presence of faster and slower ions, like that found in the other two systems as well as in glass-forming liquids.

In regime (1), $t < t_{x1}$, in the framework of the CM, the fact that τ_0 is significantly longer than t_{x1} explains the small probability of independent jump of the ions out

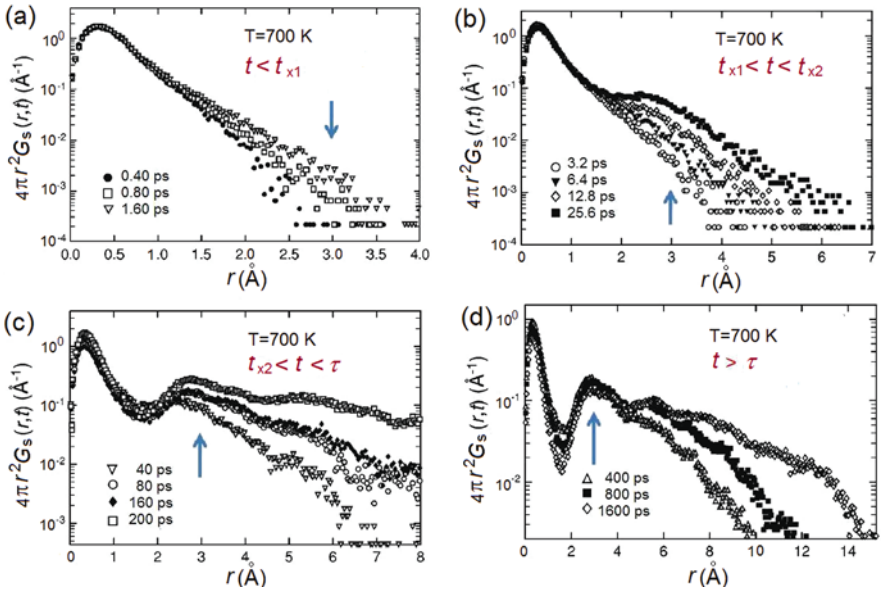

Fig. 278 $4\pi r^2 G_s(r,t)$ of Li^+ ions in Li_2SiO_3 at 700 K as a function of r at different times. $G_s(r,t)$ is the self-part of the van Hove function for the Li ion. (**a**) 0.40, 0.8, and 1.6 ps ($t < t_{x1}$). (**b**) 3.2, 6.4, 12.8, and 25.6 ps $t_{x1} < t \approx t_{x2}$. (**c**) 40, 80, 160, and 200 ps ($t_{x2} < t < \tau$); $\tau \approx 229$ ps is calculated (see text). (**d**) 400, 800, and 1600 ps. The *vertical arrows* indicate the distance of 3 Å, roughly the separation between neighboring Li^+ sites. Data from [468] are replotted together with additional illustrations in all figures

of their cages during the caged ion regime. It also explains the very slow decay of the cage indicated by either the plateau-like MSD or practically no decrease of the normalized area, $A_1(t)$, of the first peak of the self-part of the Li ion van Hove function, used to gauge the cage decay (see left panel of Fig. 279). $A_1(t)$, obtained by integrating $4\pi r^2 G_s(r,t)$ over the first peak domain of r <2 Å, can be considered as the analogue of the cage decay function of Weeks and Weitz for colloidal particles from confocal microscopy shown in Fig. 247. Alternatively, caged dynamics can be seen from $A_2(t)$ obtained by integrating $4\pi r^2 G_s(r,t)$ over the first neighboring shell region with r between $r_1 = 2$ and $r_2 = 4$ Å. $A_2(t)$ remains very small for $t < t_{x1}$, indicating negligible number of ions hopping over to the neighboring sites.

In the time regime (2), $t_{x1} < t < t_{x2}$, there is non-negligible probability for independent ion jumps to neighboring sites, particularly when time increases towards t_{x2} because t_{x2} is comparable to τ_0. This can be seen by the development of a shoulder and then a peak in $4\pi r^2 G_s(r,t)$ as t increases from 3.2 up to 25.6 ps. Therefore the cages start to decay in regime (2), a property corroborated by the departure of the MSD from the relation $< r^2(t) > \propto t^{0.11}$ in Fig. 277 (left). It is also corroborated by the initially small decrease and increase of the normalized area $A_1(t)$ and $A_2(t)$, respectively, in the regime $t_{x1} < t < t_{x2}$.

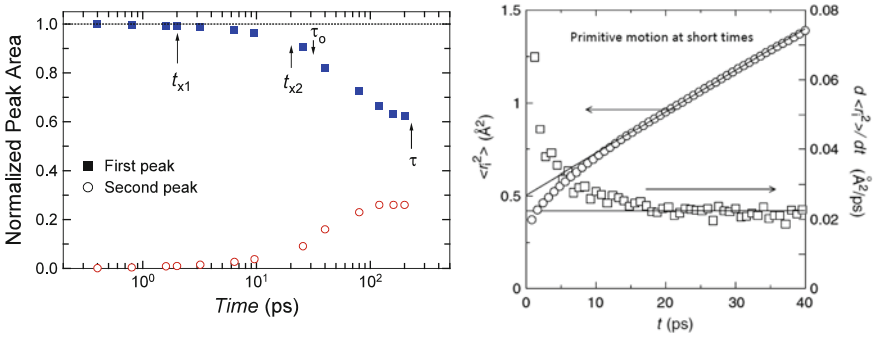

Fig. 279 (*Left*) Normalized areas of the first peak $A_1(t)$ and the second peak $A_2(t)$ of the self-part of the Li ion van Hove functions at 700 K at different times shown up to 200 ps. The positions of t_{x1}, t_{x2}, τ_o, and τ are indicated by the *vertical arrows*. Data from [468] replotted. (*Right*) Plot of $< r^2 >$ at 700 K against time, showing the linear relation within the approximate range of $15 < t < 40$ ps, which is the primitive relaxation regime. Plot of $d < r^2 > /dt$ at 700 K against time, showing that $d < r^2 > /dt$ is nearly constant within the range $15<t<40$ ps. Data from [802] replotted together with illustration in the figure

In the time regime (3), $t_{x2} < t < \tau$, t is longer than τ_0 for practically all times. Therefore, the Li ions are capable of executing the independent jump having the primitive relaxation time τ_0 with significant probability. But, instead of independent jumps with no correlation with each other, they participate in some cooperative or correlated hopping process. This is evidenced by the observed stretched exponential correlation function for the intermediate scattering function $F_s(k,t)$ in regime (3), instead of linear exponential decay for independent hops [1488]. This is like $F_s(k,t)$ found by dynamic light scattering in colloidal particle suspension by Segre and Pusey [143]. Thus t_{x2} marks the change from apparent free jump to the cooperative/correlated jump process. Again this description is corroborated by even more rapid decrease of A_1 in regime (3) than in regime (2), as can be seen by the steeper rise of the MSD with the power law dependence of $< r^2(t) > \propto t^{1-n}$, with $(1-n) \equiv \beta \approx 0.64$ in Fig. 277 (left), and population in the second peak of $4\pi r^2 G_s(r,t)$ given by A_2. This is exactly like the colloidal supercooled liquid with $\phi = 0.56$ from the data of confocal microscopy shown in Figs. 247 and 276 in the corresponding time regime $t_{x1} < t < t_{x2}$, and likewise the cage correlation function of Weeks and Weitz (see inset in Fig. 247) show much faster decay when $t>t_{x2}$ than in regime 2.

In the right panel of Fig. 279 is the linear plot of $< r^2(t) >$ against linear time in the abridged time region, $15 < t < 40$ ps, within which lies the calculated primitive relaxation time τ_0. The plot shows the linear relation $< r^2(t) > \propto t^{1.0}$ within the approximate range of $15 < t < 40$ ps, supported by $d < r^2 > /dt$ being nearly constant within the range $15 < t < 40$ ps. This is evidence for the existence of the primitive relaxation because it gives rise to independent ion jumps, and their contribution to the MSD should be linearly proportional to time. Existence of the primitive relaxation is additionally supported by the time development of A_2, the area of the second peak of $4\pi r^2 G_s(r,t)$. In the 15–40 ps region, $A_2(t)$ increases

linearly with time [802], where the area is proportional to net increase in the number of ions in the first neighboring shell region. The primitive relaxation regime also exists at 600 K within the range of $150 < t < 250$ ps as shown by the linear time dependence of $< r^2 >$ in Fig. 5 in [802] and the nearly constant $\mathrm{d} < r^2 > /\mathrm{d}t$.

In the time regime (4), $t > \tau$, Li ion sites at further distances are populated as can be seen from $4\pi r^2 G_s(r,t)$ in Fig. 278. Terminal diffusion with $< r^2(t) > \propto t^{1.0}$ is reached. At the onset time of this regime (about 600 ps at 700 K and 2000 ps at 600 K), the square root of the MSD $\sqrt{\langle r^2 \rangle}$ is about 3 Å, which is the average Li-Li ion site separation distance.

3.2.1.2 Space-Time Pictures of Motions of Li^+ Ions Equivalent to Those of Motions of Colloidal Particles by Confocal Microscopy

Habasaki and I [802] have generated space-time pictures to elucidate the motion of Li ions in Li_2SiO_3 at 700 K at different times, which is equivalent to the real-time pictures of motion of colloidal particles provided by confocal microscopy [141, 800]. These pictures of Li ions at progressively longer times of 4, 8, 16, 24, 48, 200, 400, and 1000 ps give clear information of the motions of Li ions in the different dynamic regimes.

Before presenting these space-time pictures, let us remind the reader that from the time dependences of $< r^2(t) >$ and $G_s(r,t)$, several dynamic regimes of Li^+ ions at 700 K have been delineated by the three times, t_{x1}, t_{x2}, and t_D shown in Fig. 277. The space-time pictures of the motion of Li^+ ions are discussed in the regimes defined by these three times.

Figure 280(a)-(d) shows the displacements of the Li ions at four chosen times 4, 8, 16, and 24 ps, respectively, at 700 K. The displacements of the Li ions are indicated by the vectors originating from the positions of the ions at an arbitrary chosen initial time t_0 in three dimensions for a part of the basic cell of the simulation. The amplitudes of the vectors are coded according to the color scheme shown. These results are supposed to represent the behavior of the ions within the time regime (2) bounded approximately by $t_{x1} \sim 2\,\mathrm{ps} < t < t_{x2} \sim 30\,\mathrm{s}$. According to the color code of these figures, there are few isolated jumps to nearest neighboring Li sites with distance of about 3 Å, and the number of such jumps increases with time. These isolated jumps are the primitive relaxation of the CM that we are looking for and have been identified before in the right panel of Fig. 279 by their contribution to the MSD that is linearly proportional to time within the approximate range $15 < t < 40$ ps, within which lies $\tau_0 \approx 32$ ps.

The primitive relaxation observed in MSD with $< r^2(t) > \propto t^{1.0}$ in the range of $15 < t < 40$ ps ends at longer times past τ_0 or t_{x2} when more ions jump to neighboring sites and these jumps are no longer isolated events. This can be seen starting at 48 ps in the panel (a) of Fig. 280 (lower four). With further increase in time, more ions have displacements equal to or larger than the distance between neighboring Li sites. The ions undergoing these large amplitude motions form clusters and the vectors of their motions tend to be linked together, and the length scale of the vectors linked together increases with time. Conversely the ions limited to local motions

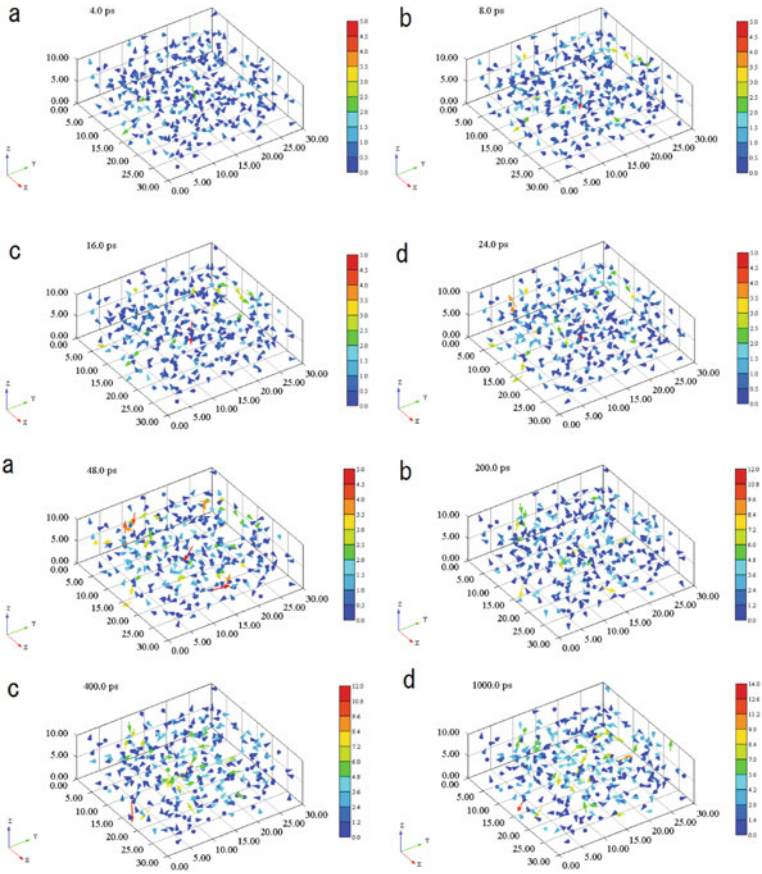

Fig. 280 (*Upper four*) Motion of Li ions in Li_2SiO_3 at 700 K at four different times: (**a**) 4 ps, (**b**) 8 ps, (**c**) 16 ps, and (**d**) 24 ps. The positions of the Li ions at any of the indicated chosen times are represented by the vectors originating from the positions of the ions at an initial time in three dimensions for a part of the basic cell of the simulation. The values of axes are in Å. The *colors* are used to indicate the lengths of the vectors (the values shown in the legend are also in Å). Note that the color codes of the scales for 4, 8, 16, and 24 ps are the same. The rare maximum displacements of the Li ions are 2.5, 3.5, 3.5, and 4.0 Å for 4, 8, 16, and 24 ps, respectively. But note that most of the displacements have magnitudes smaller than the maximum value. (*Lower four*) Motion of Li ions in Li_2SiO_3 at 700 K at four times: (**a**) 48 ps, (**b**) 200 ps, (**c**) 400 ps, and (**d**) 1000 ps. The positions of the Li ions at any of the indicated chosen times are represented by the vectors originating from the positions of the ions at an initial time in three dimensions for a part of the basic cell of the simulation. The values of axes are in Å. The *colors* are used to indicate the lengths of the vectors (the values shown in the legend are also in Å). Note that the code of the color scales for 48 ps is different from that of 200 and 400 ps, and from that of 1000 ps. The maximum displacements of the Li ions are 4.5, 7.8, 9.0, and 11.8 Å for 48, 200, 400, and 1000 ps, respectively. But note that most of the displacements have magnitudes smaller than the maximum value. Reproduced from [802] with permission

also form clusters. The increase of the length scale of the mobile ion clusters with time can be seen in going in succession from panels (a), (b), (c), and (d) at 48, 200, 400, and 1000 ps respectively. These features of Li^+ ions motion are exactly the same as those found in colloidal particle suspensions by confocal microscopy [141].

Shown previously in Fig. 23 are the motions of the colloidal particles in suspension with volume fraction $\phi = 0.52$ at the cage rearranging time $\Delta t^* = 600$ s, estimated by finding the maximum of the non-Gaussian parameter $\alpha_2(\Delta t)$. The location of Δt^* is indicated by the vertical bar crossing the MSD data for $\phi = 0.52$ in Fig. 276, and it can be seen from this figure that $\Delta t^* \approx t_{x2}$. Therefore, since $t_{x2} \approx 30$ ps from the Li metasilicate glass, the pattern of motion of Li^+ ions at 24 or 48 ps shown in Fig. 280 (upper d) and (lower a), respectively, is to be compared with that of colloidal particles with volume fraction $\phi = 0.52$ at $\Delta t^* = 600$ s. The patterns in both systems have similar character. The motions of the Li^+ ions are obviously dynamically heterogeneous. There are fast and slow ions classified as such by both temporal (waiting time of jumps) and spatial (back-and/or-forth correlation) behaviors [1488, 1489]. Back-correlated jumps return to the original positions.

(4) At even longer times, the two types of ions, fast and slow, exchange roles. This feature is also found in glass-forming liquids [226–228], referred to as heterogeneous dynamics and discussed before in Chapter 1. When these motions are coarse grained, the MSD assumes the linear dependence t, and steady-state diffusion regime is reached. The onset time of this regime t_D is about 600 ps at 700 K and about 2000 ps at 600 K. As can be seen from the left panel of Fig. 277, at t_D the root MSD $\sqrt{\langle r^2 \rangle}$ is about 3 Å, which is the average Li-Li ion site separation distance, although even in a diffusive regime, dynamics is still heterogeneous.

The primitive relaxation time increases when temperature is lowered from 700 to 600 K, and this change explains the lengthening of the time/frequency range of the NCL, as observed by experiment. The primitive relaxation also marks the onset of many-molecule dynamics. As time increases, increasing number of ions participate in cooperative motion until the maximum number, dictated by the ion-ion interaction and the matrix, is reached and steady-state diffusion begins.

In total, the processes found in the mean-square displacement of Li^+ ions in Li metasilicate include the caged dynamics, the primitive relaxation, the heterogeneous jump dynamics, and steady-state diffusion. The primitive relaxation terminates the caged ion dynamics, and it also marks the onset of many-molecule dynamics. These processes are isomorphic to those found in molecular glass-forming liquids and colloidal particles. Previously in ionic conductors the isomorphism was incomplete because of the absence of direct experimental evidence for the primitive relaxation, whereas in molecular glassformers, the evidence is provided by the universal Johari-Goldstein relaxation. By finding the primitive relaxation by molecular dynamics simulation presented in this study, we show that the underlying physics of the dynamics of ionic systems is exactly parallel to that of molecular glass-forming liquids, in spite of the fact that the Li^+ ions are moving in the metasilicate glassy matrix and have nothing in common with supercooled liquids.

From the above discussion, it is clear that time dependences of the MSD, the non-Gaussian parameter, and the heterogeneous dynamics of Li ions in Li_2SiO_3 are isomorphic to those of the binary L-J mixture and the colloidal particle suspension. The isomorphism indicates that the dynamics of diffusion in interacting systems has universal properties and suggests a common explanation for all. In the next subsection to follow, conductivity relaxation data of various crystalline and glassy ionic conductors [195, 1057, 1058] are introduced to support this isomorphism. Details of the experimental data are presented later in Sections 3.2.6.3, 3.2.6.4, and 3.2.7. The implication of universal properties found entirely in different classes of interacting systems poses problem for theory/model that is applicable to explain one system but not the others. Such is the case of MCT designed specifically for glass-forming liquids. It is a fluid- and density-based theory and does not seem natural to apply to dynamics of glassy ionic conductors such as lithium metasilicate glass where the Li ions are diffusing into the glassy matrix [1057, 1058]. Crystalline ionic conductors such as Na β-alumina [1486], $Li_{0.18}La_{0.61}TiO_3$ (LLTO) [1482, 1484, 1491], yttria-stabilized zirconia (YSZ), $(Y_2O_3)_x(ZrO_2)_{1-x}$ [149, 1492], and the pyrochlores $Gd_2Ti_{2-y}Zr_yO_7$ with $0.5 \leq y \leq 2$ [150–153, 1493] show exactly the same ion dynamics as glassy ones, and there the applicability of MCT is hard to believe to be possible. The main support of the idealized MCT to glass-forming liquids comes principally from good fits by its prediction to the frequency dependence of the observed susceptibility spectrum $\chi''(\nu)$ and the predicted various power law dependences on $(T - T_c)$ of the susceptibility minimum value $\chi''_{\min}$ and frequency $\nu_{\min}$ as well as the relaxation time of the α-relaxation. Success of these fits seems not sufficient to prove applicability of MCT to glassformers because equally successful good fits were obtained for the dielectric loss $\varepsilon''(\nu)$ of silver ions in silver iodide-silver selenate glassy ionic conductor [1494] to which MCT does not apply.

3.2.1.3 Support from Conductivity Relaxation Data of Crystalline, Glassy, and Molten Ionic Conductors

There is a relation between MSD and the complex conductivity [65]:

$$\sigma^*(\omega) = \omega^2 \frac{N_{\text{ion}} q^2}{6 H_R k T} \int_0^\infty < r^2(t) > e^{-i\omega t} dt, \tag{3.4}$$

where N_{ion} is the number density of mobile ions, q the ion charge, k the Boltzmann constant, and T the temperature. H_R, the Haven ratio, is the ratio of the self (tracer)-diffusion coefficient D^* and the conductivity diffusion coefficient D_σ. For ionic conductors with one kind of ions, D_σ is calculated from the measured dc conductivity σ_{dc} via the Nernst-Einstein equation [1490]. D^* is larger than D_σ and $H_{\text{R}} \leq 1$ because of the many-ion diffusion process necessitated by ion-ion interaction. In the absence of interaction, $H_{\text{R}} = 1$.

For $t < t_{x1}$, it follows from Eq. (3.4) that the MSD of caged dynamics $< r^2(t) > \propto t^c$ with $c << 1$ correspond to $\sigma'(\omega) \propto \omega^{1-c}$ for the real part of the ac conductivity $\sigma'(\omega)$ and $\varepsilon''(\omega) \propto \omega^{-c}$ for the dielectric loss at frequencies $\omega > (1/t_{x1})$.

For $t_{x2} < t < \tau$, the subdiffusion term $\langle r^2(t) \rangle \propto t^{1-n}$ gives rise to the power law frequency dependences $\sigma'(\omega) \propto \omega^n$ for the real part of the ac conductivity and $\varepsilon''(\omega) \propto \omega^{-(1-n)}$ for the dielectric loss in the frequency range $(1/\tau) < \omega < (t_{x2})^{-1}$.

For $t > \tau$, after these motions of fast and slow ions have been coarse grained, the MSD assumes the $t^{1.0}$ dependence of steady-state diffusion regime and $\sigma'(\omega)$ becomes a constant, which is the dc conductivity $\sigma_{\rm dc}$ and $\varepsilon''(\omega) \propto \omega^{-1}$.

From the parameters n and τ, the primitive relaxation time τ_0 can be calculated by the CM equation (3.1). Once τ_0 has been calculated, the relation $t_{x2} \approx \tau_0$ can be checked by the experimental data. Good agreement was obtained for many ionic conductors [1057, 1058], some of which are presented in Sections 3.2.6.3, 3.2.6.4, and 3.2.7.

Polymer Chain Dynamics

More than 10 years ago, MSD of the center of mass of polymer chains in both unentangled and entangled polymer liquids was found to display a subdiffusive diffusion behavior at shorter times, which crosses over to terminal free diffusive dynamics at a characteristic decorrelation time $\tau_{\rm dec}$ [1462, 1495–1502]. This subdiffusive behavior is characterized by an exponent that depends on the degree of polymerization N as well as temperature T and density of the sample. It is considered anomalous because the conventional theories of polymer dynamics, such as the Rouse model for unentangled polymer dynamics and the reptation model for entangled dynamics, predict no such subdiffusive center-of-mass motion at short times, in disagreement with simulations and experiments. The disagreement is not unexpected in our view because both models are mean-field theories of single-chain dynamics and many-body effects on diffusion leading to cooperative motion and dynamic heterogeneity in the liquid are neglected. The previous observations of subdiffusive dynamics have been mainly by simulations and some in a small range of times. Recently new data of neutron spin echo (NSE) performed by Zamponi et al. [1503] have extended the experimental time range up to about 200 ns to fully observe the subdiffusive behavior at shorter times and its crossover to the long-time normal diffusive regime. The four polyethylene samples investigated have molecular weights between 0.5 and 5.5 kg/mol covering the range from the low degree of polymerization regime of unentangled polymers to the entangled regime. All samples exhibit anomalous subdiffusive dynamics at short time and the transition to normal (Brownian-like) diffusion at long times. The deviation of the observed subdiffusion from normal diffusion increases with molecular weights.

The experimental work by Zamponi et al. is accompanied by the predictions of the theoretical approach of Guenza and coworkers [1504, 1505]. In this approach, specific intermolecular interactions are considered in the construction of a generalized Langevin equation for cooperative dynamics of a group of polymer chains. An analytical expression for the potential acting between the centers of mass of

a pair of polymer chains was derived which allows for a formal solution of the set of coupled equations of motion through normal-mode transformation. The theory predicts anomalous subdiffusive dynamics of the center-of-mass motion and crossover to normal diffusion after some long time. The subdiffusive dynamics is heterogeneous and the distribution is not Gaussian. All the aforementioned properties of the dynamics of polymer chains obtained by the theory of Guenza are analogous to the dynamics of Li^+ ions in Li metasilicate glass, binary LJ liquids, and colloidal particle suspension, discussed in Section "Ion Dynamics in Glassy Ionic Conductor."

Essentially, the theory of Guenza relates this anomalous behavior of chain diffusion to intermolecular correlation and the cooperative motion of a group of polymer chains in a dynamically heterogeneous liquid. Thus, the theory takes care of the many-chain diffusion in interacting chains systems in the same spirit as the coupling model for many-body relaxation for interacting systems. It is opposite in spirit to the single-chain, mean-field models of Rouse and reptation. Applications of the CM to polymer diffusion and viscoelasticity will be given later in this chapter.

Figure 281 presents the center-of-mass MSD data from neutron spin echo experiments (symbols) and the theoretical predictions from Guenza's theory (shorter dashed lines) for three samples with number of segments of the protonated diffusion PE chains $N = 106$, 192, and 377. Long dashed lines with slope exactly equal to 1 represent normal Brownian-like diffusion. Experimental data show the presence of subdiffusion with t^{1-n} dependence of the MSD over a period of time as indicated by the solid lines. The characteristic exponent $(1-n)$ decreases with increasing degree

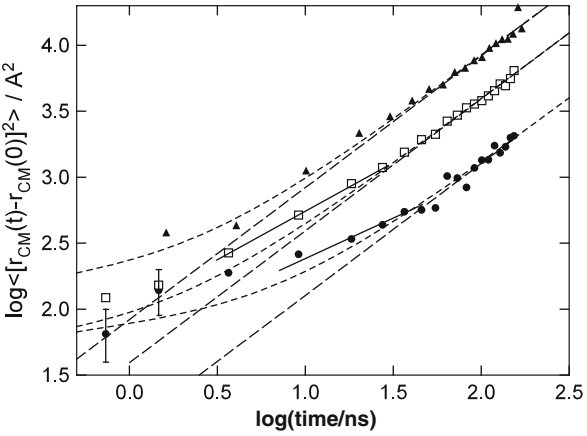

Fig. 281 The center-of-mass mean-square displacement extracted from the data at $q = 0.3$ nm^{-1}. *Symbols*: experimental data for $N = 106$ (*up triangles*), 192 (*open squares*), and 377 (*filled circles*). In the log−log plot, the *long dashed lines* have slope equal to 1, indicating terminal free diffusion at long times. *Short dashed lines* are calculated result from cooperative dynamics-generalized Langevin equation. *Solid lines* have slope equal to $(1-n)$ and are drawn to indicate the presence of subdiffusion. Data at shorter times have large uncertainties (errors not shown) and are not considered for the present purpose of showing the existence of the subdiffusion. Redrawn from the data of Zamponi et al. [1503]

of polymerization. Even in the unentangled polymers with $N = 36$ and 106, the subdiffusion appears, and thus the Rouse model of a single chain is not fully accurate when applied to undiluted polymers, although the deviation is not large because the fractional exponent $(1-n)$ is close to 1. Intermolecular interaction is enhanced by entanglements in polymer with larger N, and this is reflected by the decrease in $(1-n)$. For $N = 198$ and 377, the solid lines have slope or $(1-n)$ equal to 0.72 and 0.63, respectively. The MSD seems to level off with decreasing time past the subdiffusive regime. This behavior is reminiscent of the plateau in the MSD of caged Li ions, L−J, and colloidal particles shown in Figs. 275−277.

The presence of the subdiffusion in polymer chain diffusion with similar properties as those found in the dynamics of diffusion of Li ions, L−J, and colloidal particles further substantiates the universal behavior of diffusion in many-body interacting systems. These systems have widely different interaction potentials and yet the dynamics is similar. Specific to polymer dynamics, it also serves to show the inadequacy of conventional approaches to polymer melt dynamics such as the Rouse and the reptation models.

3.2.2 Stronger Interaction/Constraints Lead to Larger n

In Section 2.2.1 on glassformers, molecular structure with enhanced intermolecular interaction/constraint has increased stretching (or n) in the Kohlrausch correlation function of the structural relaxation. Analogues of this property abound in other interacting systems. Some examples are given below.

3.2.2.1 Ionically Conducting Systems

The concentration of mobile ions in many glassy ionic conductors can be changed by orders of magnitude. Naturally the interaction or the correlation between the motion of the ions is weak at very low concentration when the ions are far apart and increases with increasing concentration. Naturally interionic interaction vanishes and n is practically zero at very low ion concentrations and increases monotonically with concentration, provided there is no change in the structure of the glassy matrix. This expectation is realized experimentally in the broadening of the electric loss modulus peak $M''(\omega)$ as a function of the angular frequency ω with increasing ion concentration and the increase in n of the Kohlrausch function fit according to Eq. (1.56) [115(b), 148, 1057]. At very low ion concentration, $M''(\omega)$ narrows to become nearly the Fourier transform of a linear exponential function of time. The classic example is mobile Na^+ ions in a Vycor glass $x\text{NaO} - (1-x)[0.04\text{B}_2\text{O}_3 - 0.96\text{SiO}_2]$ at 313°C with $x = 0.00044$ and containing very few Na^+ ions by Simmons and coworkers [1506]. The family of Ag ion conductors $(\text{AgI})_x(\text{AgPO}_3)_{1-x}$ for $0 \le x \le 0.6$ shows monotonic narrowing of $M''(\omega)$ with decreasing x and the number of mobile Ag ions [1507]. In fact, fits to $M''(\omega)$ by the Fourier transform of the derivative of the Kohlrausch function for $\Phi(t)$ in Eq. (1.56) show decrease of n with the decrease in x [1508]. Here the reader is warned that there are publications by other workers where they concluded that the

same data when plotted as $\log_{10}\sigma(\omega)$vs. $\log_{10}\omega$ can be reduced to a universal curve when subjected to some scaling procedure. Here $\sigma(\omega)$ or $\sigma'(\omega)$ is the real part of the complex conductivity. From these results, these workers further conclude that the dynamics of migrating ions is the same independent of chemical structure and ionic concentration [1509−1511], in contradiction to what is indicated by the *same* data plotted as the electric loss modulus $M''(\omega)$. The width of the $M''(\omega)$ loss peak varies over a wide range when many ionic conductors are considered [115(b), 149]. In order to maintain their assertion that $\sigma(\omega)$ is universal for all ionic conductors, the proponents claimed that the electric loss modulus $M''(\omega)$ is not an appropriate representation of the data, although the complex $M^*(\omega)$ is no more than the reciprocal of the complex $\varepsilon^*(\omega)$, and $\sigma(\omega)$ is the real part of $i\omega\varepsilon_0\varepsilon^*(\omega)$. The attack on the electric modulus representation of data was shown to be invalid and refuted in [707]. The reasons why scaling of $\log_{10}\omega$ to an "universal" curve is fallacious were given in [115(b)]. They include (1) the differences in $\sigma(\omega)$ of different ionic conductors that are obscured in a log−log plot together with horizontal shift of data and (2) the presence of the near constant loss (NCL) contribution with $\sigma(\omega) = A\omega^{\mu}$ with $\mu \sim 1$ at higher frequencies irrespective of ion concentration and chemical structure. Demonstration of the absence of universal scaled $\log_{10}\sigma(\omega)$ vs. $\log_{10}\omega$ was given by comparing data from $Na_2O - 3SiO_2$ glass at −0.5°C with a high concentration of mobile Na^+ ions with those of the Vycor glass at 313°C with $x = 0.00044$ and containing very few Na^+ ions. The same conclusion was made in the comparison of $\log_{10}\sigma(\omega)$ data for two $xK_2O - (1 - x)GeO_2$ glasses with $x = 0.20$ and 0.0023 by Jain [1512]. The claim, that the dynamics of migrating ions is the same independent of chemical structure and ionic concentration, not only is bold but also was proffered without any theoretical support. As time tells, it serves no useful purpose, and only confusion of the real issue.

3.2.2.2 Entangled Polymer Chains

The simplest example is the comparison of an entangled monodisperse linear chain polymer with an entangled monodisperse multiple-arm, star-branched molecule with the same number of repeat units in each arm. Here, the change is in the architecture of the polymer and not in the chemical structure of the repeat unit. Obviously the multiple-arm stars have larger constraints on the movement of an individual macromolecule compared to the linear polymer. The CM predicts that n of the stars (or other architectures like H-polymers) is larger than that of the linear molecules. Experimentally this prediction is exemplified by a broader dispersion of the stars than the linear chains (see, for example, [1513]). As we shall see later, there are other predictions that accompany the predicted change of n, which have been verified by experiments.

3.2.2.3 Semidilute Polymer Solutions and Associating Polymer Solutions

More detailed description of these systems is given in a section to follow. The polymer chains in these solutions are still interacting via either entanglement or association. Naturally, increase of concentration of the polymer chains enhances

interchain coupling and constraints, and the expected increase of n in the Kohlrausch correlation function together with the consequences it has on other properties including concentration dependence and scattering angle dependence was found by experiments [198, 767, 778–780, 1514]. These aspects are subjects of further discussion to be given later. Here we cite the dielectric loss data of chain normal modes of poly(2,6-dichloro-1,4-phenylene oxide) (PDCPO) solutions from [1514]. With increasing concentration ϕ of the polymer such that the product ϕM approaches M_e, the molecular weight between entanglements, not only does the observed loss maximum frequency shifts to the low frequencies but also the loss curve simultaneously broadens on both sides of the peak maximum. The analysis of the spectra using the CM [925] relates the broadening to increase in coupling parameter n between chains with increasing concentration of PDCPO.

3.2.2.4 Junction Dynamics of Cross-Linked Polymers

A specific chemical moiety can link up a fixed number of polymer chains at a junction point. Multiple junction points convert the polymer chain to a network. The dynamics of the junctions has been studied experimentally [1515–1517]. The constraint on the motion of the junctions and hence $n \equiv (1 - \beta)$ is expected to decrease by lowering the density of junctions or the addition of a diluent. These expected changes by the CM were indeed observed by NMR measurements of the junction dynamics by Shi et al. [1515]. There are consequences of the dependence of n on junction density in the dynamic properties, and these are given in a later section.

3.2.3 Crossover from $\exp(-t/\tau_0)$ *to* $\exp[-(t/\tau)^{1-n}]$ *at* t_c

Like glassformers, there are experimental evidences in other interacting systems supporting the crossover of the correlation function from $\exp(-t/\tau_0)$ to $\exp[-(t/\tau)^{1-n}]$ in a neighborhood of a temperature-insensitive time t_c. We have mentioned before in Section 2.2.1.1 for polymers and small molecular van der Waals liquids that $t_c \approx 2$ ps. As we see below, the magnitude of t_c differs from one class of systems to another, increasing with decreasing strength of interaction and/or constraints. This trend is understandable, because in the limit of zero strength of interaction or no constraints, many-body relaxation is reduced to one-body relaxation, and its correlation function $\exp(-t/\tau_0)$ should hold for all times and hence $t_c \to \infty$.

3.2.3.1 Ionically Conducting Systems

Fast Glassy Ionic Conductors

There are many fast glassy ionic conductors where the mobility of the ions is so high that the conductivity relaxation time τ_σ is 10 orders of magnitude or more lesser than the structural relaxation time τ_α at T_g. In contrast, in $0.4Ca(NO_3)_2 - 0.6KNO_3$

(CKN) discussed in Section 2.2.1.1, τ_σ is only about 2−3 orders of magnitude lesser than τ_α at T_g [55, 1418]. These fast glassy ionic conductors can have τ_σ becoming very short by raising temperature but still staying within the glassy state. This is an example of relaxation of an interacting system which does not involve glass transition because T here is always significantly below T_g. At lower temperatures where $\tau_\sigma >> t_c$ of the order of 1 ps, the conductivity relaxation correlation of glassy and crystalline ionic conductors is well described by the Kohlrausch function $\exp[-(t/\tau_\sigma)^{1-n}]$, as shown by fits of the data in the electric modulus $M^*(\omega)$ representation by the Fourier transform of the derivative of the Kohlrausch function (see Section 1.2.2 and [55, 362, 707, 1518, 1519]). The conductivity $\sigma(\omega)$ corresponding to the $M^*(\omega)$ obtained with $\exp[-(t/\tau_\sigma)^{1-n}]$ has the ω^n dependence at high frequencies when $\omega\tau_\sigma >> 1$ and approaches the dc conductivity σ_{dc} in the low-frequency limit when $\omega\tau_\sigma << 1$ [1057, 1058]. The crossover of the correlation function from $\exp[-(t/\tau_\sigma)^{1-n}]$ to $\exp(t/\tau_0)$ with decreasing time past t_c is observed via the corresponding $\sigma(\omega)$ crossing over from the ω^n dependence to a frequency-independent value with increasing frequency past $\omega_c \equiv (t_c)^{-1}$. Here, two examples of the crossover are chosen from the work of Cramer et al. on two fast glassy ionic conductors $0.44LiBr-0.56Li_2O-B_2O_3$ [1520], and $0.5Ag_2S-0.5GeS_2$ glass [1521]. In inorganic glasses, the vibrational contribution to $\sigma(\omega)$ extends from high frequencies down to low frequencies with an ω^2 dependence [336], which is also found in these glassy ionic conductors as shown in Figs. 282 and 283. The Li

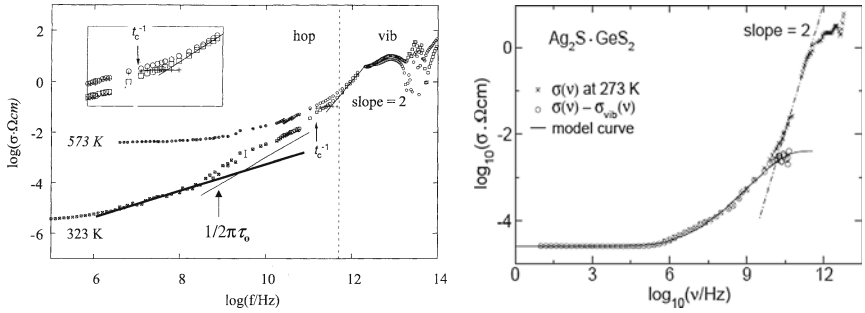

Fig. 282 (*Left*) The ac conductivity data of $0.44LiBr-0.56Li_2O-B_2O_3$ reconstructed from the data of Cramer et al. [1520]. Shown also is the high-frequency vibrational contribution to $\sigma(\omega)$ extending down to low frequencies with an ω^2 dependence. Subtracting off this vibrational contribution from the data at 573 K leaves a frequency-independent σ_0 (+). The inset shows this more clearly as well as the crossover of $\sigma(\omega)$ at a frequency of about 10^{11} Hz from frequency-independent σ_0 to the ω^n dependence. At lower temperatures such as 323 K, there is a contribution with near-$\omega^{1.0}$ dependence to $\sigma(\omega)$, the counterpart of the near constant loss in $\varepsilon''(\omega)$ at high frequencies, which obscures the crossover of diffusing ions at 10^{11} Hz. The nearly constant loss is due to loss while the mobile ions are still caged. (*Right*) Frequency-dependent conductivity $\sigma(\nu)$ of $0.5Ag_2S \cdot 0.5GeS_2$ glass at 273 K. Below 10 GHz, $\sigma(\nu)$is essentially caused by the hopping motion of the silver ions, while above 20 GHz it is essentially due to the low-frequency flank of the vibrational component. The ion contribution $\sigma_{ion}(\nu) = [\sigma(\nu) - \sigma_{vib}(\nu)]$ exhibits a crossover to primitive ionic conductivity relaxation at $10^{10.5}$ Hz. Figure reproduced from [1521] by permission

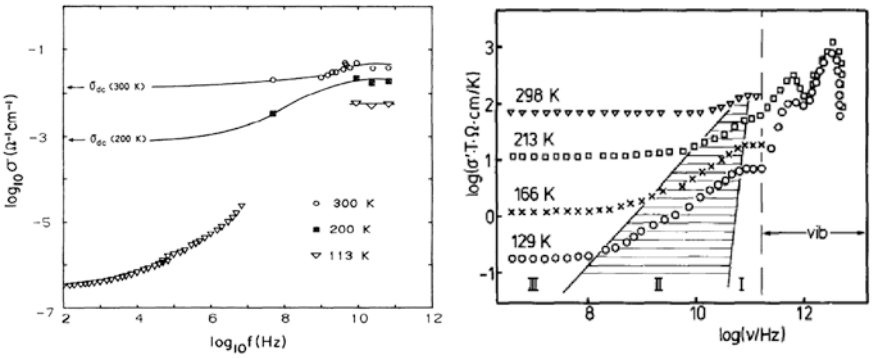

Fig. 283 (*Left*) Frequency dependence of $\sigma(\nu)$ of Na β-alumina at three temperatures showing crossover after 10^{10} Hz. Reproduced from [1522(a)] by permission. (*Right*) The product $\sigma(\nu)T$ of $RbAg_4I_5$ crystals at four different temperatures. The crossover is seen for 166 and 129 K. Reproduced from [1525, 1526] by permission

ion conductivity contribution is obtained after the tail of the vibrational contribution with an ω^2 -dependence has been subtracted off.

The results are shown for $0.44LiBr{-}0.56Li_2O{-}B_2O_3$ in the left panel of Fig. 282 at the high temperature of 573 K where ionic diffusion is the dominant contribution to $\sigma(\omega)$; there is a crossover of $\sigma(\omega)$ at a frequency $\omega_c \equiv 1/t_c$ of the order of 10^{11} Hz from an ω^n dependence to a frequency-independent value σ_0, just like that found for structural relaxation of the glassformer $0.4Ca(NO_3)_2{-}0.6KNO_3$ (CKN) at temperatures far above T_g (see Fig. 8 and recall that structural relaxation and conductivity relaxation in CKN are coupled together at high temperatures [55, 1418]). According to the CM, σ_0 is determined by the primitive relaxation time τ_0, while the dc conductivity σ_{dc} is governed by τ_σ, and the two relaxation times τ_σ and τ_0 are related by the CM equation (3.1) with τ_σ replacing τ. In the glassy state, both σ_{dc} (or τ_σ) and σ_0 (or τ_0) have Arrhenius temperature dependence with activation energies E_{dc} and E_0, respectively. In the case of $0.44LiBr{-}0.56Li_2O{-}B_2O_3$, the data of Cramer et al. [1520] yield $E_{dc} = 0.49\,eV$ or 5670 K, and $E_0 = 0.22\,eV$ or 2553 K. The exponent $(1{-}n)$ of the Kohlrausch function is estimated to be within the range of $0.40 < (1-n) < 0.48$. The other CM equation (3.2) predicts that

$$E_0 = (1-n)E_{dc}. \tag{3.5}$$

The product on the right side of this equation lies within the bounds $2268 < (1-n)E_{dc} < 2721$ K, and is consistent with $E_0 = 2553$ K [148].

The right panel of Fig. 282 shows $\sigma(\nu)$ having the same crossover from the ω^n dependence to a constant value of primitive relaxation in another fast glassy Ag ion conductor $0.5Ag_2S{-}0.5GeS_2$ at 273 K after subtracting the vibrational ω^2 dependence from the data.

Fast Crystalline Ionic Conductors

Many-body relaxation dynamics requires interaction between the units. Although disorder fosters interaction, by no means it is essential to observe the vestige of many-body relaxation dynamics. Thus, we can expect to see the crossover to primitive conductivity relaxation in fast crystalline ionic conductors. In fact there are experimental evidences for the crossover in crystalline Na β-alumina [1486, 1522, 1523], Na β''-alumina [1524, 1525], and $RbAg_4I_5$ [1525, 1526]. The crossover of conductivity of Na β-alumina at $\nu_c \approx 10^{10}$ Hz and $RbAg_4I_5$ at about 10^{11} Hz can be seen by inspection of the data presented in the left and right panels of Fig. 283, respectively. For Na β-alumina, the activation energy E_0 of $\sigma(\nu)$ for $\nu > \nu_c$ in the range of $200 < T < 300$ K is ≈ 810 K. On the other hand, the activation energy of dc conductivity E_{dc} is ≈ 1600 K at 300 K and ≈ 1700 K at 200 K (see Fig. 287). The coupling parameter n is ≈0.50 at 300 K and ≈0.53 at 200 K [1522(a)]. From these values, one can verify that the relation $E_0 = (1-n)E_{dc}$ of Eq. (3.5) is satisfied.

The crossover behavior is thus found in the dynamics of ions in fast ionic conductors in the glassy or crystalline state, in the same manner as that observed on the structural relaxation of glassformers including molten CKN by dielectric relaxation (Fig. 8), small molecular and polymeric glassformers by quasielastic neutron scattering (Figs. 4 and 5) and computer simulations (Figs. 6 and 7), and colloidal particle suspension by light scattering (Fig. 9). This universal crossover occurs for all many-body relaxation processes in systems with interactions. If the CM has captured the general physics of complex many-body correlation in relaxation of interacting systems, then it is not surprising that the crossover and other properties are universal, as we have seen in various ionic conductors and in other systems that are neither ionic conductors nor glassformers, which we discuss later on in the chapter.

Susceptibility Minimum of Glassy Ionic Conductors Well Fit to Mode Coupling Theory (MCT)

At lower temperatures where the conductivity relaxation time τ_σ is not as high to see the crossover to primitive relaxation, the $\varepsilon''(\nu)$ spectra of the fast solid-state ionic conductors show up as minima at high frequencies just like the susceptibility minima of glass-forming substances. The latter, when well fit by the predictions of the idealized MCT, often has been taken as confirmation of the theory for glass transition, as has been claimed [32] for susceptibility data from neutron and light scattering as well as dielectric susceptibility $\varepsilon''(\nu)$ spectra of CKN and CRN. In brief, the MCT prediction [31, 32] for the minimum in the dynamic susceptibility $\chi''(\nu)$ or $\varepsilon''(\nu)$ at high frequencies ν and temperatures higher than T_c is

$$\chi''(\nu) = \chi''_{\min}\left[a(\nu/\nu_{\min})^{-b} + b(\nu/\nu_{\min})^{a}\right]/(a+b), \tag{3.6}$$

where $\chi''_{\min}$ and $\nu_{\min}$ are the height and the location of the minimum, respectively. The exponents a and b are related to each other via the control parameter λ by the

two equations $\lambda = \Gamma^2(1-a)/\Gamma(1-2a) = \Gamma^2(1+b)/\Gamma(1+2b)$, where Γ is the Gamma function. The first equation implies that $a < 0.395$ and hence a pronounced sublinear increase of $\chi''(\nu)$ at $\nu > \nu_{\min}$ is predicted. For $T > T_c$, MCT predicts the following critical temperature dependences:

$$\nu_{\min} \propto (T - T_c)^{1/2a},\ \chi''_{\min} \propto (T - T_c)^{1/2},\ \text{and}\ \tau_\alpha \propto \eta/T \propto (T - T_c)^{-\gamma}, \quad (3.7)$$

where τ_α is the characteristic time of the α-relaxation and $\gamma = (1/2a) + (1/2b)$. It has become a common practice of researchers to check the validity of the MCT equations (3.6) and (3.7) for the $\chi''(\nu)$ data and determine the critical temperature T_c in the process.

The similarity of the $\varepsilon''(\nu)$ spectra of glassy ionic conductors to the susceptibility spectra of glass-forming liquids invites fitting the former to the predictions of MCT. This has been done [1494] on the dielectric loss data of the fast glassy ionic conductor $0.48(AgI)_2{-}0.52Ag_2SeO_4$ obtained by Cramer and Buscher [1528] and is shown in Fig. 284 (left). The shapes of the minima of $\varepsilon''(\nu)$ are well fit by Eq.

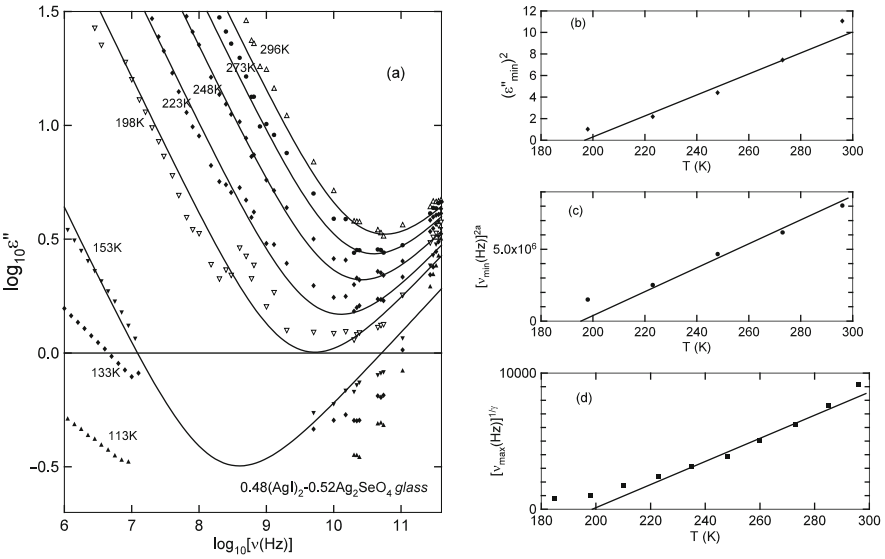

Fig. 284 (**a**) Frequency dependence of the dielectric loss of the glassy ionic conductor $0.48(AgI)_2{-}0.52Ag_2SeO_4$ at 296, 273, 248, 223, 198, 153, 133, and 113 K (*from top to bottom*). *Symbols* stand for experimental data from [1528] and are replotted here. The *solid lines* are fits using the MCT expression, Eq. (3.6), with $\lambda = 0.176$ ($a = 0.32$ and $b = 0.614$). Temperature dependences of $(\varepsilon''_{\min})^2$ is shown in (**b**), $(\nu_{\min})^{2a}$ in (**c**), and $(\nu_{\max})^{1/\gamma} \equiv (1/2\pi\tau_\alpha)^{1/\gamma}$ in (**d**). *Straight lines* in (**b**), (**c**), and (**d**) are fits to linear dependence on $(T{-}T_c)$ of these quantities according to the predictions of MCT by Eq. (3.7). Extrapolation of the linear fits determines T_c. It lies within the range of $196 < T_c < 210$ K from the extrapolations of the three quantities. All figures are redrawn from the data in [1494]

(3.5) from the MCT β-process, and the critical laws of MCT equation (3.7) are also obeyed as shown by the other plots in Fig. 284 and like that found for CKN shown in Fig. 285 [1418]. Notwithstanding the success, it does not seem possible that a fluid theory based on density fluctuations like MCT is applicable to motions of atomic size ions in the matrix of solid-state ionic conductors, glassy or crystalline. This exercise demonstrates that susceptibility minimum and the associated two-step decay of the intermediate scattering function are generally found in relaxation of other interacting systems beyond the glass-forming liquids and can have similar shapes. Moreover, the good fit of the susceptibility by the MCT predictions of the minimum by Eq. (3.6) and the critical laws Eq. (3.6) found in a case where the theory should not apply is an admonition of the danger of validating the MCT as the theory of fast relaxation in glass-forming liquids from merely the good fits to their susceptibility data such as that shown in Fig. 285.

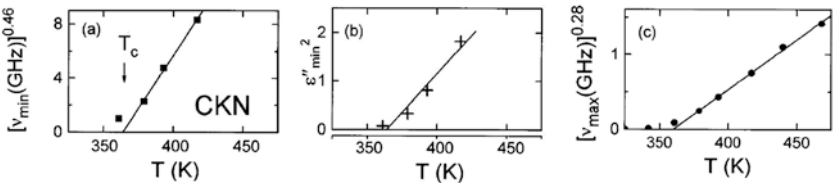

Fig. 285 Temperature dependence of various parameters obtained from the analysis of the high-frequency data of CKN in terms of MCT. The *solid lines* are in accord with the laws given by Eq. (3.7) with a critical temperature of 360 K. Reproduced from [1418] by permission

Susceptibility Minimum of Glassy Ionic Conductors Is Actually Caused by the NCL of Caged Ions

In the case of fast ionic conductors, glassy or crystalline, the nearly constant loss (NCL) is a well-known and well-observed contribution to the dielectric loss that goes back to as early as 1946 [1529−1531], is discussed in the book by Wong and Angell in 1976 [1055], extended to a gigahertz range for the first time by Robert Cole and coworkers in 1989 [1532], and followed by many works [124, 1056−1061, 1533−1535]. Hence, it is more or less certain that the minimum in the $\varepsilon''(\omega)$ of fast ionic conductors is due to the NCL lying in between the vibration absorption at high frequencies and the ω^{-n} dependence at lower frequencies contributed by the ion conductivity. This occurs when the conductivity relaxation time becomes short to limit the range of the NCL and the $\varepsilon''(\omega)$ minimum is observed [1494].

Crossover of Temperature Dependence of σ_{dc} at High Temperatures

We have shown before in Section 2.2.1.2 for glass-forming liquids that another way to see the crossover to primitive relaxation is by the change in T dependence of the viscosity at very low values corresponding to the structural relaxation time τ_α of

the order of picoseconds. The analogy in the case of ion dynamics in fast glassy or crystalline ionic conductors is the change in T dependence of the dc conductivity $\sigma_{\rm dc}$, which reflects the corresponding change of the conductivity relaxation time τ_σ according to the Maxwell relation $\sigma_{\rm dc} = \epsilon_0 \varepsilon_\infty / < \tau_\sigma >$. Here $\epsilon_0 = 8.854 \times 10^{-14}$ F/cm is the permittivity of free space, ε_∞ is the high-frequency dielectric constant, and $< \tau_\sigma >$ is the mean relaxation time. At lower temperatures where $\tau_\sigma << \tau_{\rm c}$ and the correlation function is $\exp\left[-(t/\tau_\sigma)^{1-n}\right]$, τ_σ has the Arrhenius T dependence

$$\tau_\sigma(T) = \tau_\infty^* \exp(E_{\rm a}^*/kT), \tag{3.8}$$

and $< \tau_\sigma >= \left[\Gamma(1/\beta)/\beta\right] \tau_\sigma$, where $\beta \equiv (1-n)$, and Γ stands for the gamma function [55]. The activation energy $E_{\rm a}^*$ and the prefactor τ_∞^* are usually anomalous because of many-ion relaxation due to ion−ion interactions. The temperature dependence of τ_σ is Arrhenius with a constant activation energy $E_{\rm a}^*$ provided that n does not change with temperature. If n decreases with increasing temperature, the Arrhenius T dependence no longer holds as seen in the crystalline ionic conductors such as Na β-alumina [1486] and LLTO [1482] and in some very fast glassy ionic conductors such as $0.525Ag_2S{+}0.475(B_2S_3{:}SiS_2)$ at all temperatures below $T_{\rm g}$ [1536].

On raising the temperature, τ_σ becomes shorter and when it is of the order of picoseconds or shorter, $t_{\rm c}$ is crossed and primitive motion of ions takes over with correlation function given by $\exp(-t/\tau_0)$ with

$$\tau_0(T) = \tau_\infty \exp\left(E_{\rm a}/kT\right) \tag{3.9}$$

and now $< \tau_\sigma >= \tau_\sigma$. The primitive activation energy $E_{\rm a}$ can be identified with a realistic energy barrier of an independent ion hop. The reciprocal of the prefactor τ_∞ is the attempt angular frequency, which should correspond to some peak frequency of the infrared or Raman spectrum. It follows from Eq. (3.2) that

$$E_{\rm a} = (1-n)E_{\rm a}^* \quad \text{and} \quad \tau_\infty = (t_{\rm c})^n (\tau_\infty^*)^{1-n}. \tag{3.10}$$

The temperature dependence of τ_0 is mirrored by that of the measured $\sigma_{\rm dc}$. Therefore, on increasing T, the T dependence of $\sigma_{\rm dc}$ will eventually cross over to the Arrhenius T dependence having the same activation energy $E_{\rm a}$, albeit it may be slightly modified at the higher temperatures when $1/\tau_0$ approaches the vibration frequencies. These properties associated with the expected crossover of $\sigma_{\rm dc}$ at high temperatures have been found in many ionic conductors [1538] including the molten salt CKN, fast glassy ionic conductors such as $0.48(AgI)_2{-}0.52Ag_2SeO_4$ [1528] and $0.525Ag_2S{+}0.475(B_2S_3{:}SiS_2)$ [1536, 1537], and crystalline ionic conductors such as yttria-stabilized zirconia, $(ZrO_2)_{1-x}(Y_2O_3)$ [1539−1543]. As an example, $\sigma_{\rm dc}$ data of yttria-stabilized zirconia (YSZ) are shown in Fig. 286 [1539]. In the lower temperature regime, where $\sigma_{\rm dc}$ has the Arrhenius T dependence,

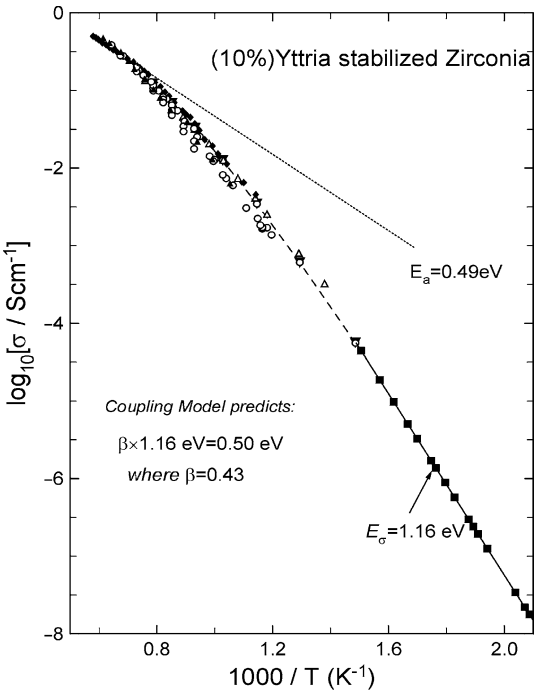

Fig. 286 σ_{dc} data of yttria-stabilized zirconia. Reproduced from [1539] by permission

$\sigma_{dc}(T) = \sigma^*_\infty \exp(-1.14\ \text{eV}/kT)\ \Omega^{-1}\,\text{cm}^{-1}$; from experimentally measured frequency dispersion, the oxygen ion hopping correlation function was found to have the Kohlrausch function with $n = 0.56$.

As temperature increases, $\sigma_{dc}(T)$ becomes non-Arrhenius, but at the highest temperatures, on approaching 1 $\Omega^{-1}\,\text{cm}^{-1}$, it returns to another Arrhenius dependence described by $\sigma_{dc}(T) = 10^{3.6} \times \exp(-0.49\,\text{eV}/kT)\,\Omega^{-1}\text{cm}^{-1}$ Such behavior is evidence of crossover from primitive conductivity relaxation to coupled conductivity relaxation because at the high conductivity levels approaching 1 $\Omega^{-1}\,\text{cm}^{-1}$, the conductivity relaxation times are likely to be comparable with $t_c \approx 2$ ps. For YSZ, the value of ϵ_∞ is 28 [1541], and hence from the Maxwell equation $\sigma_{dc} = \varepsilon_0\varepsilon_\infty / < \tau_\sigma >$, $\sigma_{dc} = 1\ \Omega^{-1}\,\text{cm}^{-1}$ corresponds to $< \tau_\sigma >= 2.5 \times 10^{-12}$ s. Oxygen−oxygen ion interaction slows down the conductivity at lower temperatures when $\tau_\sigma >> t_c$, and its higher activation energy $E^*_a = 1.16\,\text{eV}$ is correctly predicted from the smaller (primitive) activation energy ($E_a = 0.49$ eV) at high temperatures by Eq. (3.5). This can be verified by the equation $0.49\ \text{eV} = (1-n)\,1.16\,\text{eV}$ being satisfied if $n = 0.57$, which is close to the value of 0.56 independently determined by fitting the frequency dependence of the conductivity relaxation data by the Kohlrausch function [1492, 1542].

Figure 287 shows that the dc conductivity of Na β-alumina also crosses over to a weaker T dependence when σ_{dc} exceeds about 0.4 $\Omega^{-1}\ \text{cm}^{-1}$, which corresponds to $< \tau_\sigma >= 1.0 \times 10^{-11}$s because ε_∞ is 50 [1522a]. This indicates that t_c for

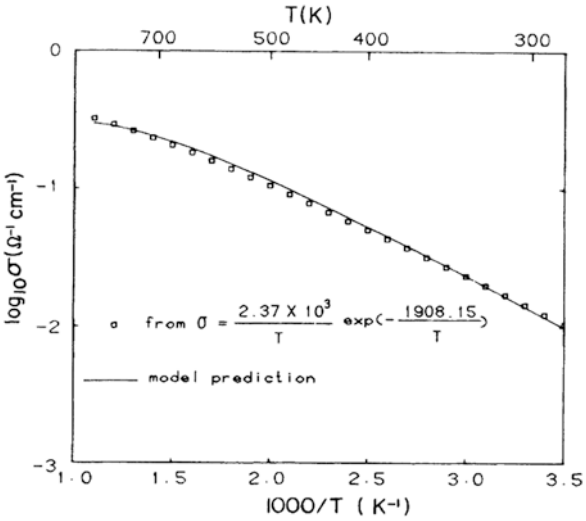

Fig. 287 σ_{dc} data of Na β-alumina (*open circles*). From [1522(a)] by permission

Na β-alumina is about 1.0×10^{-11}s and $\nu_c = 1.6 \times 10^{10}$ Hz. Interestingly, this is nearly the same as the frequency at which the ac conductivity $\sigma(\nu)$ crosses over to the plateau value at higher frequencies (see the left panel of Fig. 283). Thus, there is consistency in determining the crossover to primitive relaxation from temperature dependence of σ_{dc} and from frequency dependence of isothermal $\sigma(\nu)$. Earlier in connection with the left panel of Fig. 283, the relation $E_0 = (1-n)E_{dc}$, has been verified for Na β-alumina. Except for the change in notation, this relation is the same as $E_a = (1-n)E_a^*$ in Eq. (3.10).

The values of E_a calculated in the same way by Eq. (3.10) from the values of E_a^* and n deduced from the data at lower temperatures of many ionic conductors, glassy or crystalline, are given in Table 3.1. Each is about the same as or slightly larger than (but by no more than 20%) the value of E_a obtained from the high-temperature σ_{dc} data which have τ_σ shorter than t_c as described above. Furthermore, the reciprocal of the primitive attempt time τ_∞ calculated by Eq. (3.10) from the anomalous τ_∞^* is also in rough agreement with the value deduced from the high-temperature σ_{dc} data after the crossover. It corresponds well to the peak angular frequency of vibrational spectrum. These good correspondences between the calculated τ_∞ and E_a from the experimentally determined parameters τ_∞^*, E_a^*, and n in the glassy state with their counterparts at high temperature are expected because both sets of parameters are for independent diffusion of the ion, and the difference between them is caused only by the difference in T and density. These changes should not have a large effect on the primitive attempt frequency and the activation energy of local and independent hopping of the ion. There are cases in which n decreases with increasing temperature and approaches zero value while τ_σ is still longer than t_c. This causes the crossover of T dependence of σ_{dc} data to occur at temperature for which τ_σ is still longer than t_c, but the relations in Eq. (3.10) are still valid.

Table 3.1 Ionic transport and conductivity relaxation parameters. For the glass-forming melts, $\beta \equiv (1-n)$ and E_a^* were obtained in the glassy state from conductivity relaxation measurements, while the activation energies E_a were obtained from the high-temperature melt dc conductivity data. For some glassy ionic conductors, the activation energies E_a^{glass} were obtained from neutron scattering or high-frequency microwave and far-infrared conductivity data at temperatures all within the glassy state. All activation energies are in units of kJ/mol

	β	E_a^*	βE_a^*	E_a	E_a^{glass}	$\beta E_a^*/E_a$
Glass-forming ionic conductors						
$LiCl–7H_2O$	0.46	34	15.6	14.4		1.08
$CdF_2–LiF–AlF_3–PbF_2$	0.77	109	83.9	68.4		1.23
ZBLAN20	0.68	85	57.8	50		1.16
ZBLAN10	0.66	79	52.1	46		1.13
ZBLA	0.61	72	43.9	36		1.22
$(Li_2O)–3(B_2O_3)$	0.52	84	43.7	40		1.09
$(Na_2O)–3(SiO_2)$	0.55	64	35.2	33.5		1.05
$0.56Li_2O–0.45LiBr–B_2O_3$	0.44	47.1	20.7		21.1	0.98[a]
$AgPO_3$	0.66	49.5	32.7	28.5		1.14
$(AgI)_{0.1}–(AgPO_3)_{0.9}$	0.59	43	25.4	22.5		1.13
$(AgI)_{0.2}–(AgPO_3)_{0.8}$	0.57	39.5	22.5	19.8		1.14
$(AgI)_{0.3}–(AgPO_3)_{0.7}$	0.54	32.9	17.8	15.6		1.14
$(AgI)_{0.4}–(AgPO_3)_{0.6}$	0.51	32.0	16.3	13.3		1.23
$(AgI)_{0.5}–(AgPO_3)_{0.5}$	0.48	26.9	12.9	10.1	8.7	1.27
$(AgI)_{0.6}–(AgPO_3)_{0.4}$	0.48	26.9	12.9	7.9		1.29
$(AgI)_{0.7}–(Ag_2MoO_4)_{0.3}$	0.44	19.3	8.5	9.0		0.95
$0.48(AgI)_2–0.52Ag_2SeO_4$	0.51	25.1	12.8	13.6		0.94
$(Ag_2S)_{0.5}(GeS_2)_{0.5}$	0.45	32.8	14.8		14.5	1.02[a]
Crystalline conductors						
Na β-Al_2O_3	0.5	13.4[b]	6.7	6.8[c]	6.74	0.99
$RbAg_4I_5$	0.47[d]	9.8[c]	4.6		4.2[c]	1.09[a]
$(Y_2O_3)_{0.095}(ZrO_2)_{0.905}$	0.43	111.9	48.2	48.2		1

[a]Calculated from the ratio $\beta E_\sigma / E_a^{glass}$.
[b]At 300 K.
[c]Obtained by plotting log σ against $1/T$.
[d]Estimated from log σ vs. log f data.

Anomalously Short Prefactor τ_∞^*

In Fig. 287, we show the low-temperature conductivity relaxation data of (9.5%)YSZ from León et al. [1542, 1539, 1540] in terms of $\tau_\sigma(T)$. Its temperature dependence is Arrhenius as indicated by the straight line through the data points in the figure, which corresponds to

$$\tau_\sigma\,(T) \equiv \tau_\infty^* \exp\left(E_a^*/kT\right) = 10^{-16.44} \exp\left(1.16\ eV/kT\right)\ \text{s}. \tag{3.11}$$

The prefactor τ_∞^* of the experimentally observed $\tau_\sigma(T)$ is very short and its reciprocal corresponds to an unphysically high attempt frequency of the oxygen ions. On the other hand, the independent hopping relaxation times $\tau_0(T)$ calculated from $\tau_\sigma(T)$ via Eq. (3.5) with $t_c = 2$ ps are given by

$$\tau_0\,(T) = \tau_\infty \exp\left(E_a/kT\right) = 10^{-13.74} \exp\left(0.50\ eV/kT\right)\ \text{s}, \tag{3.12}$$

and it is represented by the thicker dashed line in Fig. 288. Remarkably, this calculated $\tau_0(T)$ has nearly the same value as well as temperature dependence as $\tau_\sigma(T)$ at high temperatures. This is no surprise because $\tau_\sigma(T)$ is reaching $t_c = 2\,\text{ps}$ at the high temperatures, and hence it crosses over to $\tau_0(T)$. The reciprocal of the prefactor τ_∞ of the calculated τ_0 now has the magnitude of an attempt frequency, as it should.

The actual attempt frequency of oxygen ions in YSZ was determined experimentally from the hyper-Raman spectrum obtained by Shin and Ishigame [1544]. The

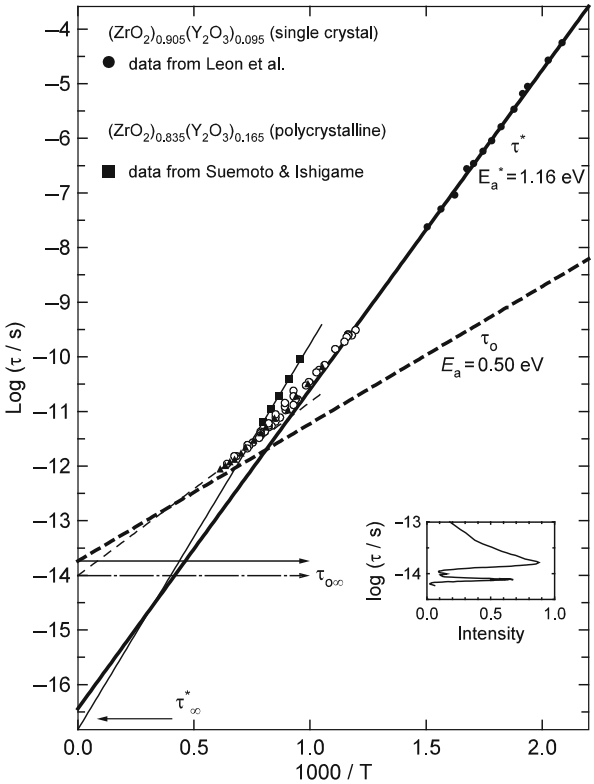

Fig. 288 *Closed circles* and *filled squares* are the relaxation times τ obtained from the oxygen ion conductivity relaxation data (by León et al. [1542]) and quasielastic light-scattering data (by Suemoto and Ishigami [1545]) of YSZ. The *inset* shows the hyper-Raman spectrum from Shin and Ishigami [1544]. *Open circles* and *closed triangles* are τ deduced from dc conductivity data. The *thick solid* and *thin solid lines* through the data points are Arrhenius fits. The *thick* and *thin broken lines* represent the independent relaxation time τ_0 calculated from τ of conductivity relaxation (*thick solid line through circles*) and from quasielastic light scattering (*thin solid line through closed squares*), respectively. The intercepts of the *broken lines* give prefactors $\tau_{0\infty}$ (values indicated by the two horizontal arrows) in good agreement with the frequencies in the narrow band at 690 cm^{-1} of the hyper-Raman spectra shown in the inset. Reproduced from [1482] by permission

vibrational modes shown have displacement of the oxygen ion toward the vacancy and are candidates for the vibrational frequency. Shin and Ishigame argued that the highest frequency narrow band located at 690 cm^{-1}, corresponding to time of $(\omega_\infty)^{-1} = 10^{-14.1}$ s, contributes most effectively to the hopping of the oxygen ions and can be identified by their attempt frequency. Having determined the reciprocal of the true attempt (angular) frequency ω_∞ of the oxygen ions from experiment to be $10^{-14.1}$ s, comparison of it can be made in Fig. 288 with the prefactors τ^*_∞ and τ_∞. The figure has used the notation $\tau_{0\infty}$ instead of τ_∞. The true angular attempt frequency $(\tau_\infty)^{-1}$ deduced from the CM is only 2.4 times smaller than the experimentally determined ω_∞. This small discrepancy between $(\tau_\infty)^{-1}$ and ω_∞ is well within the uncertainty in determining $\tau_0(T)$ from Eq. (3.10) due to experimental errors in n and $\tau_\sigma(T)$ obtained by León et al. The upper horizontal arrow in Fig. 288 indicates the good correspondence between τ_∞, determined by the intercept with the y-axis at $1/T = 0$, and $(\omega_\infty)^{-1}$ from the hyper-Raman spectrum depicted by the inset. On the other hand, as mentioned earlier, the angular frequency $1/\tau^*_\infty = 10^{16.4}\text{s}^{-1}$ is unphysical because its value is more than 200 times higher than the vibrational frequency ω_∞.

Quasielastic light scattering (QELS) in YSZ by tandem Fabry–Perot interferometry was measured by Suemoto and Ishigame [1545] using the same samples as in the hyper-Raman scattering experiment. Light scattering is due to fluctuation of the polarizability caused by ionic motion. They found that the shape of the scattered light intensity peak as a function of temperature taken at constant frequency f, in the range from 1.8 to 24 GHz is non-Lorentzian and in good agreement with that coming from a correlation function that has the Kohlrausch form. The dependence of the temperature of the intensity maximum on f is converted to a dependence on $(2\pi f)^{-1} \equiv \tau^*_{\text{QELS}}$ and the data are shown in Fig. 287 by closed squares. The thinner straight line through the data point is the best fit to an Arrhenius temperature dependence:

$$\tau^*_{\text{QELS}} \equiv \tau^*_{\text{QELS},\infty}\exp\left(E^*_{\text{a,QELS}}\Big/kT\right) = 10^{-16.82}\exp\left(1.40\ \text{eV}\Big/kT\right). \qquad (3.13)$$

The unphysically high apparent attempt frequency $\tau^*_{\text{QELS},\infty}$ is again evident from the prefactor. The QELS correlation time τ^*_{QELS} has a slightly larger activation energy than the conductivity relaxation time $\tau_\sigma(T)$ obtained by León et al. [1542]. This difference arises because the concentration of yttria is higher in the sample studied by QELS than that by conductivity relaxation (16.5 vs. 9.5 mol %) and it is known from conductivity measurement that E^*_a increases with yttria content when above roughly 8 mol%. The spectral shape is well fitted by an expression proportional to $\chi'(\omega)\big/\omega$, where $\chi'(\omega)$ is the imaginary part of the susceptibility function calculated [1544] by a Fourier transform of the time derivative of the Kohlrausch function. In the process, the coupling parameter n_{QELS} was determined to have the value of 0.55. The independent ion hopping correlation time $\tau_{\text{QELS, o}}$ calculated from τ^*_{QELS} has the Arrhenius dependence

$$\tau_{\text{QELS,o}}(T) \equiv \tau_{\text{QELS},\infty}\exp\left(E_{\text{a,QELS}}\big/kT\right) = 10^{-14.0}\exp\left(0.63\ \text{eV}\big/kT\right)\ \text{s} \qquad (3.14)$$

and is plotted as a function of temperature in Fig. 288 (the thinner dashed line).

The situation in QELS is similar to conductivity relaxation in that the experimentally determined attempt frequency $1/\tau^*_{QELS,\infty}$ is too high to be real. However, the attempt frequency $\left(\tau_{\mathrm{QELS},\infty}\right)^{-1}$ of the independent ionic hopping motion deduced by the CM nearly coincides with the measured frequency of the vibrational mode (690 cm^{-1}). The near coincidence is indicated by the lower horizontal arrow located at the intercept of $\tau_{\mathrm{QELS,o}}\,(T)$ with the y-axis at $(1000/T) = 0$. This horizontal arrow points almost at the 690-cm^{-1} peak position of the observed vibrational band. Thus, the QELS data reaffirm the interpretation of the CM that $\tau_{\mathrm{QELS,o}}$ and τ^*_{QELS} are the ion hopping correlation time without and with the effects of many-body interactions between the ions, respectively.

The Meyer–Neldel Rule or Compensation Law

The many-body effects simultaneously make the prefactor τ^*_∞ unphysically short and the activation energy E^*_a larger than the true activation energy E_a. This dual effect is sometimes referred to as the Meyer–Neldel rule [1546] or the compensation law. It makes repeated appearance in other interacting systems, some of which are to be shown later.

Quasielastic Neutron Scattering Studies of Glassy Ionic Conductors

Quasielastic neutron scattering (time of flight) measurements at short times (in the picosecond range) of the ionic diffusion coefficient as a function of temperature in superionic glasses and short-time ion diffusion in fast ion glasses including the systems $\mathrm{AgI–AgPO_3}$ and $\mathrm{Ag_2S–GeS_2}$ with and without AgI have been made by two groups [1547–1550]. It was found that the activation enthalpy of the short-time diffusion coefficient E_a is smaller than that of the dc conductivity and approximately equal to βE^*_a [1522(b), 1523, 1058, 1551]. Here β is the Kohlrausch exponent and E^*_a is the activation enthalpy of conductivity relaxation observed at much lower temperatures and frequencies. These neutron scattering experiments measure the ion diffusion with correlation times of the order of picoseconds. The short-time diffusion E_a from neutron scattering is compared with βE^*_a calculated from the long-time conductivity relaxation data in Table 3.2. The good agreement between E_a and βE^*_a suggests the crossover of dynamics near 1 ps.

3.2.3.2 Entangled Polymer Chains

Crossover from Primitive (Rouse) Dynamics to Many-Chain Cooperative Dynamics

The length scale of entanglement interaction (i.e., the entanglement distance) depends on the polymer but usually is of the order of a few nanometers. The radius

Table 3.2 Activation enthalpies E_a of 0.5AgI–0.5$AgPO_3$ [1547, 1548] and Ag_2S–GeS_2 [1549, 1550] from short-time ionic diffusion obtained by neutron time-of-flight measurements. The Kohlrausch exponent $\beta \equiv (1-n)$ and the activation enthalpies E_σ of conductivity relaxation observed in the same glasses at lower temperatures and frequencies in the many-particle hopping region are also included. The near equality between E_a and βE_σ is found, consistent with the change to independent relaxation at times shorter than $t_c \approx 2$ ps and probed by quasielastic neutron scattering (QENS)

Glass	E_a^*	$\beta \equiv (1-n)$	βE_a^*	E_a (QENS)
AgI–$AgPO_3$	21 (kJ/mol)	0.44	9.2 (kJ/mol)	8.7 (kJ/mol)
Ag_2S–GeS_2	0.34 eV	0.45	0.153 eV	0.15 eV

of gyration of the near-Gaussian chain depends on the chain length and can be even larger. The length scale of interaction between entangled chains in polymer melts is much larger than that between repeat units of the same polymer. Consequently, the strength of interaction between entangled chains is weaker than that between repeat units and we expect that the crossover time t_c from many-chain complex dynamics to primitive single-chain dynamics would be much longer than 1 or 2 ps, the crossover time found for local segmental motion in polymers and for structural relaxation of small molecular liquids and ionic conductivity relaxation. The single-chain dynamics without considering chain–chain entanglement interactions is given by the time-honored Rouse model modified for undiluted polymer [29], which has proven to give excellent description of the viscoelastic properties of low molecular weight unentangled polymers except at temperatures close to T_g [29, 1552].

Evidence of crossover from cooperative many-chain dynamics to Rouse dynamics at t_c of the order of nanoseconds can be found from the neutron spin echo spectroscopic data of coherent scattering from poly(ethylene propylene) copolymer and poly(dimethylsiloxane) chains by Richter et al. [1553]. They found the Rouse dynamics at short times from the experimental intermediate scattering function $S(Q,t)$ but it ceases to hold at times longer than a few nanoseconds, after which the dynamics slows down as expected for cooperative many-chain dynamics as shown in Fig. 289.

3.2.3.3 Colloidal Suspensions

Hard-Sphere Colloidal Particles

The diffusion of colloidal particles with a mean radius of about 10^2 nm [141, 143] suspended at high concentrations in a liquid constitutes another problem of relaxations in a many-body system with hard-sphere interaction. This subject has been discussed before in Section 2.2.1.1 and Fig. 9 shows the mean-square displacement $< r^2(t) >$ obtained from the light-scattering dynamic structure factor $S(Q,t)$ by the relation $S(Q,t) = \exp(-Q^2\langle r^2(t)\rangle/6)$ at particles volume fraction $\phi = 0.465$. $< r^2(t) >$ has $t^{1.0}$ dependence for t<2 ms and crosses over to assume a fractional power $t^{0.65}$ dependence for t>2 ms, which eventually gives way to another $t^{1.0}$ dependence for t>0.2 s. The first crossover in the neighborhood defined by

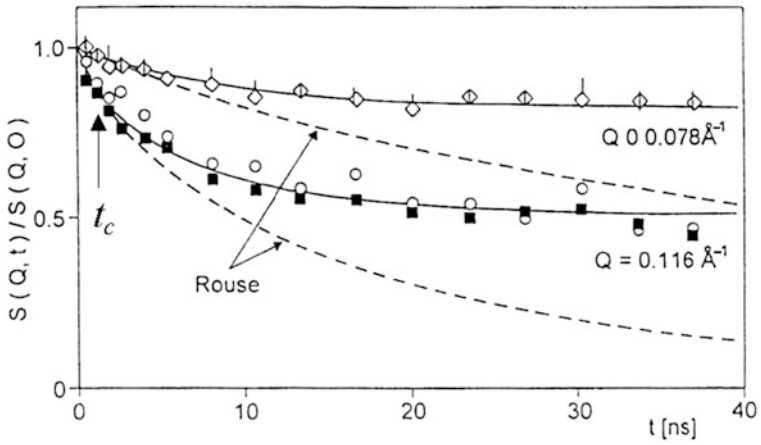

Fig. 289 Evidence of such a t_c can be found from the neutron spin echo spectroscopic data of coherent scattering from poly(ethylene propylene) copolymer and poly(dimethylsiloxane) chains by Richter et al. [1553]. The intermediate scattering function $S(Q,t)$ follows that of the Rouse dynamics (*dashed line*) but ceases to hold at times longer than a few nanoseconds, after which the dynamics slows down. Same data of polymers in dilute solution (not shown) follows the Rouse dynamics. Reproduced from [1553] by permission

2ms $< t <$ 8 ms is due to the change of the particle diffusion correlation function from $\exp(-t/\tau_0)$ to $\exp\left[-(t/\tau)^{1-n}\right]$, with $n = 0.35$. Thus, t_c can be taken to be 4 ms. As shown in [1554], the diffusion correlation function $\exp\left[-(t/\tau)^{1-n}\right]$ for $t >$8 ms is responsible not only for the $t^{0.65}$ dependence for $t >$2 ms but also for its crossover to steady-state diffusion near 0.2 s. An analysis of the data for $\phi = 0.57$ was given in [1554], but in retrospect the results from this analysis are doubtful. This is because at higher volume fraction such as $\phi = 0.57$ and above, $S(Q,t)$ or $<r^2(t)>$ is the complicated by the particles being caged for a long period of time. This caged colloidal particle dynamics is equivalent of the "intermediate power law" (IPL) observed in small molecular and polymeric glassformers by optical Kerr effect, and as nearly constant loss (NCL) by and dynamics light scattering and dielectric relaxation discussed before in Sections 2.3.2.6, 2.3.2.23, and 2.3.2.33. Its appearance in $S(Q,t)$ or $< r^2(t) >$ obscures the crossover and makes it difficult to ascertain the relaxation times τ_0.

Aqueous Suspension of Laponite

Also discussed before in Section 2.2.1.1, from dynamic light scattering in aqueous suspension of Laponite, the intermediate scattering function $f(\boldsymbol{q},t)$ at short times has the $\exp(-t/\tau_f)$ dependence, with τ_f having the q^{-2}-dependent normal Brownian motion [338], and thus it is the primitive diffusion in the CM. At longer times, $f(\boldsymbol{q},t)$ follows the time dependence of $\exp[-(t/\tau_s)^{1-n}]$ [343, 344]. In practice, $f(\boldsymbol{q},t)$ was fitted by the sum

$$f(\boldsymbol{q}, t) = A \exp(-t/\tau_{\mathrm{f}}) + (1 - A) \exp[-(t/\tau_{\mathrm{s}})^{1-n}]. \tag{3.15}$$

An analysis of the data in terms of the CM by Zulian et al. gave values of the crossover time t_{c} for samples with different Laponite concentrations [344]. The results of the analysis show that t_{c} becomes shorter on increasing Laponite weight concentration C_{w}, following a linear decrease of $\log_{10}(t_{\mathrm{c}})$ with C_{w}. The value of t_c is ~1 ms at low C_{w} of 0.4 wt% and decreases to ~20 μs at high C_{w} of 3%. This trend is consistent with the CM which predicts that t_{c} is determined by the interaction. Increase of C_{w} certainly enhances the interaction between the rigid discs in the Laponite solutions. From the very original CM [47] reviewed in Section 2.2.1.2, it is clear that stronger the interaction, larger the ω_{c} and shorter the $t_{\mathrm{c}} \equiv (\omega_{\mathrm{c}})^{-1}$. Also found is that the fast and slow relaxation times τ_{f} and τ_{s} of aqueous suspension of Laponite are related by the CM equation (3.3).

3.2.3.4 Semidilute Polymer Solutions

Adding a solvent to an entangled polymer separates the chains further apart, but the chains are still entangled if the length of the chains is long and the concentration is not too low. Such systems are called semidilute polymer solutions. If the crossover from cooperative many-chain dynamics to primitive Rouse dynamics exists, its crossover time t_{c} would be longer than undiluted entangled polymers, which is a few nanoseconds (see Fig. 289), because entanglement interaction is weakened by the presence of the solvent. Figure 290 shows as an example from light-scattering experiment performed on aqueous gelatin solutions a semidilute entangled polymer solution by Ren et al. [776]. The light-scattering dynamic structure factor $S(Q, t)$ shows clear evidence of sharp crossover from exponential decay to Kohlrausch decay at $t_{\mathrm{c}} \leq 10^{-4}$ s for 3 and 7% aqueous gelatin (linear polymer) solutions at $T = 45°\mathrm{C}$ (above gel point) and 27°C (below gel point).

The same was found in pre-gelling silica solution by Martin and Wilcoxon [1555, 1556] using quasielastic light scattering. The initial decay rate is proportional to Q^2, where Q is the scattering vector, indicating it is the primitive relaxation. The slower relaxation that follows has the Kohlrausch stretched exponential time dependence. In the pre-gel silica solution, t_c lies between 10^{-5} and 10^{-4} s, and the Kohlrausch fractional exponent (1–n) is equal to 0.65.

3.2.3.5 Polymeric Cluster Solutions

Similar light-scattering experiments on polymeric cluster solution by Adam et al. [780] and Delsanti et al. [1557] also have the crossover from exponential decay to Kohlrausch stretched exponential decay at t_{c} with similar order of magnitude as semidilute polymer solutions. In all these cases, the Kohlrausch exponent $\beta \equiv (1 - n)$ decreases with increasing concentration of the polymer clusters, naturally caused by increasing coupling between the relaxing units and hence the coupling parameter of the CM.

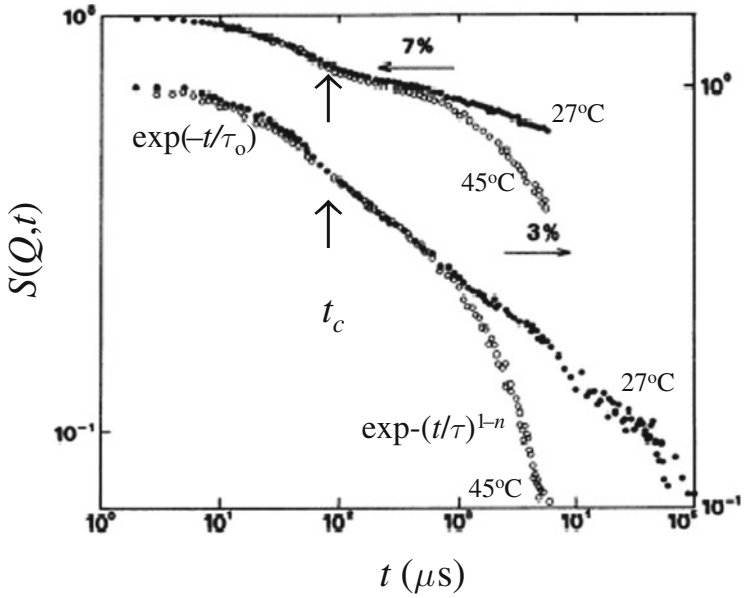

Fig. 290 Light-scattering dynamic structure factor $S(Q,t)$ for 3% (*bottom* and *right* y-axis) and 7% (*top* and *left* y-axis) aqueous gelatin (linear polymer) solutions at $T = 45°C$ (above gel point) and 27°C (below gel point), showing the crossover time $t_c \leq 10^{-4}$ s. The x-axis is logarithm of time in micro seconds ranging from 1μs to 10^5μs. Reproduced from [776] by permission

3.2.3.6 Associating or Aggregating Polymer Solutions

The time correlation data obtained from the dynamic light-scattering (DLS) experiments on polymer solutions of various kinds by Nyström and coworkers [778, 1558–1560] and earlier by others [1561] have revealed the existence of two relaxation modes, one single exponential at short times followed by a Kohlrausch stretched exponential at longer times. The first-order electric field correlation function $g^1(q,t)$ obtained from DLS (see Section 1.3.2) in all these reports was fitted by Eq. (3.15) to deduce the parameters τ_f, τ_s, n, and A, and their q dependences. Here are some examples of associating polymer:

(1) Aqueous solutions of a hydrophobically end-capped poly(oxyethylene) (POE) urethane (HPOEU) by Nyström et al. [778].
(2) Aqueous solutions of associating diblock and triblock poly(oxyethylene)-containing copolymers of the same type by Thuresson et al. [1558].
(3) Semidilute aqueous mixtures of various compositions of oppositely charged and hydrophobically modified polyelectrolytes. In the system, the cationic polymer is a *N*,*N*-dimethyl-*N*-dodecylammonium derivative of hydroxyethylcellulose and the hydrophobically modified polyacrylate, which was chosen as the negatively charged polyelectrolyte [1559].

(4) An example of aggregating polymer solutions is aqueous solutions of low-methoxyl pectins. Pectins are important water-soluble, anionic heteropolysaccharides of plant origin. Structurally they are biopolymers consisting of a linear backbone of randomly connected (1→4)-linked α-D-galactosyluronic acid residues partially esterified with methanol and interrupted by (1→2)-linked α-L-rhamnopyranosyl residues. Low temperatures and increased pectin concentrations promote the formation of multichain aggregates. The time correlation data obtained from dynamic light-scattering experiments revealed, for all solutions with polymer from 0.5 up to 1.5 wt%, the existence of two relaxation modes, one single exponential at short times followed by a Kohlrausch stretched exponential at longer times. In the semidilute regime at 1.5 wt%, on lowering the temperature, chain associations are enhanced in the solutions resulting in increasingly longer values of the Kohlrausch relaxation time of the slow mode, and it has a stronger wave vector dependence. These features have been rationalized in the framework of the CM by Kjøniksen et al. [1560].
(5) Similar results were obtained by Narayanan et al. also by DLS in aqueous solutions of pectin by the addition of calcium chloride to induce gelation [1562].
(6) The crossover was found in two other systems: aqueous alginate modified by association and gelation via reaction by Bu et al. [1563] and semidilute aqueous hyaluronic acid solutions by Maleki et al. [1564(a)].
(7) Similar result was found in rod-like micelles formed at 3 M NaCl, which become increasingly entangled with increasing concentration of the copolymer PEO–PPO–PEO triblock copolymers [1565]. Length of the micellar rods increases with increase in NaCl concentration at constant copolymer concentration. Another system is a thermosensitive methoxy-poly(ethylene glycol)-*block*-poly(*N*-isopropylacrylamide)-*block*-poly(4-styrenesulfonic acid sodium) triblock copolymer having the following composition: $MPEG_{45}$-*b*-$P(NIPAAM)_n$-*b*-P(SSS) with $n = 17$, 48, and 66 [1564(b)]. The fast relaxation mode always is diffusive with $D = 1/\tau_f q^2$.

3.2.4 Anomalous $Q^{-2/(1-n)}$ Dependence of τ

Quasielastic neutron scattering data of molecular glassformers presented in Section 2.2.5.2 have shown that the slow structural α-relaxation time τ_α does not have the normal Q^{-2} dependence on the scattering vector Q, while the fast primitive relaxation time τ_0 does. Instead τ_α has the stronger but anomalous $Q^{-2/(1-n)}$ dependence, where $(1-n)$ is the fractional exponent of the Kohlrausch correlation function of the α-relaxation. This is also the case for non-molecular glassformers including colloidal particle suspension [143] and Laponite [344] from dynamic light-scattering measurements. This is one of several properties of the α-relaxation indicating that they are governed by the dispersion or n, and the anomalies associated with them originate from many-body dynamics. The anomalous $Q^{-2/(1-n)}$ dependence of τ_α is derivable from the CM equations (3.1) or (3.2) simply by substituting the known

or found Q^{-2} dependence of τ_0 into them. If this anomaly of structural relaxation of glassformers is indeed originating from many-body relaxation as proposed in Section 2.2, then it should show up in relaxation of interacting systems which are not glassformers and the relaxation process is entirely different from structural relaxation of glassformers, as long as they are relaxations involving units that are interacting with each other.

Almost all the systems discussed above in Sections 3.2.3.3–3.2.3.6 show that the slow relaxation time τ_s of the Kohlrausch stretched exponential decay in Eq. (3.15) has the anomalous $Q^{-2/(1-n)}$ dependence, while τ_f has the normal Q^{-2} dependence. All relaxations of the systems in Sections 3.2.3.4–3.2.3.6 involve motions of polymer chains totally unrelated to the structural α-relaxation and the glass transition problem. Because these relaxations also exhibit the crossover from exponential to Kohlrausch decay in some neighborhood of t_c, the CM equations (3.1) and (3.2) hold and explain the $Q^{-2/(1-n)}$ dependence of τ_s. For other related applications of the CM, see the review in [1567]. To be precise, τ_s and $(1-n)$ are two separate parameters in the Kohlrausch function. While τ_s has the experimentally determined Q dependence given by $\tau_s \propto Q^{-\alpha_s}$, the exponent (1–$n$) is independent of Q, and it turns out that α_s is in reasonably good agreement with $2/(1-n)$. The systems showing the $Q^{-2/(1-n)}$ dependence of τ_s vary greatly. They include (i) aqueous solutions of linear random coil molecules of swine gelatin, (ii) synthetic polymer (polyurethane) cluster solutions and pre-gelling silica solution, (iii) aqueous solutions of a hydrophobically end-capped poly(oxyethylene) urethane, (iv) aqueous solutions of associating diblock and triblock poly(oxyethylene)-containing copolymers, (v) semidilute aqueous mixtures of various compositions of oppositely charged and hydrophobically modified polyelectrolytes, (vi) aqueous solutions of the biopolymer pectin, alginate, and hyaluronic acid, (vii) rod-like micelles formed by the copolymer PEO–PPO–PEO triblock copolymers in the presence of NaCl, and (viii) aqueous solutions of hydroxypropylcellulose (HPC) by probe diffusion measurements [198, 777, 1566].

Not mentioned in the above is the three-component microemulsion system containing bis(2-ethylhexylsulfosuccinate) (AOT) (surfactant), D_2O, and decane (oil), and the measurements by dynamic light-scattering, small-angle neutron scattering, and neutron spin echo (NSE) spectroscopic measurements by Sheu et al. [1568]. The time-dependent density correlation function exhibits the Kohlrausch form with stretch exponent (1–n), and its relaxation time has the anomalous $Q^{-2/(1-n)}$ dependence.

The $Q^{-2/(1-n)}$ -dependence of τ_s is thus shared by these diverse systems besides the colloidal suspension and Laponite. This suggests that the same $Q^{-2/(1-n)}$ dependence of the structural α-relaxation time of glassformers is a universal manifestation of many-body relaxation.

Before leaving this topic, the data from three systems are shown. All illustrate the increase of n or decrease of the Kohlrausch stretch exponent $\beta \equiv (1-n)$ when interaction is enhanced by one way or the other, as well as corresponding increase of the exponent α_s of the experimentally determined Q dependence $\tau_s \propto Q^{-\alpha_s}$ and the good agreement of α_s with $2/\beta$.

The first example is taken from light-scattering experiment performed on aqueous gelatin solutions, the semidilute entangled linear polymer solutions by Ren et al. [776] shown in Fig. 291. The dynamic structure factor $S(Q, t)$ has been presented in Fig. 290.

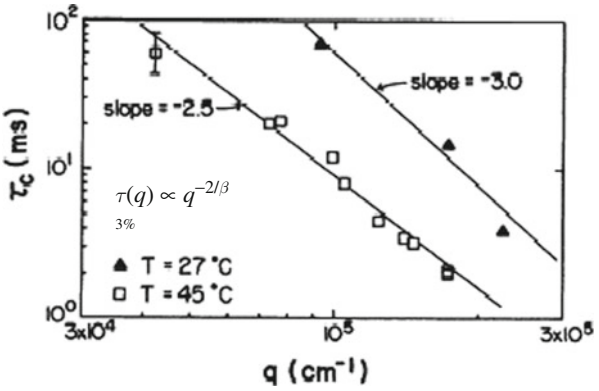

Fig. 291 Data of the slow-chain diffusion relaxation time τ_c (symbols) in aqueous gelatin semidilute solutions (*symbols*) showing its q dependence, which is well described by the $q^{-2/(1-n)}$ dependence (*lines*) predicted by the CM. Reproduced from [776] by permission

The fast-chain diffusion process with exponential decay has the normal q^{-2} dependence for its relaxation time τ_f. The q dependence of the slow polymer chain diffusion time τ_s from the dynamic structure factor $S(q, t)$ is shown by symbols in Fig. 291 for 3% aqueous gelatin solutions (τ_c in the figure). The data at 45°C (open squares) were taken above the gel point (∼30°C) and the Kohlrausch stretched exponential fit to the time dependence of $S(q, t)$ has the stretch exponent $(1 - n) = 0.81$. Also shown in the same figure are the data of τ_c at 27°C, which is below the gel point and the stretch exponent $(1 - n) = 0.67$. The larger n at 27°C is due to enhanced intermolecular coupling in the gel by the presence of cross-links. The lines in the figure have the predicted $q^{-2/(1-n)}$ dependence using exactly the values of 0.81 and 0.67 for (1–n) obtained from the Kohlrausch fits. It can be seen from the figure that these lines well describe the q dependence of τ_c.

The second example come from 0.1, 0.5, and 1.5 wt% of pectin solutions by Kjøniksen et al. [1560]. Part (a) of the left panel of Fig. 292-1 presents the temperature dependence of the stretched exponent β of the Kohlrausch relaxation function of the slow mode for the pectin solutions. Part (b) shows the effects of temperature and polymer concentration on α_s and $2/\beta$, as well as good agreement between these two quantities.

The third example shown in the right panel of Fig. 292-1 comes from the semidilute aqueous mixtures of various compositions of anionic hydrophobically modified polyacrylate (HM-P-) and cationic hydrophobically modified hydroxyethylcellulose (HM-P+) with total polymer concentration of 1 wt% by Tsianou et al. [1559]. Part (a) of the figure presents some examples of the wave vector q dependences of the fast (τ_f^{-1}) and the slow (τ_s^{-1}) inverse relaxation times for several mixture ratios

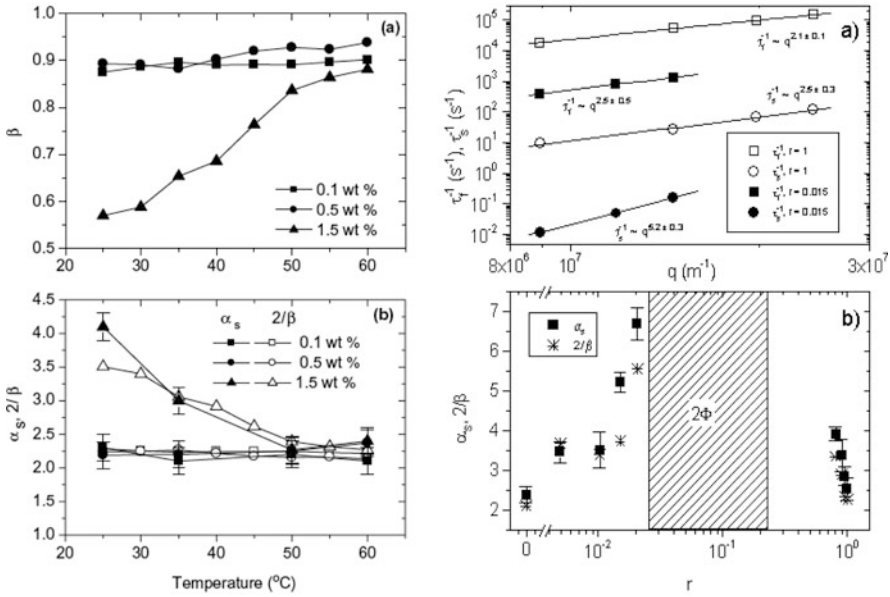

Fig. 292-1 (*Left*) (**a**) Temperature dependence of the stretched exponent β for pectin solutions at the concentrations shown. (**b**) Effects of temperature and polymer concentration on the quantities $2/\beta$ and α_s, illustrating the q dependence of the slow inverse relaxation mode. Reproduced from [1560] by permission. (*Right*) (**a**) Illustration of the wave vector dependences of the fast (τ_f^{-1}) and the slow (τ_s^{-1}) inverse relaxation times for semidilute aqueous mixtures of various compositions of anionic hydrophobically modified polyacrylate (HM-P-) and cationic hydrophobically modified hydroxyethylcellulose (HM-P+) with total polymer concentration of 1 wt% by Tsianou et al. [1559]. The mixture ratio r is indicated. (**b**) Effects of the mixture ratio on the quantities $2/\beta$ (see the main text for explanation) and α_s, illustrating the q dependence of the slow inverse relaxation time. Reproduced from [1559] by permission

indicated. Part (b) shows the effects of the mixture ratio outside the two-phase region (shaded area labeled by 2Φ) on the quantities $2/\beta$ and α_s, and the good correspondence between them. It is understood that the intermolecular interactions are strengthened when approaching the two-phase region because of polymer clustering. Thus the accompanying observed decrease of β and the good agreement between $2/\beta$ and α_s are in accord with the CM predictions [1567].

The fourth example is given by the family of thermosensitive methoxy-poly (ethylene glycol)-*block*-poly(*N*-isopropylacrylamide)-*block*-poly(4-styrenesulfonic acid sodium) triblock copolymers having the following composition: $MPEG_{45}$-*b*-$P(NIPAAM)_n$-*b*-P(SSS) with $n = 17$, 48, and 66 [1564(b)]. The structure of the triblocks is shown by the chemical formula and the illustration on the right side of Fig. 292-2. Overall, there is good agreement between α_s and $2/\beta_s$, where α_s is the power in the observed dependence $\tau_s \propto Q^{-\alpha_s}$ and $\beta_s \equiv (1 - n_s)$ is the Kohlrausch exponent of the stretched exponential correlation function for the slow mode. Remarkably, even the temperature dependences of α_s and $2/\beta_s$ are about the same.

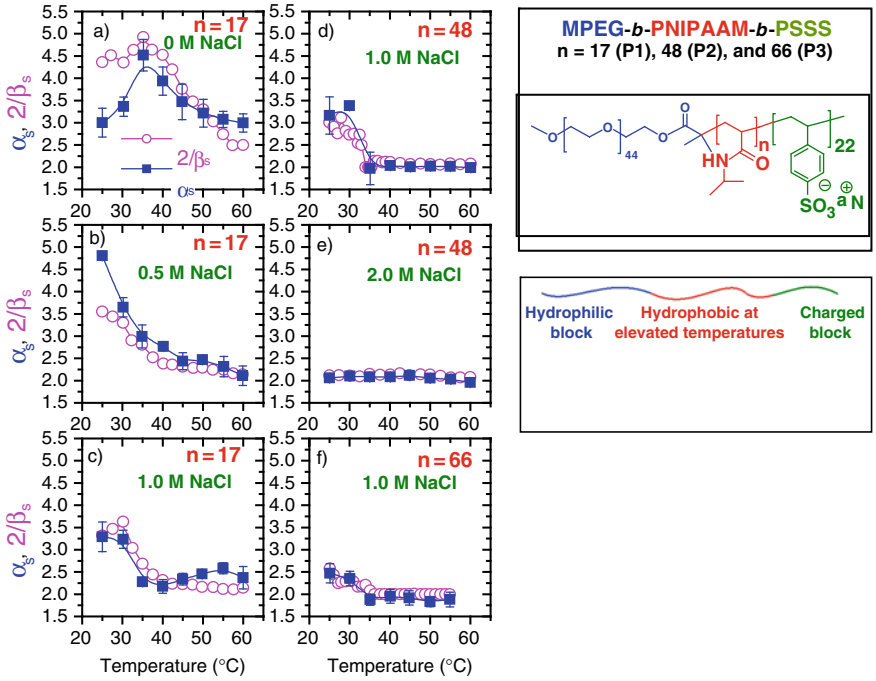

Fig. 292-2 (*Left*) Effects of temperature and salt addition on the quantities $2/\beta$ (see text for explanation) and α_s, expressing the q dependence of the slow relaxation time, for 1 wt% solutions of $M(PEG)_{45}$-*b*-$P(NIPAAM)_n$-*b*-$P(SSS)_{22}$. Courtesy of Bo Nyström. The data shown are to be published as [1564(b)] in the future. (*Right*) Chemical structure and illustration

3.2.5 *Different Correlation Functions of the Same Relaxation Can Have Different Kohlrausch Exponents (1– n), Relaxation Times τ, and T-Dependences*

Previously in Section 2.2.5.6, experimental data of the structural α-relaxation in the same glassformers were presented to show that the Kohlrausch correlation functions $\langle \mu(0)\mu(t)\rangle = \exp[-(t/\tau_\mu)^{1-n_\mu}]$ of different dynamic variables μ can differ in the stretch exponent $(1 - n_\mu)$ and the value of the relaxation time τ_μ as well as its T dependence. This situation occurs when comparing data obtained from different techniques such as translational diffusion, rotational diffusion, dielectric relaxation, dynamic light scattering, mechanical relaxation, and NMR, which involve various dynamic variables. This property has been interpreted as caused by different dynamic variables weighing the effect of many-body relaxation differently, resulting in different degrees of stretching of the α-relaxation to different longer times. Correlation function for dynamic variable μ that is more stretched (i.e., the exponent n_μ appearing in the Kohlrausch function is larger) has longer relaxation time τ_μ and stronger T dependence of τ_μ. These properties are predicted by the CM equations

(3.1) and (3.2) if the primitive relaxation times $\tau_{0\mu}$ of all the dynamic variables are equal or about equal and have the same T dependence. It can be seen from Eq. (3.1) rewritten as

$$\tau_\mu = \tau_{0\mu}(\tau_{0\mu}/t_c)^{n_\mu/(1-n_\mu)} \tag{3.16}$$

that larger n_μ leads to longer τ_μ. Like Eq. (3.2) for the dependence on any variable U, when Eq. (3.16) is simplified to show just different T dependences and rewritten as

$$\tau_\mu(T) \propto [\tau_{0\mu}(T)]^{1/(1-n_\mu)}, \tag{3.17}$$

it clearly shows that larger n_μ leads to stronger T dependence of τ_μ. When specializing to comparison of translation diffusion with viscosity or with probe rotation, these properties constitute the breakdown of Stokes-Einstein (SE) and the Debye-Stokes-Einstein (DSE) relations, the property recognized by many researchers as a key to solve the glass transition problem (see Section 2.2.5.6). Here, experimental data of relaxation in other interacting systems that have nothing to do with structural α-relaxation of glassformers are presented to show the similar properties, and they are thus general behavior of many-body relaxation in interacting systems. This demands that any solution of the breakdown of SE and DSE relations in glassformers proffered has to be general enough to be applicable to the other systems. Since the CM is designed for relaxation and diffusion of any interacting systems, naturally its explanation for the breakdown of SE and DSE relations in glassformers given in Section 2.2.5.6 is general enough to satisfy this requirement.

3.2.5.1 Glassy Ionic Conductors: Conductivity vs. NMR

This subject has been touched before in Section 2.2.1 to support the CM explanation for the breakdown of SE and DSE relations in glassformers. More experimental data and details are given here to stress the universal behavior of relaxation and diffusion in interacting systems.

Experimental Data

The fact that the dynamics of ion diffusion as probed by nuclear spin relaxation (NSR) and electrical conductivity relaxation (ECR) in glassy ionic conductors is significantly different was discovered by Tatsumisago et al. [147, 279] and by Kanert and coworkers [280–282] at almost the same time in 1992 on different ionic conductors. Subsequently, other workers have repeatedly confirmed this anomalous property [283–289] that resembles the breakdown of the DE and DSE laws. Experimentally both the electrical conductivity and NSR correlation functions have the Kohlrausch forms and Arrhenius T dependences for their relaxation times:

$$\phi_M(t) = \exp[-(t/\tau_M)^{1-n_M}], \quad \text{where} \quad \tau_M = \tau_{M,\infty}\exp(E_M/kT) \tag{3.18}$$

and

$$\phi_s(t) = \exp[-(t/\tau_s)^{1-n_s}], \quad \text{where} \quad \tau_s = \tau_{s,\infty} \exp(E_s/kT). \tag{3.19}$$

Notwithstanding, τ_s of the relaxation of the nuclear spin of the diffusing ion is considerably longer than the electrical conductivity relaxation time τ_M. The activation energies E_s of τ_s is larger than E_M of τ_M. At this level, the relations $\tau_s >> \tau_M$ and $E_s > E_M$ from the dynamics of ions are analogues of the relations between the viscosity (or rotation relaxation) and self (or probe)-diffusion, which constitute the breakdown of the SE and DSE relations. Moreover, it was found that $n_s > n_M$, the analogue of $n_\eta > n_D$ or $n_r > n_D$, which is the key to the explanation of the breakdown of the SE and DSE relations by the CM in Section 2.2.5.6. The effect was also found by a Monte Carlo simulation experiment of a disordered Coulomb lattice gas model of the ionic conductor [467, 1569, 1570]. It is also present in the NMR and conductivity relaxation data of the non-glassy fast ionic conductor sodium β-alumina, Na-βAl_2O_3, found by Bjorkstam and Villa [290] as early as 1980 and brought back into attention in 1993 by [291]. These experiments have proven that the decoupling between NSR and conductivity relaxation is a general phenomenon of interacting many-ion dynamics, glassy or crystalline.

Before proceeding further, I hasten to point out that electrical conductivity relaxation (ECR) is a macroscopic probe involving the measurement of capacitance $C(\omega)$ and conductance $G(\omega)$, from which the parallel quantities $\varepsilon^*(\omega)$, $\sigma^*(\omega)$ or $M^*(\omega)$ are obtained. Therefore, the macroscopic electrical conductivity correlation function in Eq. (3.18) fitting the $M^*(\omega)$ is not the microscopic conductivity correlation function $\phi_\sigma(t)$ given by

$$\phi_\sigma(t) = \exp[-(t/\tau_\sigma)^{1-n_\sigma}], \quad \text{where} \quad \tau_\sigma = \tau_{\sigma,\infty} \exp(E_\sigma/kT). \tag{3.20}$$

The Kohlrausch exponents of $\phi_M(t)$ and $\phi_\sigma(t)$ are the same and both denoted by n, because the time dependence or frequency dispersion is faithfully reproduced by the macroscopic measurement. The difference is between the macroscopic τ_M and the microscopic τ_σ, which will be given later, although they have the same activation energy E_σ and hence the prefactors $\tau_{\sigma,\infty}$ and $\tau_{M,\infty}$ differ. To avoid confusion with notations, the relations between the parameters of electrical and microscopic conductivity relaxation are written explicitly as follows:

$$n_M = n_\sigma, \; E_M = E_\sigma, \quad \tau_{M,\infty} \neq \tau_{\sigma,\infty}. \tag{3.21}$$

On the other hand, nuclear spin-lattice relaxation is a microscopic probe of the motion of the mobile ions, and the SLR, $T_1^{-1}(\omega_L, T)$, corresponds to the microscopic correlation function.

Here we show the three examples, all of which involve macroscopic conductivity relaxation measurements and hence τ_M. The first one is from the 1992 work of Kanert and coworkers on a heavy metal fluorozirconate glass with the following composition (in mol%): 27.4ZrF_4, 27.4HfF_4, 19.8BaF_2, 3LaF_3, 3.2AlF_3, 20NaF

(ZBLAN glass; $T_g = 553$ K). The F^- ions are responsible for ionic conductivity, which was measured over ranges of frequencies and temperatures. The conductivity relaxation time τ_M, its activation energy E_σ, and the coupling parameter n_σ determined are shown in Fig. 293 and Table 3.3. The ^{19}F spin-lattice relaxation (SLR) times τ_s has been measured at different Larmor frequencies. The τ_s of ZBLAN was obtained from the ^{19}F spin-lattice relaxation rate $T_{1\rho}^{-1}(\omega_L, T)$ in the rotating frame at Larmor frequencies of 28, 42, and 62 kHz matching the high frequencies used to measure the conductivity relaxation time τ_M [282]. The results of τ_s are shown in Fig. 293, and n_s and E_s determined from fits to temperature dependence of $T_{1\rho}^{-1}(\omega_L, T)$ are given in Table 3.3. All measurements were in the glassy state where the temperature dependences of τ_s and τ_M are undoubtedly Arrhenius, and their difference is brought out by the comparison of the $T_{1\rho}^{-1}(\omega_L, T)$ with the product σT at the *same* frequency of about 25 kHz. The fact that the characteristic temperatures $T_s \approx 525$ K and $T_M \approx 425$ K of τ_s and τ_M, respectively, are so different makes perfectly clear SLR and conductivity relaxation are not the same, although both

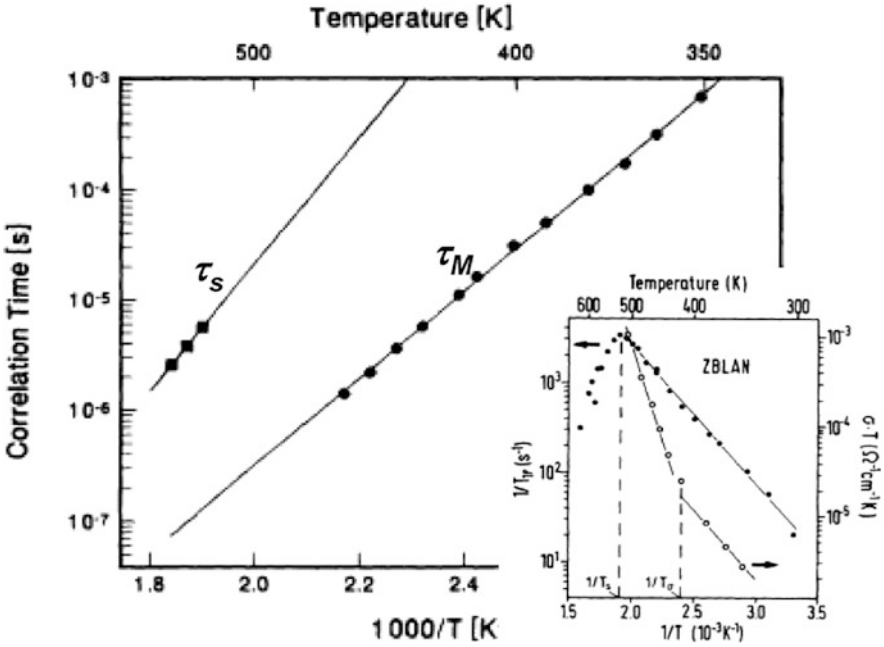

Fig. 293 ZBLAN conductivity correlation time τ_M from data analysis of the electric modulus and NSR correlation time τ_s from frequency dependence of $1/T_{1\rho}$ maxima plotted against $1000/T$. The inset is a comparison of the T dependence of the ionic motion-induced part of the ^{19}F spin-lattice relaxation (SLR) rate $1/T_{1\rho}$ and of σT observed at the *same* frequency of about 25 kHz. These isochronal data clearly show the different temperatures $T_s \approx 525$ K and $T_M \approx 425$ K of the SLR maximum and of the crossover point of σT from one T dependence to another. Reproduced from [282] by permission

Table 3.3 The relaxation time τ_s, activation energy E_s, and coupling parameters n_s for SLR, and the corresponding quantities τ_M, E_σ, and n_s for ECR for three different glassy ionic conductors

Ionic conductor	Dynamic variable U	$\beta_U \equiv (1-n_U)$	E_U^* (K)	$(1-n_U)E_U^*$ (K)
$(Li_2S)_{0.56}(SiS_2)_{0.44}$	*Spin* (SLR)	0.35	5845	2046
$(Li_2S)_{0.56}(SiS_2)_{0.44}$	*M* (ECR)	0.52	3911 (from τ_M)	2034
			4000 (from σ_{dc})	2080
$(LiCl)_{0.6}(Li_2O)_{0.7}(B_2O_3)$	*Spin* (SLR)	0.35	7400	2590
$(LiCl)_{0.6}(Li_2O)_{0.7}(B_2O_3)$	σ (ECR)	0.50	5500	2750
ZBLAN[a]	*spin* (SLR)	0.30	13346	3830
ZBLAN[a]	σ (ECR)	0.44	9284	4085

[a]27.4ZrF, 27.4HfF, 19.8BaF, 3LaF, 3.2AlF_3, 20NaF (in mol%)

measure the motion of the F^- ions. For details of the procedure used to obtain the parameters, see [282].

The second example is the 1992 study by Tatsumisago et al. [147, 279] on Li^+ ion motion in the fast glassy ionic conductor $0.6LiCl–0.7Li_2O–B_2O_3$. The right panel of Fig. 294 is the Arrhenius plot of the correlation time of the mobile Li^+ ion τ_s deduced from ^7Li nuclear spin-lattice relaxation measurement and the macroscopic electrical conductivity relaxation time τ_M from dielectric measurements. In this work, the Larmor frequencies of the SLR in the 10–100-MHz range are much higher than the conductivity relaxation measurements, unlike the rotating frame SLR measurements in the tens of kilohertz range of Kanert and coworkers. Nevertheless, the fact that τ_s is much longer than τ_M and has a larger activation energy E_s than E_σ is clear

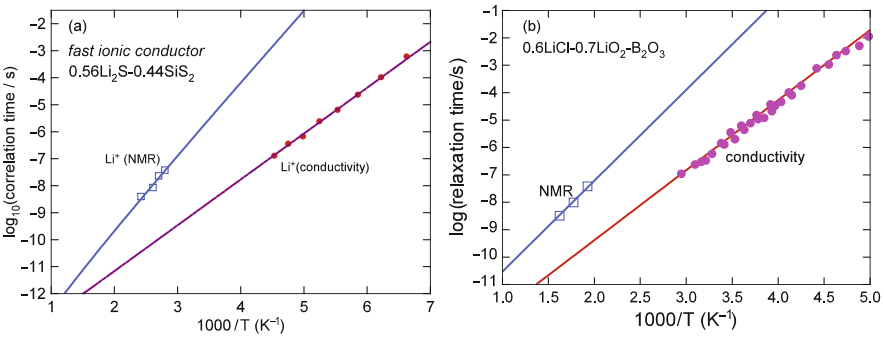

Fig. 294 (**a**) Arrhenius plot of the correlation time of the mobile ion τ_s deduced from ^7Li nuclear spin-lattice relaxation measurement (*open squares*) and the macroscopic electrical conductivity relaxation time τ_σ (•) from measurements of τ_σ. Data from [286] and [292] are replotted here. (**b**) Arrhenius plot of the correlation time of the mobile ion τ_s deduced from ^7Li nuclear spin-lattice relaxation measurement (*open squares*) and the macroscopic electrical conductivity relaxation time τ_σ or τ_{EM} (*closed circles*) from measurements of $0.6LiCl–0.7Li_2O–B_2O_3$. Data from [279] and [291] are replotted here. The *upper full line* is τ_s calculated by the CM (see text)

from the figure. Furthermore, the coupling parameters n_s for SLR and n_σ for conductivity relaxation have been determined from the data. All parameters are given in Table 3.4.

The third example is taken from glassy Li^+ conductor $(Li_2S)_{0.56}(SiS_2)_{0.44}$ by Borsa et al. [286]. The quality of the data is similar to that of Tatsumisago et al., and the Arrhenius plot of τ_s and τ_M shown in the left panel of Fig. 294 shows the same features. All parameters deduced from the data are entered into Table 3.3.

The CM Explanation

The frequency-dependent conductivity $\sigma(\omega)$ is given in Eq. (1.130) by the Fourier transform of the current–current correlation function, or equivalently the velocity–velocity correlation function $\phi_\sigma(t) = N^{-1}\sum_{ij}\langle v_i(0)v_j(t)\rangle$. An expression for $\sigma(\omega)$ in terms of the mean-square displacement is given by Eq. (3.4). In this expression, the Haven ratio [1490] though less than unity is not very small for glassy ionic conductors, which indicates that the tracer diffusion correlation function $\phi_D(t) = \langle r(0)r(t)\rangle$ is only slightly different from $\phi_\sigma(t)$ and the $i \neq j$ cross terms is not important.

If spin-lattice relaxation (SLR) measurements are made using the mobile ion nucleus, and the ion SLR mechanism is caused by time-dependent fluctuations of the nuclear spin coupling energy ω_{ij} between interacting ion pairs (i,j), the resulting SLR rate $T_1^{-1}(\omega_L, T)$ as a function of temperature at the Larmor frequency ω_L is given by the expression $\kappa[J(\omega_L, T) + 4J(2\omega_L, T)]$ [92]. Here κ is the coupling constant and $J(\omega,T)$, the spectral density function, is the real part of the Fourier transform $J(\omega, T) \equiv \mathrm{Re}\int_0^\infty \phi_s(t/\tau_s)\exp(-i\omega t)dt$ of the pair–pair correlation function $\varphi_s(t) = \sum_{i,j} < \omega_{ij}(0)\omega_{ij}(t) >$. If the ion NSR is via magnetic dipole or quadrupolar interactions, it is governed by the correlation function $\phi_s(t) = (1/N)\sum_{i\neq j}(1/N)\sum_{i\neq j}\left\langle F_{ij}^{(q)}(t)\,F_{ij}^{(q)}(0)\right\rangle$, where $F_{ij}^{(q)}(t) = q\sqrt{8\pi/15}\,Y_2(q)\,\Omega_{ij}/r_{ij}^3$, Y_2 is the spherical harmonics, r_{ij} is the distance between two ions, and $q = 1, 2$ [92].

$\phi_\sigma(t)$ is effectively a correlation function for an ion, while $\phi_s(t)$ is a correlation function for a pair of ions. The latter weighs more heavily on the contributions from ion pairs at smaller distance of separation r_{ij}, particularly for $\phi_s(t)$ that involves $F_{ij}^{(q)}(t)$ and the $(r_{ij})^{-3}$ factor. Therefore, ion–ion interaction has stronger slowing and stretching effect on $\phi_s(t)$ than on $\phi_\sigma(t)$ and this translates in the context of the CM to a larger n_s in the SLR correlation function in Eq. (3.19) than n_σ in the electrical conductivity correlation function in Eq. (3.18) or the macroscopic conductivity relaxation function in Eq. (3.20), e.g., $n_s > n_M$. The same argument has been used to justify the coupling parameter for center–of-mass diffusion is smaller than that for viscosity in the CM explanation of the breakdown of the Stokes–Einstein relation in Section 2.2.5.6. The independent relaxation of the ion and its primitive relaxation

time $\tau_0 = \tau_{0,\infty} \exp(E_a/kT)$ as well as t_c are the same for both NSR and $\sigma(\omega)$. On applying Eq. (3.1) separately to NSR and $\sigma(\omega)$, we have [282, 291–294, 1571]

$$\tau_s = [(t_c)^{-n_s}\tau_0]^{1/(1-n_s)} = \tau_0[\tau_0/t_c]^{n_s/(1-n_s)}, \tau_\sigma = [(t_c)^{-n_\sigma}\tau_0]^{1/(1-n_\sigma)} = \tau_0[\tau_0/t_c]^{n_\sigma/(1-n_\sigma)}. \tag{3.22}$$

Since $n_s > n_\sigma$ and the fact that in the experimental investigations all relaxation times including τ_0 are much longer than $t_c \approx 1 - 2$ ps, these equations lead us to the result that $\tau_s >> \tau_\sigma$, as observed. In particular, we have the following relations between the activation energies and prefactors:

$$(1-n_s)E_s = (1-n_\sigma)E_\sigma = E_a,\ \tau_{s,\infty} = \tau_\infty(\tau_\infty/t_c)^{n_s/(1-n_s)},\ \tau_{\sigma,\infty} = \tau_\infty(\tau_\infty/t_c)^{n_\sigma/(1-n_\sigma)}. \tag{3.23}$$

The first relation is well obeyed by the experimental data from electrical conductivity relaxation (ECR), in view of the relations between the parameters in $\phi_M(t)$ of ECR and $\phi_\sigma(t)$ given in Eq. (3.21), within experimental errors as demonstrated in Table 3.3. The prefactor τ_∞ of the primitive relaxation time τ_0 is shorter than $t_c \approx 1 - 2$ ps because it is the reciprocal of vibrational frequency. From this and $n_s > n_\sigma$, it can be deduced from the second and the third relations under Eq. (3.23) that $\tau_{s,\infty} << \tau_{\sigma,\infty} << \tau_\infty$, which is in accord with experiments. This can be seen if the Arrhenius T dependences of τ_s and τ_M in Figs. 293 and 294 are extrapolated to infinite temperature. From the ZBLAN data in Fig. 293, $\tau_{s,\infty} = 6.6 \times 10^{-17}$ and $\tau_M, \infty = 4.1 \times 10^{-15}$. The experimental value of the prefactor $\tau_{s,\infty}$ is also in agreement with that calculated from the second CM equations in Eq. (3.23), assuming that the prefactor $\tau_{0,\infty}$ of τ_0 is 2×10^{-13} s [282]. The comparison of the experimental prefactor $\tau_{s,\infty}$ with calculation has to wait later after the microscopic prefactor $\tau_{\sigma,\infty}$ has been deduced from the experimental $\tau_{M,\infty}$ by a relation in the next subsection.

An Analogue of Breakdown of SE and DSE Relations and Decoupling of Dynamic Variables in the Same Glassformer

The decoupling of nuclear SLR from electrical conductivity relaxation is an exact analogy of the breakdown of SE and DSE relations in supercooled liquids. The SLR is the counterpart of viscosity or rotational relaxation, and electrical conductivity relaxation is the counterpart of self-diffusion or probe translational diffusion. It is also the analogue of the observation of different magnitudes and temperature dependence of the structural α-relaxation times for dielectric, mechanical, light-scattering, and enthalpy relaxation in a variety of glassformers by experiments and by molecular dynamics simulations [266–275], discussed before in Section 2.2.1(*v*). The relations $\tau_s >> \tau_\sigma$, $E_s > E_\sigma$, and $n_s > n_\sigma$ have analogues in the breakdown of SE and DSE relations (see Section 2.2.5.6 and Fig. 247). In the present case, the coupling parameters n_s and n_σ are known from experiment to provide a critical test of the prediction of the CM, which turned out to be valid in general for glassy ionic conductors.

Quantitative Relation Between τ_s and τ_σ *Beyond* $(1-n_s)E_s = (1-n_\sigma)E_\sigma = E_a$

As discussed before, electrical conductivity relaxation (ECR) measurements give macroscopic information about ion motion dynamics. The capacitance $C(\omega)$ and conductance $G(\omega)$ measured, as well as the quantities $\varepsilon^*(\omega)$, $\sigma^*(\omega)$, or $M^*(\omega)$ obtained, give no clue to ion concentration, charge, and jump length, and thus clearly it is not microscopic. Notwithstanding, the measured electrical conductivity relaxation (ECR) time τ_M and the microscopic conductivity relaxation time τ_σ have the same activation energy E_σ, emphasized in Eq. (3.21), but their prefactors $\tau_{\sigma,\infty}$ and $\tau_{M,\infty}$ differ. There is a way to calculate τ_σ from τ_M given by a comparison between microscopic and electric conductivity relaxation in [56(b)].

Starting from the velocity–velocity correlation function, an explicit expression for microscopic complex conductivity $\sigma^*(\omega\tau_\sigma)$ is derived via a stochastic transport theory which is given as

$$\sigma^*(\omega\tau_\sigma) = (Nq^2/kT\tau_\sigma)(r_{rms}^2/6)\left\{\frac{1}{\widetilde{\phi}_\sigma(\omega\tau_\sigma)} - i\omega\tau_\sigma\right\}, \tag{3.24}$$

where N is the density of the mobile ions, q the ion charge, k the Boltzmann constant, and T the temperature. The quantity r_{rms}^2 represents the mean-squared displacement of an ion in hopping to nearest neighboring sites, and $\widetilde{\phi}_\sigma(\omega\tau_\sigma)$ is the Laplace–Fourier transform of $\phi_\sigma(t) = \exp[-(t/\tau_\sigma)^{1-n_\sigma}]$. It has also been shown in [56(b)] that the complex conductivity from ECR can be rewritten in the form

$$\sigma_M^*(\omega\tau_M) = (\varepsilon_o/M_\infty\tau_M)\left\{\frac{1}{\widetilde{\phi}_M(\omega\tau_M)} - i\omega\tau_M\right\}, \tag{3.25}$$

which is formally the same as $\sigma^*(\omega\tau_\sigma)$ in the previous equation. From this, τ_σ is related to τ_M by

$$\tau_\sigma/\tau_{EM} = (Nq^2r_{rms}^2)/(6kT\varepsilon_o\varepsilon_\infty). \tag{3.26}$$

This relation enables the microscopic τ_σ to be calculated from the experimental macroscopic τ_M and the quantities N, q, and r_{rms}^2 which can be deduced from the chemical and physical structure of the ionic conductor. This has been carried out for the three glassy and one crystalline ionic conductors [1572], and three of these Li^+ ion conductors $0.56Li_2S–0.44SiS_2$, $0.45Li_2S+0.55GeS_2$, and $Li_{0.5}La_{0.5}TiO_3$(LLTO) are shown in Fig. 295.

After obtaining the microscopic τ_σ, the primitive relaxation time τ_0 can be deduced from the second part of Eq. (3.22) and then the SLR time τ_s can be calculated using this τ_0 by the first part of Eq. (3.22). The three steps outlined can be combined into one equation:

$$\tau_s = [t_c^{(\beta_s-\beta_\sigma)}(\tau_M Nq^2r_{rms}^2/6kT\varepsilon_o\varepsilon_\infty)^{\beta_\sigma}]^{1/\beta_s}, \tag{3.27}$$

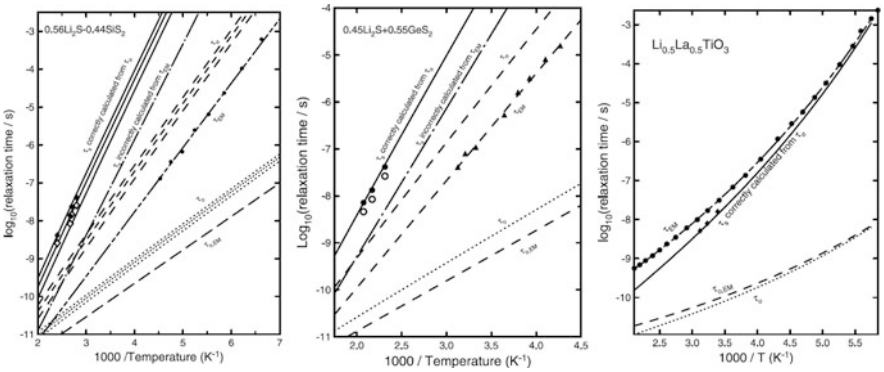

Fig. 295 (*Left*) Arrhenius plot of the correlation time of the mobile ion τ_s deduced from ^{7}Li nuclear spin-lattice relaxation measurement and the macroscopic electrical conductivity relaxation time τ_M (labeled here as τ_{EM}) for $0.56Li_2S–0.44SiS_2$. Experimental data of τ_s (*filled diamonds* and *open diamonds* determined by two different methods) and τ_{EM} (*closed circles*). The three *dashed lines* in descending order are the corresponding microscopic ion hopping relaxation time τ_σ calculated from Eq. (3.26) for $r_{rms} = 3$, 2.5, and 2 Å and other known parameters given in [1572]. The most probable value of r_{rms} is 2.5 Å. The three *dotted lines* in descending order are the corresponding microscopic ion hopping relaxation time τ_0 calculated from τ_σ by solving the second part of Eq. (3.22) for the three cases of $r_{rms} = 3,\ 2.5$, and 2 Å. After obtaining τ_0, the three full lines in descending order are τ_s calculated from the first part of Eq. (3.22) with $r_{rms} = 3,\ 2.5$, and 2 Å, respectively, and other parameters given in [1572]. There is good agreement with the experimental τ_s. Also shown is the primitive relaxation time $\tau_{0,EM}$ (*dashed line at the bottom*) calculated from τ_{EM} by solving an equation similar to Eq. (3.22), with τ_{EM} replacing τ_σ. Note that τ_s calculated from $\tau_{0,EM}$ (*dashed–dotted line*) cannot explain the spin-relaxation time data. (*Middle*) Arrhenius plot of the correlation time of the mobile ion τ_s deduced from ^{7}Li nuclear spin-lattice relaxation measurement and the macroscopic electrical conductivity relaxation time τ_{EM} for $0.45Li_2S+0.55GeS_2$. Experimental data of τ_s (*filled and open circles*) and τ_{EM} (*triangles*). Other lines are the same as in the caption of the *left panel*, except here only results for $r_{rms} = 2.5$ Å are shown. (*Right*) Same as in the caption of Fig. 1 for $Li_{0.5}La_{0.5}TiO_3$ (LLTO), a crystalline ionic conductor. The value of $r_{rms} = 3.87$ Å is known. Experimental data of τ_s (*filled diamonds*) and τ_{EM} (*filled circles*). Reproduced from [1572] by permission

where $\beta_s \equiv (1 - n_s)$ and $\beta_\sigma \equiv (1 - n_\sigma)$. This relation now enables the CM to quantitatively account for the difference between the experimental values of τ_s and τ_M. Figure 295 demonstrates excellent agreement with the data. A corollary of Eq. (3.27) is the relation between E_s and E_σ:

$$E_s/E_\sigma = (1 - n_\sigma)/(1 - n_s), \tag{3.28}$$

a prediction that has previously been verified (see Table 3.3).

Isotope Mass Dependence of σ

Before leaving the subject of dynamics of ions in ionic conductors, we mention an interesting experimental finding of anomalous isotope mass dependence of conductivity by Jain and Peterson in 1982 [1573] that has been shown to provide strong

support of the application of the CM to ion dynamics from the very start in 1984 [362].

The experimental study is on the isotope mass dependence of the ion conductivity. Replacing the more abundant isotope ^{7}Li by ^{6}Li in the Li_2O:2.88B_2O_3 glasses is one way to change the prefactor, because the attempt frequency depends on the mass m of the vibrating ion. Given the rest are the same except changing the Li isotope mass, the change of the prefactor is directly reflected in the corresponding change of the dc conductivity. The dc conductivity can be measured to high accuracy and the ratio $^6\sigma/^7\sigma$ of the conductivities was found to be much larger than $\sqrt{7/6}$ from the classical dependence of the attempt frequency on the reciprocal square root dependence of the mass m or other similar values from more sophisticated theories [1573]. The data of $^6\sigma/^7\sigma$ are shown in the right panel of Fig. 296.

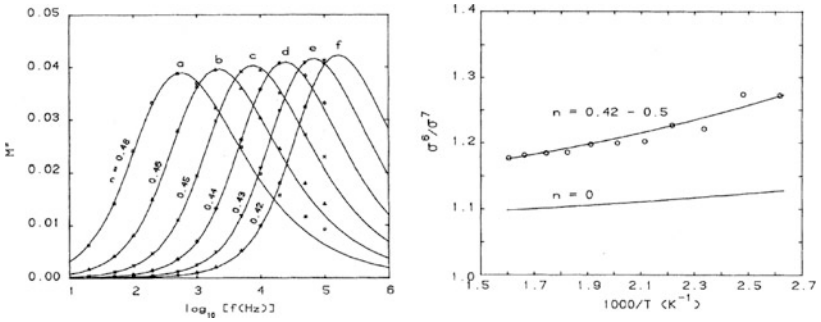

Fig. 296 (*Left*) Loss electric modulus $M''(f)$ vs. frequency for the Li_2O–3B_2O_3 glass containing predominantly ^{6}Li isotope. *Solid curves* are Kohlrausch fits with n values indicated at temperatures (in °C): (**a**) 108.9; (**b**) 131.0; (**c**) 153.8; (**d**) 177.5; (**e**) 200.5; (**f**) 222.2. (*Right*) The ratio $^6\sigma$ / $^7\sigma$ of the conductivities of ^{6}Li and ^{7}Li isotopes. Experimental data indicated by *circles*. *Upper curve* is theoretical fit based on the CM equation using n values in the *left panel*. *Lower curve* is the normal isotope mass dependence, i.e., when n is put to zero. Reproduced from [362] by permission

The observed anomalous isotope mass m dependence of dc conductivity has been explained quantitatively from the CM relation

$$\tau^*_\infty(m) = [t_c^{-n}\tau_\infty(m)]^{1/(1-n)} \tag{3.29}$$

between the prefactor $\tau^*_\infty(m)$ of the observed conductivity relaxation time τ_σ and the primitive prefactor $\tau_\infty(m)$ using the actual value of n obtained by fitting the frequency dispersion of the data in an electric modulus representation by Fourier transform of the Kohlrausch function. The values of the coupling parameter n are obtained from the fits to the loss electric modulus data shown in the left panel of Fig. 296. The calculated $^6\sigma/^7\sigma$ are in good agreement with the experimental data.

So far, no other theory except the CM has successfully explained this isotope mass dependence.

3.2.5.2 Entangled Polymer Chains: Self-Diffusion vs. Viscosity

There are direct experimental data of self-diffusion and viscosity of entangled polymers showing that they have different activation energies and molecular weight dependences. This property is a close analogue of the breakdown of Stokes–Einstein relation found for small molecular glassformers and the difference between SLR and conductivity of mobile ions in glassy and crystalline ionic conductors. However, note that this anomaly is observed from the motion of polymer chains that has nothing to do with glass transition, nor with ions in glasses or crystals. The discussion of the dynamics of entangled polymer melts below in parallel with other different systems serves to illustrate several other general properties of relaxing/diffusing interacting systems.

Activation Enthalpy and Molecular Weight Dependences of Viscosity of Entangled Polymers

Some high molecular weight entangled polymers such as polyethylene (PE), hydrogenated polybutadiene (HPB), and poly(dimethylsiloxane) (PDMS) have low glass temperatures and the terminal relaxation can be measured at temperatures high above T_g of the polymers. At the high temperatures the terminal relaxation time as well as the viscosity exhibited Arrhenius behavior. The activation energies E_η, determined from the zero-shear viscosity or terminal zone shift factors, were often found to be larger than the conformational transition barrier energy E_a, which should govern the temperature dependence of the mobility of the polymer chains high above T_g had they been able to relax independently of each other. Examples of PE and HPB in Table 3.4 show E_η for shear viscosity of entangled linear chains, which is larger than the known conformation energy barrier of about 3.5 kcal/mol for PE and 4.2 kcal/mol for HPB [359, 360, 833–836, 1575]. The difference between the activation energies of shear viscosity η and self-diffusion coefficient D will be the subject of discussion in a later section.

Linear Entangled Polymers

Earlier attempt [360] and more sophisticated approach by taking into account of constraint mitigation later [837] have applied the CM to the terminal relaxation of entangled linear polymers. The coupling parameter can be obtained from fits to the dielectric spectrum [837] or the mechanical spectrum [360] of monodisperse polymers. The value of n_η obtained falls within the range of $0.40 \leq n_\eta \leq 0.43$. An alternative method to determine n_η is from the experimentally observed ratio J_S/J_N, which is a measure of the terminal dispersion [29]. Here J_N is the plateau compliance and J_S is the steady-state compliance [165, 171, 248]. If the Kohlrausch function is used to fit the terminal dispersion, then

$$\frac{J_S}{J_N} = \beta \left[\Gamma\left(\frac{2}{\beta}\right) \Big/ \Gamma\left(\frac{1}{\beta}\right) \right]^2, \tag{3.30}$$

Table 3.4 Parallel explanation of the molecular weight and temperature dependences of zero shear viscosity of polyethylene (PE), hydrogenated polybutadiene (HPB), and polydimethylsiloxane (PDMS). The actual conformational energy barrier of PE is taken from measurement on alkanes [360] and that of HPD is not known, but it is expected to be similar to PE. For references to the sources of data on PE and HPB, see Table 2 in [1577]. For PDMS, the experimental activation energy for viscosity E_η is 3.56 kcal/mol [1578] compared with E_a=2 kcal/mol from neutron scattering experiment [1579, 1580]

Linear polymer	Measured shear viscosity activation enthalpy, E_η (kcal/mol)	Observed M dependence of shear viscosity	Coupling parameter for shear viscosity (n_η)	Predicted M dependence of shear viscosity, from $\tau_0 \propto M^{2.0}$	Predicted conformational energy barrier, E_a (kcal/mol)	Actual conformational energy barrier (kcal/mol)
PE	6.35	$M^{3.5}$	0.43	$M^{3.5}$	3.6	3.5
HPD	7.2	$M^{3.4}$	0.41	$M^{3.4}$	4.2	
PDMS	3.56	$M^{3.5}$	0.43	$M^{3.5}$	2.03	2.0

where Γ is the gamma function and $\beta = (1 - n_\eta)$. The right-hand side of Eq. (3.30) is a monotonic increasing function of n_η that reaches the value of 2 when $n_\eta = 0.40$ [360, 904]. Experimental value of J_S/J_N of monodisperse polymer melts is about 2 or slightly larger [165, 171, 248], and thus it substantiates that n_η falls within the range of $0.40 \leq n_\eta \leq 0.43$.

Incidentally, the coupling parameter n_η does not depend on the length of the chain as long as the molecular weight exceeds the molecular weight M_e for entanglement because the situation is self-similar. The terminal relaxation time τ_η and η are related by the Maxwell equation $\eta = G_N \tau_\eta$, where G_N is the plateau modulus. The values of n_η in the range of $0.40 \leq n_\eta \leq 0.43$ can immediately explain the $M^{3.4}$ or the $M^{3.5}$ dependence of η and τ_η [905] based on Eq. (3.4) and the well-known $M^{2.0}$ dependence of the primitive relaxation time τ_0 of uncoupled motion of a single chain from the Rouse model modified for undiluted polymers [29]. The observed anomalous dependence of τ_η on M and T

$$\tau_\eta (M, T) \propto M^{3.4} \exp\left(E_\eta / RT\right) \tag{3.31}$$

have been explained simultaneously by the generalization of Eq. (3.4)

$$\tau_\eta (M, T) \propto [\tau_0 (M, T)]^{1/(1-n_\eta)} = M^{2/(1-n_\eta)} \exp\left(E_a / (1 - n_\eta) RT\right), \tag{3.32}$$

with a *single* value of n_η. The results can be seen from Table 3.4 for PE and HPD. The companion relation for activation enthalpies is $E_a = (1 - n_\eta) E_\eta$. The enhanced molecular weight dependence of τ_η and η is analogous to the enhanced isotope mass dependence of Li^+ ion conductivity in Li borate glasses [362, 1573], discussed before in this section.

For PE, from the experimental value of $E_\eta = 6.35$ kcal/mol [833], $E_a = (1 - n_\eta)E_\eta$ yields 3.6 kcal/mol for the primitive activation energy. This is in agreement with the value of 3.5 kcal/mol (14.8 kJ/mol) for the conformational energy barrier of bulk PE from molecular dynamics simulations by Boyd and coworkers [1581] and also consistent with the estimation of the potential energy for rotating the carbon–carbon bonds in alkanes in the range from 3.1 to 3.7 kcal/mol by Flory [1575]. There is additional support from ^{13}C-NMR measurements of local segmental relaxation in two unentangled low molecular weight polyethylene $C_{44}H_{90}$ and one with $M_w = 2150$ g/mol in the nanoseconds range by Qiu and Ediger [1582]. At this short time range, many-body dynamics is not that important. This is supported by the ^{13}C-NMR experimental correlation function well described by an exponential correlation function $\exp(-t/\tau_\alpha)$, and τ_α has an Arrhenius temperature dependence with activation enthalpy equal to 16.7 kJ/mol (or 4 kcal/mol), which is close to the primitive activation energy E_a deduced from $E_\eta = 6.35$ kcal/mol by the product $(1 - n_\eta)E_\eta$, which evaluates to 3.6 kcal/mol (or 15.1 kJ/mol).

For PDMS with $n_\eta = 0.43$, Eq. 3.32) yields a molecular weight dependence of $M^{3.5}$ and $E_\eta = 3.5$ kcal/mol based on $E_a = 2$ kcal/mol from neutron scattering data of Allen and coworkers [1579, 1580], which is in good agreement with the experimental value of $E_\eta = 3.56$ kcal/mol (14.9 kJ/mol) from rheological measurements of entangled PDMS with $M_w = 10^5$ g/mol ($M_e = 12,000$ g/mol) [1578, 1583]. Conversely from the experimental value of $E_\eta = 3.56$ kcal/mol, $E_a = (1 - n_\eta)E_\eta$ yields 2.03 kcal/mol, the primitive activation energy from neutron scattering (Table 3.4). Nevertheless, viscosity measurement on PDMS with very low molecular weight of 1250 and 550 g/mol by Ding et al. [1584] reported $E_\eta = 14.8$ and 13.5 kJ/mol, almost the same E_η of entangled PDMS. These values of E_η are larger than $E_a = 2$ kcal/mol (8.4 kJ/mol) of local segmental relaxation of high molecular weight PDMS from neutron scattering. The E_η of low M_w PDMS from Ding et al. may be that of the sub-Rouse modes, which is cooperative in nature [872].

The viscosity η of entangled linear atactic polypropylene (aPP) does not have Arrhenius temperature dependence [361, 902]. Effort has been made to measure η at very high temperatures [361] where the local segmental relaxation time is of the order of picoseconds [875]. Because t_c is about 2 ps for polymers, the local segmental relaxation is essentially in the primitive relaxation mode, and we can expect its relaxation rate at these high temperatures governed by the conformational transition barrier energy of aPP, which is about 4 kcal/mol [1585]. The mobility of the terminal relaxation of the chains and the viscosity should have the same activation energy at the same temperatures. However, from the measurement of viscosity, the apparent activation energy of the viscosity E_η of entangled aPP is estimated to be 7.2 kcal/mol at the very high temperatures [361]. This larger activation energy can be explained again by Eq. (3.32), which predicts $E_\eta = 7.0$ kcal/mol from $n_\eta = 0.43$ and $E_a = 4$ kcal/mol. By the way, the reptation theory [41–44] cannot predict E_η as done by the CM.

The above shows that the CM equation(3.32) can explain both the molecular weight and temperature dependence of the viscosity of entangled polymers. Rendell et al. [1577] have shown that the same CM can explain additionally the

concentration dependence of the terminal relaxation and viscosity of entangled polymer solutions. Explicitly, if ϕ is the polymer volume fraction, the predicted combined M and ϕ dependences of viscosity is $\eta \propto M^{3.4}\phi^{3.4}$, in agreement with experiment [905].

Branched Entangled Polymers

Changing the architecture of polymers from linear chains by branching to multiple-arm star will enhance the molecular constraints overall and hence the effective coupling parameter if the arms of the star are sufficiently long for them to fully entangle. Larger coupling parameter n_η for such a star than the linear value results in stronger molecular weight dependence and higher activation energy of the viscosity as predicted by Eq. (3.32). The relaxation times of the Rouse–Ham modes for a star-branched polymer molecule still have the M^2 dependence like the Rouse modes for a linear molecule [29], and Eq. (3.32) still holds. The same conformation energy barrier is deduced [359, 1577]. Such predictions are borne out by data of star-branched PE and HPB as shown in Table 3.5.

Table 3.5 Shear viscosity data of star-branched PE

Star-branched polymer	Measured shear viscosity activation enthalpy, E_η (kcal/mol)	Observed M dependence of shear viscosity	Coupling parameter for shear viscosity n_η	Predicted M dependence of shear viscosity	Predicted conformational energy barrier, E_a (kcal/mol)	Actual conformational energy barrier (kcal/mol)
PE	11.66	$M^{6.56}$	0.70	$M^{6.67}$	3.5	3.5
HPD	14.29		0.71	$M^{6.9}$	4.15	n.a.

From [833]. The data of HPB stars are taken from the Ph.D. thesis of V. R. Raju [1586]. For more details, see [359, 1577]

Again, a larger coupling parameter can explain simultaneously the molecular weight dependence and the activation energy for the stars. The larger values of the coupling parameter are also consistent with the observed broader dispersions of the terminal relaxation of the monodisperse stars [1577, 1586].

Different Activation Energies and M Dependence of Self-Diffusion than Viscosity in Some Entangled Polymers

Self-diffusion of entangled polymer chains was measured for PE and HPB [1587]. For the self-diffusion coefficient of HPB, only data cited here and in [1577] are considered and not all the data combined like the way discussed by Lodge in [1588]. From experiments, the self-diffusion coefficient D of these two polymers has the M^{-2} dependence and Arrhenius T dependence with activation enthalpy E_D listed

Table 3.6 Parallel explanation of the molecular weight and temperature dependences of self-diffusion of polyethylene (PE) and hydrogenated polybutadiene (HPB). The actual conformational energy barrier of PE is taken from measurement on alkanes [360]. HPD is not known, but it is expected to be similar to PE. For references to the sources of data, see Table 2 in [1577]

Linear polymer	Measured self-diffusion activation enthalpy, E_D (kcal/mol)	Observed M dependence of self-diffusion coefficient	Coupling parameter for self-diffusion, n_D	Predicted M-dependence of self-diffusion from $\tau_0 \propto M^{2.0}$	Predicted conformational energy barrier, E_a (kcal/mol)	Actual conformational energy barrier (kcal/mol)
PE	5.47	M^{-2}	1/3	M^{-2}	3.7	3.5
HPB	7.2	M^{-2}	1/3	M^{-2}	4.1	n.a.

in Table 3.6. Theoretically, D is the ratio $(R_g)^2/\tau_D$, where $R_g(\sim M)$ is the radius of gyration of the linear chain and τ_D is the center-of-mass diffusion time of the entangled chain. The latter is related to the primitive diffusion time τ_{0D} by the CM equation

$$\tau_D(M,T) = [t_c^{-n_D}\tau_{0D}(M,T)]^{1/(1-n_D)}. \tag{3.33}$$

Since τ_{0D} is the uncoupled center-of-mass diffusion of a single chain, it can be identified with that of the Rouse model, which has the $M^{2.0}$ dependence. With the $M^{2.0}$ dependence of τ_{0D}, Eq. (3.33) yields the $M^{3.0}$ dependence of τ_D if $n_D = 1/3$. From the $M^{3.0}$ dependence of τ_D and $(R_g)^2 \propto M$, it follows from $D = (R_g)^2/\tau_D$ that $D \propto M^{-2.0}$ as found by experiment. Support of $n_D = 1/3$ comes from the fact that the product $(1 - n_D)E_D$ is almost the same as $(1 - n_\eta)E_\eta$, and also E_a, the conformational energy barrier of these two polymers. These correspondences can be seen in Table 3.6.

Confirmation by the Neutron Spin Echo Experiment of Zamponi et al.

Here we recall the center-of-mass mean-square displacement (MSD) data from neutron spin echo experiment of Zamponi et al. [1503] shown in Fig. 281. For the entangled polyethylene chains with $N = 192$ and 377, the subdiffusion term t^{1-n} has exponent $(1–n)$ values of 0.72 and 0.63, respectively. The molecular weights of the polymers with $N = 192$ and 377 are about $1.5M_c$ and $3M_c$, respectively, where M_c is the molecular weight for entanglement. Substituting these values of $(1–n)$ for $(1–n_D)$ in Eq. (3.33), one gets the molecular weight dependences

$$D \propto M^{-1.8}, \text{ for } N = 192, \text{ and } D \propto M^{-2.2}, \text{ for } N = 377 \tag{3.34}$$

which are consistent with the neutron spin echo data within the uncertainty of determining the exponent of the subdiffusion.

Analogue of the breakdown of SE relation in supercooled liquids, and decoupling of SLR and conductivity relaxation in glassy and crystalline ionic conductors

The results above from comparison of self-diffusion and viscosity of entangled polymer chains, namely $n_D < n_\eta$ and $E_D < E_\eta$, have almost exact analogues in the breakdown of Stokes–Einstein relation of molecular glassformers [438, 449–457] and ionic liquids [158], and the CM explanations given here for entangled polymers follow the same parent CM equation as those given for the analogues [159, 268] discussed in Sections 2.2.5.7. Furthermore, the result

$$(1 - n_D)E_D \approx (1 - n_\eta)E_\eta = E_a \tag{3.35}$$

for entangled polymers is the analogue of Eq. (3.23), $(1-n_s)E_s \approx (1-n_\sigma)E_\sigma = E_a$, between nuclear spin relaxation and conductivity relaxation in the case of ionic conductors (see also Table 3.3). Both cases show that the activation energy of the primitive relaxation E_a can be recovered from that of the slow many-body relaxation by multiplying it by the fractional Kohlrausch exponent, and the result is the same independent of the dynamic variable chosen.

3.2.5.3 Semidilute Polymer Solutions

Polymer dynamics in semidilute and concentrated solutions has been a subject of considerable interest in the past decades. Some works in this area have been referenced before [776–779, 1555–1567] in connection with some universal properties of relaxation and diffusion in interaction systems discussed before. Compared to polymer melts, introduction of the polymer concentration c as an additional variable has made the problems in polymer solutions richer. Examples of other studies on various properties of semidilute polymer solutions related to c dependence are given in [834, 1590–1606] and reviews in [1607, 1608]. There are various problems of polymer diffusion in semidilute solutions of high molecular weight polymers as well as in concentrated solutions. In the concentrated solutions, the problem is the observed $M^{2.5}$ dependence of the polymer diffusion coefficient D, where M is the molecular weight [1609, 1610]. In semidilute solutions, there are a number of observed properties that need to be explained. Here we take the observed properties from two systems.

Probe Diffusion vs. Viscosity in Semidilute Polymer Solutions

The first one is the hydroxypropylcellulose (HPC):water semidilute aqueous solutions. The dynamics of several length scale of this semidilute polymer solution was studied by measurement of optical probe diffusion in it by light scattering. The optical probes carboxylate modified polystyrene sphere in water solutions of nominal 300 kDa (M_W=415 kDa) HPC at 25°C. The size of probes employed R_{probe} are 760,

189, 102, and 20 nm [1566, 1611, 198]. The optical probe diffusion D and shear viscosity η experimental data of hydroxypropylcellulose/water solutions obtained by Phillies and coworkers are summarized briefly as follows. All these were obtained from the field correlation function $g^{(1)}(t)$ from light scattering of optical probes suspended in solution. The parameters characterizing the quantities above depend on the probe size and the polymer molecular weight.

(a) The field correlation function has the stretched exponential time dependence

$$g^{(1)}(t) = A_o \exp[-(t/\tau_{\rm D})^{1-n_{\rm D}}]. \tag{3.36}$$

(b) The concentration dependence of D is given by the stretched exponential form

$$D = D_o \exp(-\alpha_{\rm D} c^{u_{\rm D}}). \tag{3.37}$$

(c) The $\tau_{\rm D}$ has the anomalous dependence on the scattering vector q given by

$$\tau_{\rm D} \propto q^{-2/(1-n_{\rm D})}. \tag{3.38}$$

(d) The solution viscosity η is found to be described well by another stretched exponential c dependence

$$\eta = \eta_o \exp(\alpha_\eta c^{u_\eta}), \quad \text{with} \quad \alpha_\eta \propto M^{\gamma_\eta} \tag{3.39}$$

valid up to very large M and c. The parameters α_η, u_η, and γ_η for viscosity in general have values different from the corresponding $\alpha_{\rm D}$, $u_{\rm D}$, and $\gamma_{\rm D}$ for probe diffusion [198, 777, 1606]. Probes in 300-kDa hydroxypropylcellulose show Stokes–Einstein behavior, $D = kT/6\pi\eta R_{\rm probe}$, for large ($R_{\rm probe} > 55$ nm) spheres but increasingly non-Stokes–Einstein behavior for small probes ranging from 33 down to 0.5 nm in radius.

Some of these observed dynamic properties of semidilute polymer solution at different length scales determined by the probe diameter are obviously analogues of glassformers. These include the Kohlrausch stretched exponential correlation function in Eq. (3.28) and the superlinear q dependence of $\tau_{\rm D}$ in Eq. (3.37). Here is another example of the breakdown of Stokes–Einstein relation $D = kT/6\pi\eta R_{\rm probe}$, which has nothing to do with glass transition. In optical probe experiments, motions of chain segments with length scales comparable to $R_{\rm probe}$ determine the probe diffusion coefficient D. On the other hand, η is determined by the motions of entire polymer chains, which experience stronger dynamic constraints and larger coupling parameter than do chain segments having length scale of $R_{\rm probe}$ if $R_{\rm probe}$ is much smaller than $R_{\rm g}$ of the polymer. Thus, we expect $n_\eta(c) > n_D(c)$ to hold when the probe size is small. If $n_\eta(c) > n_{\rm D}(c)$, it follows immediately from the CM-derived expressions [198] that η will have a stronger c dependence than D. The reader may see that the CM explanation given here for the breakdown of SE relation of probe

diffusion in semidilute solution of entangled polymer chains is isomorphic to that given for the same phenomenon in glass-forming liquids.

A theoretical treatment of the dynamics of semidilute polymer solutions has been proposed by using the CM of polymer chain dynamics together with scaling arguments. The theory has many predictions, which are remarkably consistent with all known experimental facts of HPC/water system. The formalism involves some cumbersome equations and will not be reproduced here. The interested reader can consult [198, 779]. The upshot of scaling is to allow extraction of values for the coupling parameter n_D by three separate paths from the concentration, time, and scattering vector dependencies of $g^{(1)}(t)$. Values of n_D from these three distinct physical approaches are shown to be mutually consistent, especially in the higher concentration, large-probe-particle regime in which the scaling arguments are most likely to be valid. In other words, as a function of c and M, the same n_D explains simultaneously the concentration and molecular weight dependences of D and τ_D, time dependence of $g^{(1)}(t)$, and scattering vector dependences of τ_D. By the way, it is well known that reptation model cannot give satisfactory explanation of the dynamics of semidilute polymer solutions, not even the dependence of D on c and M.

Linear and Star-Branched Polystyrene Tracer Diffusion in Semidilute Polymer Solutions

A large body of tracer diffusion coefficient measurements of linear and star-branched polymers in dilute, semidilute and concentrated solutions have accumulated since 1986 [1594–1598]. Naturally, attempts [1595, 1596] have been made in the past to examine these data in the light of the reptation model. Unfortunately, it was found that these data could not be described by the reptation mechanism even with constraint release being included [1594–1598, 1607]. In 1989, an explanation based on combining concentration scaling theory [834, 1590, 1612] and the coupling model was proposed and part of the results was published in an abbreviated format by Ngai and Lodge [1613]. Since then, publication of the entire analysis of the experimental data was put on hold, partly because at that time there is no *direct* evidence to support the application of the coupling model to diffusion in semidilute solutions. However, in the intervening years from 1989 till 1996, new experimental investigations [776–778, 780, 1557, 1566, 1602, 1603, 1614, 1615] have provided the most direct evidence of the applicability of the coupling model. These include the crossover from primitive linear exponential relaxation $\exp(-t/\tau_0)$ to Kohlrausch stretched exponential relaxation $\exp\left[-(t/\tau)^{1-n}\right]$ and the $Q^{-2/(1-n)}$ dependence of τ, discussed before in Sections 3.2.3 and 3.2.4. Encouraged by these developments uniquely in favor of the CM, the scaling–coupling theory of dynamics of semidilute polymer solutions was given in full in 1996 by Ngai and Phillies [198] and applied to probe diffusion data of Phillies and coworkers addressed in the previous subsection. In the same year, the scaling–coupling theory was applied [779] to the analysis of the linear, 3-arm star and 12-arm star polystyrene tracer diffusion in solutions of

linear poly(vinyl methyl ether) of various molecular weights and concentrations by dynamic light-scattering measurements by Lodge and coworkers [1595–1598] and forced Rayleigh scattering measurement of linear polystyrene tracer in polystyrene matrix by Yu and coworkers [1594]. The scaling–coupling theory [779] explained the empirical stretched exponential form $D = D_o \exp(-\alpha c^u)$ for the concentration dependence of the diffusion coefficient originates from the monotonic increase of the coupling parameter n with c/c^*. Conversely, the measured stretched exponential concentration dependence of D has been used to calculate n as a function of c, tracer molecular weight M, and matrix molecular weight P. At constant c and fixed P, these n values, $n(M)|_{c,P}$, have been used to calculate the tracer molecular weight dependence of the diffusion coefficient $D(M)|_{c,P}$ at constant c and fixed P. The calculated values of $D(M)|_{c,P}$ are in good agreement with measurements. In particular, tracer molecular weight dependence of $D \propto M^a$, with a larger than 2 and as large as approximately 3, observed in matrix solutions at higher concentrations can be explained. Full dynamic constraints are imposed on the tracer by the matrix solution if $P >> M$. However, when the latter condition is not satisfied, some of the dynamic constraints are mitigated in the same matrix solution, leading to a decrease of the coupling parameter. The effects of mitigation of dynamic constraints under the condition of $M>P$ on the diffusion of linear and branched PS in PVME solutions are demonstrated by using directly the experimental data or alternatively by the decrease of the calculated values of n. Thus, the dependences of D on the three variables c, M, and P can be explained from the corresponding dependences of the coupling parameter n through the physics contained in the coupling model with the assist of scaling. The temperature dependence of $D(c, M, P)$ has also been predicted to depend sensitively on $n(c/c^*,\ M,\ P)$. This prediction should be a critical test of the coupling model, but till now there is little data of temperature dependence of tracer diffusion to compare with. Details of the analysis by the model and comparison of predictions with experiments can be found in [779].

3.2.6 Recovering or Discovering the Primitive Relaxation

In Chapter 2 where we addressed principally glass-forming substances, the universal secondary relaxation of the Johari–Goldstein (JG) kind found by various spectroscopies is a manifestation of the primitive relaxation in view of their similar character and behavior, and the good correspondence between the JG relaxation time τ_{JG} from experiment and the calculated τ_0. Analogues of the JG relaxation in glassformers actually are already found in the other interacting systems discussed in Sections 3.2.3 and 3.2.4. Dynamic light-scattering experiments have shown the presence of the primitive relaxation at short times with $\exp(-t/\tau_f)$ decay and τ_f has the normal q^{-2} dependence. The experimental correlation function is usually well fitted by Eq. (3.6) in the form of the sum $f(q,t) = A\exp(-t/\tau_f) + (1-A)\exp[-(t/\tau_s)^{1-n}]$. To make obvious the equivalence to JG β-relaxation as often found in dielectric loss spectra, $f(q,t)$ is Fourier transformed to obtain the susceptibility $\chi''(\omega)$ in Fig. 297.

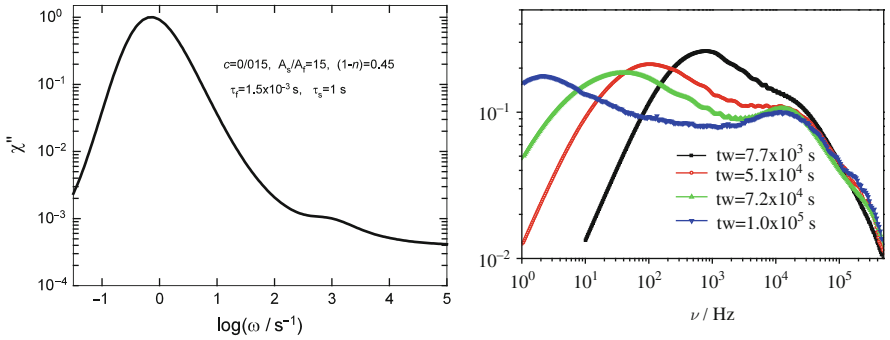

Fig. 297 (*Left*) Susceptibility obtained by Fourier transform of $f(q,t) = A\exp(-t/\tau_f) + (1 - A)\exp\left[-(t/\tau_s)^{1-n}\right]$ from fit to dynamic light-scattering data of an aqueous solution of a hydrophobically end-capped poly(oxyethylene) urethane (HPOEU) at concentration $c = 0.015$ g/ml by Nyström et al. [778]. The parameters A, τ_f, τ_s, and $(1–n)$ are shown in the figure. (*Right*) Susceptibility data obtained by numerical Fourier transform of PCS correlation function of the Laponite colloidal suspension at different aging times t_w performed by S. Capaccioli (Laponite concentration $C_w = 2.5\%$, salt concentration $C_s = 2 \times 10^{-3}$ M). Data are from Fig. 2-D of [342] and provided digitally by L. Zulian

The parameters A, τ_f, τ_s, and $(1–n)$ are taken from dynamic light-scattering study of an aqueous solution of a hydrophobically end-capped poly(oxyethylene) urethane (HPOEU) at concentration $c = 0.015$ g/ml by Nyström et al. [778]. The bump at higher frequencies is the analogue of resolved JG β-relaxation of glassformers.

The time-domain photon correlation spectroscopy data of colloidal suspension of Laponite [340–342] discussed before have also been fitted by $f(q,t) = A\exp(-t/\tau_f) + (1 - A)\exp\left[-(t/\tau_s)^{1-n}\right]$. Shown in the right panel of Fig. 297 is the susceptibility $\chi''(\omega)$ obtained by Fourier transform of the data at four different aging times t_w. The JG β-relaxation appearing at higher frequencies is like that commonly found in other glassformers by dielectric spectroscopy.

We have seen in the many examples given before that the relaxation time τ of many-body interacting systems is anomalous in magnitude as well as dependences on variables. In the context of the coupling model (CM), these anomalies originate from the modification of the normal primitive relaxation time τ_0 according to Eqs. (3.1) and (3.2), principally by raising τ_0 to the superlinear power $1/(1 - n)$. Larger n leads to greater modification of τ_0 and higher degrees of the anomaly. All these are consistent with many-body effects as the cause of the anomalies because n is a measure of the amount of stretching in the Kohlrausch correlation function, which is an obvious indicator of many-body effects. By examples, it has been shown how the CM explains many anomalies in different systems. Now we turn this around and use the experimentally observed anomalies to support verity of the CM. This is done by calculating τ_0 from the experimental τ and n according to Eqs. (3.1) and (3.2), and verifying that the calculated τ_0 is in agreement with either the expected value or the actual value obtained by another source. Actually, this way of recovering τ_0 has been demonstrated before at several places in this chapter. The recovered prefactor

τ_∞ of τ_0 from conductivity relaxation or dynamic light scattering in YSZ has been shown to agree well with the attempt frequency of the oxygen ion independently determined by hyper Raman spectroscopy (see Fig. 286). The recovered activation energy E_a of τ_0 of Ag ions in AgI–$AgPO_3$ or Ag_2S–GeS_2 is in agreement with that directly determined by neutron scattering (see Table 3.2). The recovered activation energy E_a of τ_0 of PE and PDMS chains is consistent with the conformation energy barriers independently determined (see Tables 3.4 and 3.5). In this section, we add more examples from diverse interacting systems to reaffirm the physical reality of the primitive relaxation and in turn the validity of the CM.

3.2.6.1 Influence of Mesophase Structures on the β-Relaxation in Side-Chain Liquid Crystal Polymers (SCLCPs)

This particular problem gives us another occasion to consider the anomalously large activation energy accompanied by unphysically high attempt frequency in many-body relaxations with Arrhenius *T*-dependent relaxation times. Such dual anomalies have been encountered before in ionic conductors in this chapter and are referred to in the literature as the "compensation law" or the "Meyer–Neldel" rule. The system is a side-chain liquid crystal polymer (SCLCP) and the chemical structure of its repeat unit of the 10 samples studied by Schönhals and coworkers [1616–1618] are shown schematically below.

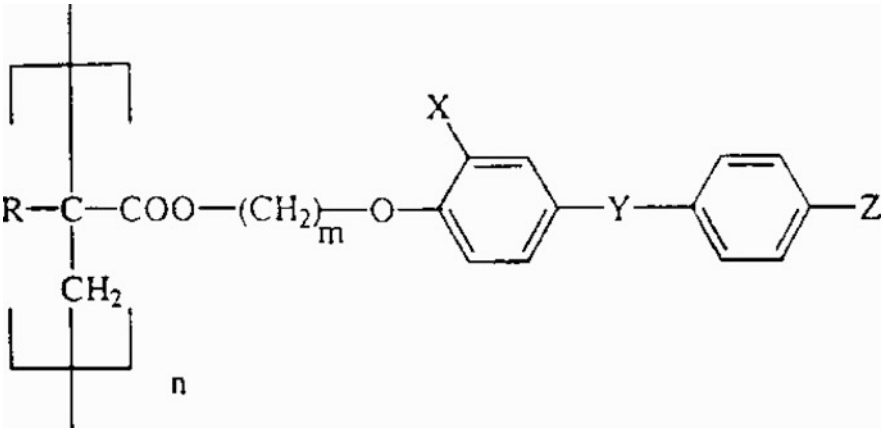

The backbone or the main chain is either poly(methacrylate) or poly(acrylate), and the side chain consists of mesogenic groups separated from the main chain by a spacer consisting of a chain of $–CH_2–$ units. The mesogenic groups are derivatives of (*p*-alkoxy-phenyl)-benzoate that have optical activity [1616–1618]. The process studied by Schönhals and coworkers is the rotational fluctuations of the mesogenic group about its long axis called the β-relaxation. Although called such, this β-relaxation is cooperative because of its size, like the γ-relaxation in BPA-polycarbonate [883–890].

Table 3.7 Experimental data of the most probable $f^*_{\beta\infty}$ and E^*_β, appearing in the Arrhenius equation $f^*_{\max,\beta}(T) = f^*_{\beta\infty}\exp(-E^*_\beta/kT)$ for 10 polymers with various mesophase structures from dielectric relaxation measurements. The most probable coupling parameter n and the primitive pre-exponential factor $f_{\beta\infty}$ have been obtained from the predictions of the coupling model

Polymer	Mesophase	$\log(f^*_{\beta\infty}/Hz)$	E^*_β (kJ/mol)	$\log(f_{\beta\infty}/Hz)$	n
P1	Isotropic	12.8	45.7	11.44	0.716
P2	Nematic	13.8	46.5	11.71	0.720
P3	Nematic	14.8	53.3	11.85	0.756
P4	Smectic A	16.5	57.5	12.17	0.774
P5	Smectic A	16.4	56.4	12.17	0.77
P6	Smectic A	17.1	61.0	12.22	0.787
P7	Smectic B	17.5	62.8	12.27	0.793
P8	Smectic B	18.2	63.2	12.40	0.794
P9	Smectic B	18.5	64.9	12.42	0.80
P10	Smectic B	19.4	68.9	12.51	0.81

Different mesophases were obtained by a variation of the number of methylene units in the spacer and in the tail groups Z. The mesophases of 10 SCLCPs are shown in Table 3.7. It was found by dielectric spectroscopy that the most probable relaxation frequency $f^*_{\max,\beta}$ of the β-relaxation has the Arrhenius temperature dependence

$$f^*_{\max,\beta}(T) = f^*_{\beta\infty}\exp\left(-E^*_\beta\Big/kT\right), \tag{3.40}$$

but the pre-exponential factor $f^*_{\beta\infty}$ as well as the activation energy E^*_β increases (obeying a compensation law) significantly with the order of the mesophase. In the isotropic state, $f^*_{\beta\infty} = 10^{12.8}$ Hz and $E^*_\beta = 45.7$ kJ/mol. In going from the isotropic state to the nematic, the smectic A, and the smectic B mesophases (i.e., with increasing order of the mesophase and decreasing mean lateral mesogenic distance as obtained by X-ray measurement), both $f^*_{\beta\infty}$ and E^*_β increase to reach the anomalously high values of $f^*_{\beta\infty} = 10^{19.4}$ Hz and $E^*_\beta = 68.9$ kJ/mol. These results are collected in Table 3.7.

The interesting experimental facts found by varying the mesophase are the following: (1) the simultaneous increases of $\log f^*_{\beta\infty}$ and E^*_β with decreasing mean lateral mesogenic distance that obey the compensation law and (2) the unphysically large pre-exponential factors found in the smectic mesophases. These are analogues of the same properties found in other interacting systems including the crystalline and glassy ionic conductors. The CM has been applied to explain them [1619]. Concentration fluctuations occur in the environments of the mesogenic group because of the internal blending of the mesogenic groups with the long methylene spacer chains, which broadens the β-relaxation dispersion, making it impossible to determine the coupling parameter by fitting the frequency dispersion to the Fourier transform of a Kohlrausch function. Notwithstanding, the reduction of the data to primitive relaxation time offers a way to understand

the anomalies. The most probable $\tau_\beta^*(T)$ is related to $f_{\max,\beta}^*(T)$ by the approximate relation $1\Big/\left[2\pi\tau_\beta^*(T)\right] = f_{\max,\beta}^*(T)$. Since the observed most probable frequency of the β-relaxation has an Arrhenius dependence, it follows from Eq. (3.3) that the primitive relaxation time $\tau_\beta(T)$ also has another Arrhenius T dependence $\tau_\beta = \tau_{\beta\infty}\exp\left(E_{a\beta}\Big/RT\right)$. Here $E_{a\beta}$ and $\tau_{\beta\infty}$ are respectively the activation enthalpy and prefactor of the primitive relaxation time of rotational motion of the mesogenic group about its long axis. Due to the close resemblance in chemical structures of the mesogenic group to the monomer unit of BPA-PC and the strong similarity of rotational motion of the mesogenic group (β-relaxation) in the SCLCPs studied by Schönhals et al. and the rotations of the phenyl rings in the γ-relaxation in BPA-PC (see Section 2.3.2.38), we can take $E_{a\beta}$ and $\tau_{\gamma\infty}$ to have approximately the same values as the corresponding quantities $E_{a\gamma}$ and $\tau_{\gamma\infty}$ deduced earlier for the γ-relaxation. The values $E_{a\gamma} = 13$ kJ/mol and $\tau_{\gamma\infty} = 6.5\times10^{-13}$ s have been obtained from NMR measurement in dilute solution of BPA-PC [1470] and from theoretical calculations [1472, 1473]. Therefore the value $E_{a\beta} = 13$ kJ/mol is used for the analysis of the experimental data of Schönhals et al.

The concentration fluctuations give rise to a distribution of environments seen by the mesogenic groups. The different environments introduce a distribution of primitive relaxation times about the most probable value $\tau_\beta(T) = \tau_{\beta\infty}\exp\left(E_{a\beta}\Big/RT\right)$ as well as possibly a distribution of coupling parameter with most probable value n. From the CM equation (3.3) the corresponding most probable effective relaxation time $\tau_\beta^*(T)$ is given by $\tau_\beta^*(T) \equiv \tau_{\beta\infty}^*\exp\left(E_{a\beta}^*\Big/RT\right)$ with

$$\tau_{\beta\infty}^* = \left[t_c^{-n}\tau_{\beta\infty}\right]^{1/(1-n)} \quad \text{and} \quad E_{a\beta}^* = E_{a\beta}/(1-n). \tag{3.41}$$

X-ray measurement [1618] shows that an increase in the order of the mesophase is accompanied by a decrease in the mean lateral mesogenic distance. From this result, we expect that the increase in order of the mesophase will pack the mesogenic groups closer together, enhance their mutual constraints, and cause the coupling parameter n to increase. In fact, the values of n calculated from the expression $\left(1 - E_{a\beta}\Big/E_{a\beta}^*\right)$ for different mesophases are in agreement with this expected trend, as shown in Table 3.7 as well as in Fig. 298.

With the values of n for the SCLCPs with various mesophases determined, the critical stage is reached to test if these values of n will be able to explain the compensation law followed by $f_{\beta\infty}^* \equiv 1/(2\pi\tau_{\beta\infty}^*)$ and the large spread of its observed values ranging from $10^{12.8}$ Hz to $10^{19.4}$ Hz, which is exhibited in the right panel of Fig. 298 in a plot of $f_{\beta\infty}^*$ against n (solid triangles) of the various mesophases. This test is made by solving $f_{\beta\infty}^* = (2\pi)^{-1}\left[t_c^{-n}\tau_{\beta\infty}\right]^{-1/(1-n)}$ for the primitive prefactor $\tau_{\beta\infty}$ for each SCLCP with its experimentally determined $f_{\beta\infty}^*$ and n from Table 3.7 and $t_c = 2$ ps for polymers. The results for $\tau_{\beta\infty}$ give immediately $f_{\beta\infty} = 1\Big/\left(2\pi\tau_{\beta\infty}\right)$. The values of $f_{\beta\infty}$ obtained for all 10 SCLCPs are also listed in Table 3.7 and shown in the right panel of Fig. 298. It is important to recognize that

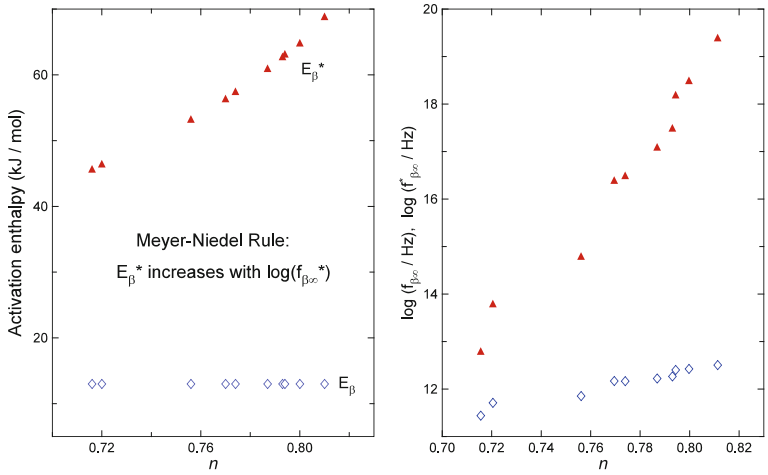

Fig. 298 (*Left*) The *x*-axis is the coupling parameter n of 10 SCLCPs with various mesophase structures (see Table 3.7). Each of the 10 *open diamonds* stands for the point (n, E_β). Each of the 10 *solid triangles* stands for the point (n, $E^*_\beta E^*_\beta$). (*Right*) The *x*-axis is the coupling parameter n of 10 SCLCPs with various mesophase structures. Each of the 10 *solid triangles* stands for the point (n, $f^*_{\beta\infty}$). Each of the 10 *open diamonds* stands for the point (n, $f^*_{\beta\infty}$), where $f_{\beta\infty}$ is calculated with $t_c = 2$ ps and $f^*_{\beta\infty}$ (from experiment, see Table 3.7). Reproduced from [1619] by permission

these results have been obtained in effect without any adjustable parameters because n has been independently determined by the relation between the experimental value of the activation enthalpy $E^*_{a\beta}$ and the known value of $E_{a\beta}$.

In the right panel of Fig. 298, $f^*_{\beta\infty}$ and the corresponding $f_{\beta\infty}$ (open diamonds) are plotted simultaneously against n of the SCLCPs. In contrast to the large spread of almost seven decades shown by $f^*_{\beta\infty}$, the primitive prefactor $f_{\beta\infty}$ has a narrow spread of one decade. The trend that $f_{\beta\infty}$ increases moderately with n is apparent from the figure. Since n increases with decreasing lateral mesogenic distance, the observed trend can be restated as a moderate increase of $f_{\beta\infty}$ with decreasing lateral mesogenic distance. The latter is physically possible and reasonable because $f_{\beta\infty}$ is an attempt frequency which, like a vibration frequency, is expected to increase with decreasing inter-mesogenic distance because the latter causes the potential energy well to become steeper. All values of $f_{\beta\infty}$ lie within the narrow range of physically reasonable values, $10^{11.5} \le f_{\beta\infty} \le 10^{12.5}$, and can be readily interpreted as the pre-exponential factor of the rotational frequency of the mesogenic group. Moreover, the values are close to the primitive prefactor of the γ-relaxation in BPA-PC $f_{\gamma\infty}$ defined as $f_{\gamma\infty} = 1/(2\pi\tau_{\gamma\infty})$ and have been previously determined to have the value of $10^{11.48}$ Hz. In fact, this value of $f_{\gamma\infty}$ obtained from an earlier work [1620] is nearly identical to $f_{\beta\infty}$ of the SCLCP with isotropic mesophase (P1 in Table 3.7). The good correspondence between the order of magnitude of the primitive prefactor of the β-relaxation of the SCLCPs and that of the closely related γ-relaxation of BPA-PC is not an accident but the result of similar physics, i.e., cooperative dynamics of densely packed mesogenic groups and phenyl rings of similar chemical structures.

The observed dramatic increases of the pre-exponential factor $f^*_{\beta\infty}$ and the activation energy $E^*_{a\beta}$ of the β-relaxation rate with the mesophase structure can now be understood in the framework of the coupling model. The increase in the order of the mesophase enables the mesogenic groups to pack closer together and causes intermolecular cooperativity or the coupling parameter n to increase. The increase of n is responsible for the large observed variations of $f^*_{\beta\infty}$, and $E^*_{a\beta}$ and the compensation law obeyed by their variations. The prefactor and the activation energy of the primitive relaxation time recovered from the anomalous experimental data are physically reasonable. This supports reality of the primitive relaxation as well as its relation to the many-body cooperative relaxation as described by the CM equations.

3.2.6.2 Dynamics of Cross-Linked Junction of a Polymer Network

The classical approach to rubber elasticity considers only the chain entropy and internal energy contributions to the elastic energy of a network. Any effect of intermolecular interactions is ignored, based on the idea that such interactions are independent of the chain configurations and thus do not modify the stress. The deviation of experimental results from the predictions of classical theory, as exemplified by the strain dependency of the elastic modulus (defined as the ratio $\sigma/(\lambda - \lambda^{-2})$, where σ is the stress and λ the extension ratio), has led to refinements which take into account the effect of interactions among the network chains. In the Flory description [1621–1623], the intermolecular interactions reduce the configurations available to the network chains by constraining the network junctions. The reduced effectiveness of these constraints upon deformation gives rise to a strain-dependent elastic modulus.

Rubber elasticity theories restrict their concerns to the properties of the network in mechanical equilibrium. However, experimental studies reveal analogies in the behavior of elastomers and polymer melts [1624], which bespeak a connection between elastic and dynamic properties, suggesting that unifying concepts may underlie thermodynamic theories and dynamic models. By providing information on the dynamics of networks, recent experimental advances reinforce the idea that the microscopic motions and the elastic properties can be usefully interrelated. For example, quasielastic neutron scattering measurements probe the motions of the network cross-links [1625, 1626]. In end-linked polydimethylsiloxane, it was observed that the junctions diffuse on the same timescale as the network chains, although the spatial extent of the cross-link motion is reduced by intermolecular constraints [1626].

^{31}P-NMR spin-lattice relaxation measurements on a series of polytetrahydrofuran networks with tris(4-isocyanatophenyl)thiophosphate junctions have been carried out [1515] to study junction dynamics and their dependencies on cross-link density and diluent concentration. These less conventional techniques (as far as the study of rubber elasticity is concerned) provide information that is consistent with existing rubber elasticity models, yet demonstrates that a void exists. There is a conspicuous absence of theories which specifically describe the

junction dynamics. The new experimental findings invite a new approach from a totally dynamic point of view; mechanical equilibrium properties can be considered as only a special or a limiting case (albeit a very important one). The CM has provided such a new approach [1516, 1517]. The adequacy of this application of the CM to address dynamic response of networks is demonstrated here by analyzing the informative ^{31}P-NMR spin-lattice relaxation data [1515] and by revisiting the change of mechanical relaxation on deforming glassy polymers presented before in Section (2.2.5.9 (I)). Before addressing the experimental data, it is instructive to show the connection between the constrained junction model of Flory for rubber elasticity and the CM approach for dynamics of junctions.

Connections Between Flory's Constrained Junction Model and the Coupling Model

The restrictions on the configurations available to the cross-link junctions of a network, arising from its presence in dense phase, govern the mechanical properties of elastomers. These constraints also give rise to intermolecular correlations and cooperativity of the junction motions, and hence can be described by the CM. The close connection between the elasticity of networks and junction dynamics can be illustrated through a comparison of the predictions of the CM for constraint dynamics with the constrained junction model of Flory. This comparison given in Table 3.8 is enlightening because it shows that the gist of the CM for interacting or constrained dynamics is compatible with the idea of Flory in his constrained junction model.

Flory modeled the effects of restrictions imposed by neighboring chains on the fluctuations of network junctions, deriving an expression for the modification of the elastic stress for a network of phantom chains. Analogously, the CM (when applied to junctions in polymer networks) uses the dynamics of the constraints on junctions to model the slowing down of the motions of the network junctions caused by interactions with neighboring chains and thus obtain the modification of the (primitive) correlation function of relaxation of junctions $C_0(t)$. From the idea that phantom chains are able to freely pass through one another, we expect that $C_0(t)$ has an exponential time dependence $\exp\left[-(t/\tau_0)\right]$. At temperatures sufficiently above T_g, τ_0 can be well approximated by the Arrhenius temperature dependence $\tau = \tau_\infty \exp(E_a/RT)$ with the activation energy E_a given by the true microscopic conformational energy barrier to motion of junctions in the phantom network model. Following the general physical principle behind the CM, the junction constraints will modify $C_0(t)$ to $C_c(t) = \exp[-(t/\tau^*)^{1-n}]$ with $\tau^*(T) \equiv \tau^*_\infty \exp\left(E^*_a/RT\right)$, and will give rise to the two relations $\tau^*_\infty = (t_c^{-n}\tau_\infty)^{1/(1-n)} = \tau_\infty(\tau_\infty/t_c)^{n/(1-n)}$ and $E^*_a = E_a/(1-n)$. These relations tells us that the degrees of modification of the pre-exponential and the activation energy from the phantom network values τ_∞ and E_a to the constrained values τ^*_∞ and E^*_a increase with n. Typically τ_∞ is of the order of 10^{-13}–10^{-14} s. This, together with $t_c \geq 2$ ps, indicates that the ratio τ_∞/t_c is much less than unity. Hence, both $\log(\tau_\infty/\tau^*_\infty)$ and the ratio E^*_a/E_a increase with n or the severity of constraints. Higher cross-link densities and cross-link functionality will

Table 3.8 Close connection between the elasticity of networks and junction dynamics illustrated through a comparison of the predictions of the CM for constraint dynamics with the constrained junction model of Flory. The comparison is borne out by NMR results on networks

Network feature	Anticipated effect	Flory model, f_c	CM			^{31}P-NMR[a]		
			n	$\frac{E_a^*}{E_a} - 1$	$\log(\tau_\infty/\tau_\infty^*)$	n	$\frac{E_a^*}{E_a} - 1$	$\log(\tau_\infty/\tau_\infty^*)$
Higher cross-link density	More firmly imbedded junction	Higher[b]	Higher	Higher	Higher	Higher[g]	Higher[h]	Higher[i]
Diluent	Reduced severity of constraints	Lower[c]	Lower	Lower	Lower	Lower[g]	Lower[h]	Lower[i]
Higher cross-link density	More constrained junctions	Higher[d]	Higher	Higher	Higher			
Extension	Alleviation of constraints	Lower[e]	Lower[f]	Lower[f]	Lower[f]			

[a]Reference [1515]; [b]Reference [1627]; [c]Reference [1623, 1628]; [d]Reference [1627, 1629]; [e]Reference [1623, 1630–1633]; [f]Tentative (see [940]); [g]See Fig. 299 (left); [h]See Fig. 299 (right); [i]See Fig. 300

enhance the strength of the intermolecular constraints and consequently n. On the other hand, with the addition of diluent, the junctions become increasingly isolated from the neighboring chain segments so that the strength of the intermolecular constraints and hence n decreases. Such a decrease of n with diluent concentration has been seen in the case of the local segmental motion in amorphous polymer solutions (see Section 2.2.5.7) and the terminal motion of barely entangled polymer solutions (see Section 3.22). The data of these other systems have been explained by a reduction of intermolecular constraints and the coupling parameter. In fact, in these cases the experimental data gave direct evidence of the decrease of n with diluent concentration [849, 1634].

Comparison with Experimental Results of ^{31}P-NMR Spectroscopy

New insight has been provided by the solid-state ^{31}P-NMR spin-lattice relaxation measurements of Shi et.al. [1515] on a series of polytetrahydrofuran networks. The relaxation properties of the tris(4-isocyanatophenyl) thiophosphate junctions were characterized in networks with strand molecular weights ranging from 250 to 2900. The dominant mechanism for ^{31}P nuclear spin relaxation was identified to be chemical shift anisotropy. The spin-lattice relaxation times measured over a wide range of temperatures were fitted by spectral density functions derived from the appropriate Fourier transforms of the stretched exponential correlation function, with τ^* assumed to have the Arrhenius temperature dependence. From these fits, Shi et al. obtained the coupling parameter n, the apparent pre-exponential factor τ^*_∞, and the apparent activation energy E^*_a for the networks of different cross-link densities, both neat and diluted. The coupling parameter was found to increase with decreasing molecular weight between cross-links and, at constant cross-link density, decrease with the addition of diluent. Averages of the values of n determined for each sample from ^{31}P spin-lattice relaxation data by two parallel methods (cross polarization and direct polarization) are plotted in Fig. 299. These results are in accord with expectations based on the CM [1516, 1517].

The apparent activation energy E^*_a is also found to increase significantly with higher cross-link density and, at constant cross-link density, decrease with the addition of diluent. In the right panel of Fig. 299 we have plotted the averages of the E^*_a values determined by the two NMR methods. The products $(1–n)E^*_a$ obtained by using the experimentally determined values of the coupling parameter (left panel) and the apparent activation energy E^*_a for all samples have essentially the same value of 26.2 kJ/mol. This constancy is predicted by the coupling model, since the product, being the true microscopic energy barrier E_a to motion of junctions in a phantom network, is independent of intermolecular interactions or constraints and hence should be independent of cross-link density and dilution. It is worthwhile to point out that 26.2 kJ/mol is of the correct magnitude for the intramolecular conformational energy barrier of polymers with structure similar to the PTHF network junctions. Alternatively, we have calculated E^*_a by the relation $E^*_a = E_a/(1 - n)$ using the experimentally determined coupling parameters (right panel of Fig. 299) and a constant value of $E_a = 26.2$ kJ/mol. The results in the right panel of Fig. 299

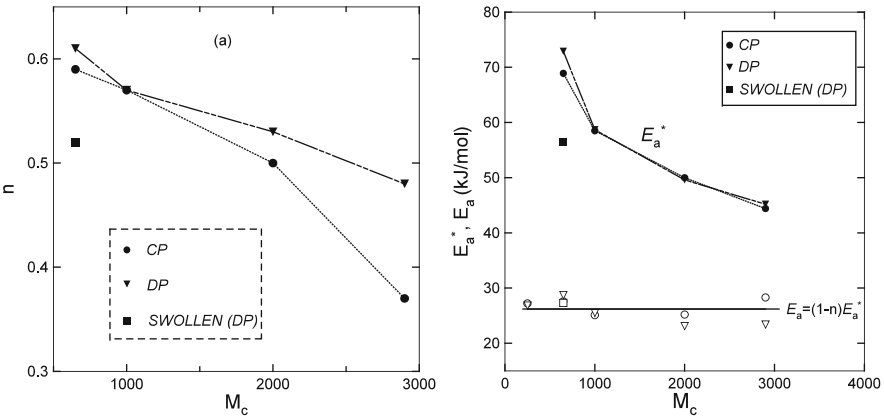

Fig. 299 (*Left*) The coupling parameter of junction dynamics n (*filled circles*) obtained by taking the average of the two values determined by Shi et al. from their ^{31}P-NMR data taken using cross and direct polarizations [1515] for four polymer networks with different molecular weights between cross-links M_c. The *filled square* is the corresponding coupling parameter obtained in a similar manner for a swollen sample with $M_c = 650$. The *smooth curve* drawn through the data points is a visual aid only. (*Right*) *Filled triangles* represent the apparent activation enthalpy E_a^*, obtained by an average of the two values determined by Shi et al. from their ^{31}P-NMR data using direct and cross polarizations for four polymer networks. *Filled square* is E_a^* for the swollen polymer network having $M_c = 650$. The *corresponding unfilled symbols* are the theoretical predicted values of the coupling model calculated by the equation $E_a^* = E_a/(1-n)$ using a constant $E_a = 26.2$ kJ/mol and the coupling parameters n for the same five network polymers given in the *left panel*. A smooth curve has been drawn through the calculated points to guide the eyes. Data from [1516] are replotted in all figures here

suggest good agreement with the experimental values of E_a^* for five samples of different cross-link densities and diluent concentrations.

The raw ^{31}P-NMR data give unphysically short times of the pre-exponential factor τ_∞^* (10^{-16} to 10^{-19} s) and the trend that τ_∞^* decreases dramatically with higher cross-link density (see Fig. 300). The experimental values for τ_∞^* in this figure are the geometric mean of the values obtained by the two NMR methods used. These anomalous properties of τ_∞^* can be explained by the other equation of the CM $\tau_\infty^* = (t_c^{-n}\tau_\infty)^{1/(1-n)} = \tau_\infty(\tau_\infty/t_c)^{n/(1-n)}$. The prefactor τ_∞ corresponds to relaxation of junctions of a phantom network. Thus, its value should be independent of intermolecular interaction and hence of cross-link density and diluent concentration. Since τ_∞ has not been determined directly by experiment, it is taken to be an adjustable (albeit constant) parameter. With the experimentally determined n and a value for the crossover time, $t_c = 4 \times 10^{-12}$ s and $\tau_\infty = 1.5 \times 10^{-14}$ s, the calculated values of τ_∞^* are found to be in good agreement with the experimental values obtained for all five samples, as shown in Fig. 300. The trends of a rapid decrease of τ_∞^* with cross-link density and an increase upon dilution are reproduced.

Universal Features

The physical aspects of junction dynamics of networks discussed above are isomorphic to the dynamics of β-relaxation of the mesogenic group in side-chain liquid

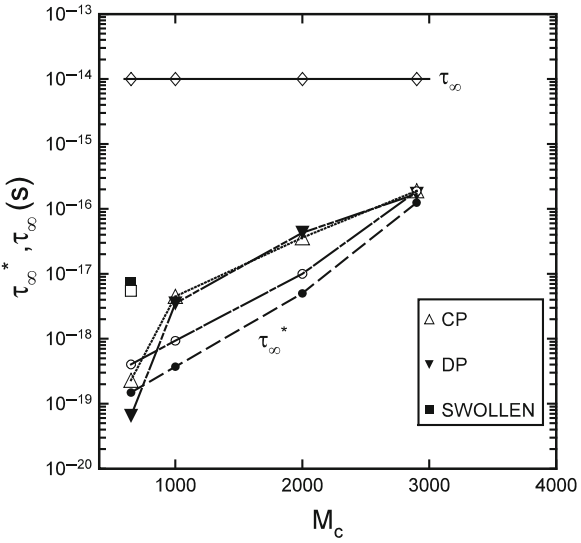

Fig. 300 *Filled diamonds* are the apparent pre-exponential factor τ_∞^* determined by Shi et al. from their experimental data [1515] for the four polymer networks by cross and direct polarizations. *Filled square* is τ_∞^* for the swollen polymer network with $M_c = 650$. The corresponding *open symbols* represent the theoretical predictions of the coupling model calculated by the equation indicated in the figure using constant values of $\tau_\infty = 1.5\times10^{-14}$ s and $t_c = 4\times10^{-12}$ s independent of M_c and diluent concentration. The coupling parameters used here are taken from the data in Fig. 299. For clarity a smooth curve is drawn through the calculated points. Data from [1516] are replotted here

crystalline polymers discussed in Section 3.2.6.1 and ion dynamics in crystalline and glassy ionic conductors (Section 3.2.5). These are entirely different systems and relaxation processes, and yet the anomalies found are analogous.

Effect of Deformation

In Flory's constrained junction model of elasticity, elongation alleviates the restrictions of junctions from neighboring segments [1623], in that the "domain" of the constraints extends along the stretch direction. The elastic behavior of the network thus becomes more phantom-like at higher elongations, in agreement with experiments [1630–1633]. We anticipate that this alleviation of the constraints on the junctions by elongation will be manifested in the junction dynamics. The junctions have higher mobility at higher elongations. If this is the case, the coupling model predicts a decrease of n with extension, along with corresponding changes in relaxation time τ^* and its E_a^* and τ_∞^*. Such experiment has not been carried out to reveal the expected changes in the network dynamics associated with elongation. An analogue of this is the non-linear deformation of glassy polymers including bisphenol A polycarbonate and polystyrene. As discussed in Section 2.2.5.9(I), decrease of n and shorter τ^* by large deformation were found experimentally in glassy polymers.

3.2.6.3 Cooperative Oxygen Ion Dynamics in $Gd_2Ti_{2-y}Zr_yO_7$

The oxygen ion conductors with pyrochlore structure $A_2B_2O_7$ are promising materials for use in fuel cells [1635–1637]. The pyrochlores $Gd_2Ti_{2-y}Zr_yO_7$ are particularly interesting since the concentration of mobile oxygen vacancies can be increased by substitution of Zr for Ti, and oxygen ion conductivity shows the highest value found among materials with pyrochlore structure. For $y < 1.8$ the conductivity is comparable to that of YSZ (10^{-2} S/cm at 700°C). Molecular dynamics [151, 152] and static lattice energy minimization simulations [153] have suggested that oxygen diffusion in $Gd_2Ti_{2-y}Zr_yO_7$ occurs by hopping from 48*f* site to 48*f* site. This result has been later confirmed by XPS measurements [1637]. The oxygen occupancy of 48*f* sites is 1 (or very close to 1) for Zr contents below $y = 0.6$ but decreases progressively as Zr content is further increased [1638]. These vacancies in 48*f* sites are responsible for oxygen hopping and diffusion, and explain the increase of more than two orders of magnitude in dc conductivity at 600°C observed when increasing Zr content from $Gd_2Ti_{1.4}Zr_{0.6}O_7$ to $Gd_2Zr_2O_7$ [1635]. Although the activation energies E_σ of the dc conductivity increases monotonically with y from $E_\sigma = 0.70$ eV for $y = 0.5$ to $E_\sigma = 1$ eV for $y = 2$ [1639, 1640].

More recent measurements of E_σ by Moreno et al. [150] are shown in the left panel of Fig. 301 for six samples with Zr content of $y = 0.5, 0.7, 0.9, 1.3, 1.8$, and 2. However, the energy barrier for oxygen hopping from 48*f* to 48*f* sites E_a has been previously calculated. From molecular dynamics simulations [151, 152], E_a ranges from 0.57 to 0.64 eV, and from static lattice energy minimization simulations [153], $E_a = 0.58$ eV. Two problems or anomalies present themselves. One is

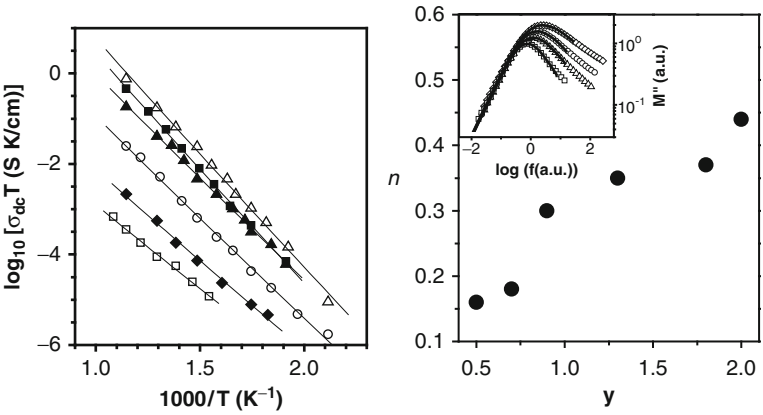

Fig. 301 (*Left*) Arrhenius plot of dc conductivity in the series $Gd_2Ti_{2-y}Zr_yO_7$ for different Zr contents: $y = 0.5$ (*open squares*), 0.7 (*closed diamonds*), 0.9 (*open circles*), 1.3 (*closed triangles*), 1.8 (*open triangles*), and 2 (*closed squares*). (*Right*) Dependence of the exponent n obtained from fits of electric modulus data to Fourier transform of the Kohlrausch function, as a function of Zr content in $Gd_2Ti_{2-y}Zr_yO_7$. The *inset* shows the imaginary part of the electric modulus for samples (*from top to bottom*) with $y = 2, 1.3, 0.9$, and 0.5. Note that experimental data in the *inset* have been horizontally and vertically shifted for clarity. Reproduced from [150] by permission

that the actual energy barrier for oxygen ion hopping E_a is significantly smaller than the observed E_σ. The other is the monotonic increase of E_σ with y. These anomalies are analogous to those found in other interacting systems. These include the conductivity relaxation in other ionic conductors, β-relaxation in side-chain liquid crystalline polymers, and motions of polymer chains, where the anomalies originate from many-body relaxation dynamics and have been explained by the CM through the coupling parameter n.

To resolve the anomalies, the key step was taken by Moreno et al. in determining n for the conductivity relaxation as a function of frequency in $Gd_2Ti_{2-y}Zr_yO_7$ using impedance spectroscopy. The imaginary part of the electric modulus $M''(f)$ from the impedance spectroscopy measurements of $Gd_2Ti_{2-y}Zr_yO_7$ is shown in the inset of the right panel of Fig. 301. It can be seen that the width of the $M''(f)$ loss peak increases with y. $M''(f)$ calculated by using the Kohlrausch function for $\Phi(t)$ in Eq. (1.56) was used to fit the data, and the coupling parameter n was determined for all six samples from the good fits found. The results shown in the right panel of Fig. 301 show systematic and significant increase in n as Zr content is increased from $y = 0.5$ to 2.0. It is known that increasing Zr content above $y = 0.5$ results in creating vacant 48f sites which are responsible for oxygen hopping motion [1638], resulting in higher charge carrier (oxygen vacancies at 48f sites) concentration. The increase also creates higher disorder in both the cationic and anionic sublattices [1637]. Both effects act in concert to enhance mutual interactions between the carriers, which lead to the increase of the coupling parameter n with y as expected by the CM, as observed by experiment. From this, the observed increase of the dc conductivity activation energy E_σ with y follows as a consequence of the CM equation (3.23), now written as

$$E_\sigma(y) = E_a/\left[1 - n(y)\right], \tag{3.42}$$

together with the facts that the energy barrier for oxygen hopping from 48f to 48f sites E_a is independent of y and n is a monotonic increasing function of y.

Furthermore, from the values of $E_\sigma(y)$ and $n(y)$ obtained from experiment, we can form the product $[1-n(y)]E_\sigma(y)$. According to the CM, it should be the microscopic energy barrier E_a for an oxygen ion to jump from one 48f site to a neighboring 48f sites. The products from the six samples all lie within the range of 0.60 ± 0.03 eV and can be considered as nearly independent of y as expected. This is shown in Fig. 302.

The mean value of 0.60 eV is in excellent agreement with recent calculations of the energy barrier an oxygen ion must overcome to hop from one 48f site to a neighboring one from molecular dynamics simulations (0.57–0.64 eV) [151, 152] and from static lattice energy minimization simulations (0.58 eV) [153]. This result offers proof of the verity of the primitive relaxation time. The observed slow relaxation time and its properties are the consequence of the many-ion cooperative dynamics originating from Coulomb interaction between the ions. Cooperative oxygen ion dynamics is not only a subject of fundamental interest but also a key factor in determining the dc ionic conductivity value for practical applications.

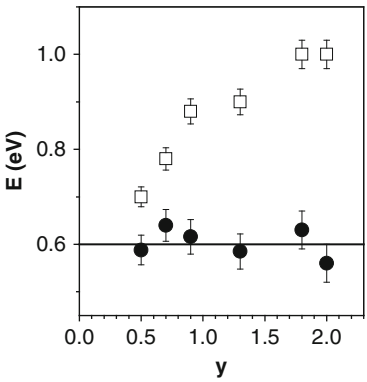

Fig. 302 Activation energies E_σ (□) and $E_a = (1 - n)E_\sigma$ (•) as a function of Zr content in $Gd_2Ti_{2-y}Zr_yO_7$. *Solid line* represents the average value $E_a = 0.60$ eV obtained for the primitive energy barrier for oxygen hopping. Reproduced from [150] by permission

In the discussion above for $Gd_2Ti_{2-y}Zr_yO_7$, increase in activation energy E_σ when increasing Zr content is explained by the increase in the degree of correlations among mobile oxygen ions in the oxygen ion diffusion process as the structure becomes more disordered. This explanation is supported by the concomitant increase in n, which is a measure of the many-ion conductivity relaxation dynamics. If the effect and the interpretation are general, one would expect that replacing Gd in $Gd_2Ti_{2-y}Zr_yO_7$ by other lanthanides such as Y and Dy, both the exponent n and the activation energy E_σ also will increase with Zr content in $Y_2Ti_{2-y}Zr_yO_7$ and in $Dy_2Ti_{2-y}Zr_yO_7$. This is in fact observed by Díaz-Guillén et al. [1645]. It is noted that the increase in E_σ occurs despite increasing cell volume, indicating that it is caused by the enhancement of ion–ion correlations and the increase in n, in accordance with the coupling model predictions.

As for the primitive energy barrier $E_a(y)$, its value is given by the product $[1 - n(y)]E_\sigma(y)$, according to the CM. We have seen from Fig. 302 for the $Gd_2Ti_{2-y}Zr_yO_7$ series that the calculated values of $E_a(y)$ are approximately constant and in agreement with the values obtained by molecular dynamics simulations and by static lattice energy minimization simulations. The same was found for the two other series $Y_2Ti_{2-y}Zr_yO_7$ and $Dy_2Ti_{2-y}Zr_yO_7$, as shown in Fig. 303(a)–(c), which are like Figs. 301 and 302 for the $Gd_2Ti_{2-y}Zr_yO_7$ series.

Moreover, increasing order and concomitant decrease in E_σ as well as n was found by annealing at a higher temperature of $Dy_2Ti_{0.45}Zr_{0,56}O_7$ [1646]. On the other hand, E_a calculated by the product $[1 - n]E_\sigma$ remains nearly independent of the annealing temperature. All these supplementary data support once more the verity of the primitive relaxation through its primitive activation energy.

3.2.6.4 The Crystalline Lithium Ionic Conductor $Li_{3x}La_{2/3-x}TiO_3$ (LLTO)

For some ionic conductors that have the dc conductivity σ_{dc} measured over an extended range of temperature to reach high σ_{dc} levels, the complete temperature dependence of σ_{dc} is non-Arrhenius. Examples can be taken from some ionic conductors in Table 3.1, and they can be glassy, molten, or even crystalline. Specific

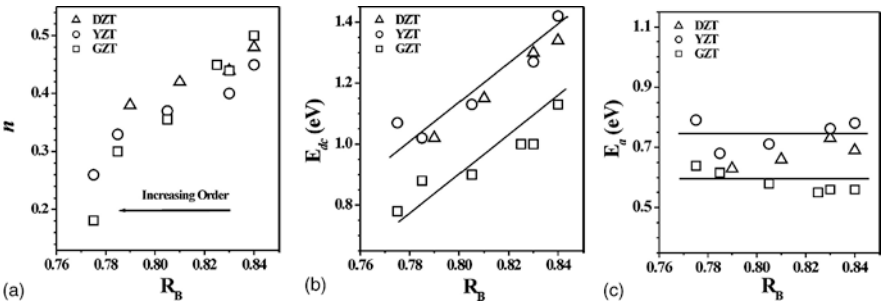

Fig. 303 Dependences on the average cation size R_B of (**a**) the exponent n, (**b**) the dc conductivity activation energy E_{dc}, and (**c**) the primitive activation energy E_a for samples in the series of $Dy_2Zr_{2-y}Ti_yO_7$ (DZT), $Y_2Zr_{2-y}Ti_yO_7$ (YZT), and $Gd_2Zr_{2-y}Ti_yO_7$ (GZT). Note that the absolute scales in (**b**) and (**c**) are the same, and the *solid lines* are shown only to emphasize the trends. Reproduced from [1645] by permission

examples include the fast silver ion-conducting glasses by Kincs and Martin [1536] and the crystalline lithium ionic conductors $Li_{3x}La_{2/3-x}TiO_3$ (LLTO); a special case is $Li_{0.18}La_{0.61}TiO_3$ by León et al. [1484]. This non-Arrhenius behavior, seemingly a universal feature in fast ionic conductors as dc conductivity approaches values about 10^{-1} S/cm (see Table 3.1), may not be too surprising. This is because when $\sigma_{dc} \approx 1$ S/cm, the conductivity relaxation time τ_σ would be shorter than the crossover (to primitive relaxation) time $t_c \approx 1$ ps as discussed in Section 3.2.3 and demonstrated in [1537, 1538]. However, the crystalline ionic conductor LLTO exhibits non-Arrhenius behavior at levels of σ_{dc} much lower than 1 S/cm, as shown in the left panel of Fig. 304.

For crystalline ionic conductors such as LLTO and glassy ionic conductors that remain deep in the glassy state throughout the entire temperature range, the observed non-Arrhenius T dependence of σ_{dc} or τ_σ offers a challenge for an explanation. This is because the activation energy should be constant since the structure and hence the energy barrier opposing ion hopping remains unchanged. By the same token, the primitive activation energy E_a in the CM should also be constant. Notwithstanding, the explanation from the CM model is the change of ion–ion correlation effects caused by decrease of coupling parameter n_σ as τ_σ becomes shorter on increasing temperature. There is an analogue of this behavior in the structural relaxation of many glass-forming substances (see Chapter 2), where the coupling parameter n_α of the structural α-relaxation shows monotonic decrease with decrease in τ_α by raising temperature. It can be readily seen from the CM equation $\tau_\sigma(T) = [t_c^{-n_\sigma(T)}\tau_0(T)]^{1/(1-n_\sigma(T)}$ that $\tau_\sigma(T)$ is non-Arrhenius even though $\tau_0(T) = \tau_{0\infty}\exp(E_a/kT)$ is strictly Arrhenius if n_σ is temperature dependent. The same applies to σ_{dc} because $\sigma_{dc}(T) = \varepsilon_0\varepsilon_\infty/ < \tau_\sigma(T) >$, where $< \tau_\sigma(T) >= [\Gamma(1/\beta_\sigma)/\beta_\sigma]\tau_\sigma(T)$ and $\beta_\sigma = (1 - n_\sigma)$. This CM explanation also offers an opportunity to recover the primitive relaxation time and the primitive activation energy from the experimental data.

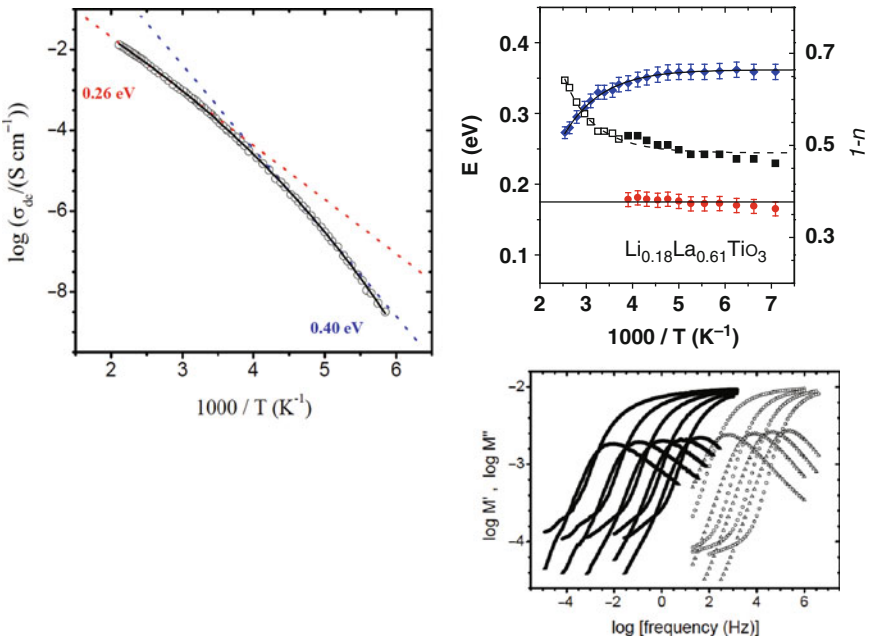

Fig. 304 (*Left*) dc conductivity vs. 1000/T of LLTO, showing a strongly non-Arrhenius behavior. *Dashed lines* indicate the low- and high-temperature activation energies of the Li ion spin relaxation rate, which are 0.4 and 0.26 eV, respectively. *Solid line* is a fitting to VFTH law. Data from León et al. [1484] is replotted here. (*Right*) (*Upper*) Temperature dependence of the dc activation energy E_σ (*diamonds*) and of the Kohlrausch exponent $[1 - n(T)]$ (*solid squares*) describing the dynamic response of ions in $Li_{0.18}La_{0.61}TiO_3$. E_σ has been determined up to 385 K, but $[1 - n(T)]$ only up to 256 K. *Circles* represent the microscopic activation energy E_a estimated by using the CM equation (3.23). It has the constant value of 0.175 eV (*horizontal line*). *Open squares* are the predicted values of the exponent $[1 - n(T)]$ for $256 < T < 385$ K in order that the same constant value, $E_a = 0.175$ eV, is maintained at the higher temperatures according to the relation $E_a = [1 - n(T)]E_\sigma$. Data from [1482] is replotted here. (*Lower*) Spectra of the real (*open circles*) and imaginary parts (*open squares*) of the electric modulus of $Li_{0.18}La_{0.61}TiO_3$ obtained from 121, 131, 141, 150, and 160 K from *left to right*. *Solid symbols* represent spectra of real and imaginary parts of the electric modulus at higher temperatures, 191, 212, 232, and 256 K from the *left to right*. The narrowing of the loss peak on increasing temperature is clear. Data from [1647(a)] is replotted

Combination of time domain and dynamic frequency measurements of the complex electric modulus $M^*(\nu)$ of LLTO has been performed to investigate ion dynamics in the wide frequency range of 11 decades from 10^{-5} to 10^6 Hz and temperatures up to 256 K [1647(a)]. The spectra are shown in the right (lower) panel of Fig. 304, where the narrowing of the loss modulus peak on increasing temperature can be clearly seen. Indeed, this study have found that the exponent $[1 - n_\sigma(T)]$ of the Kohlrausch function used to fit the spectra increases with increasing temperature as shown by the solid squares in the right (upper) panel of Fig. 304. The primitive activation energy $E_a(T)$ calculated via Eq. (3.42) by the product $[1 - n_\sigma(T)E_\sigma(T)]$ are shown by the open circles in the same figure. It can be seen that within errors

the values of $E_a(T)$ obtained are independent of temperature as it should be since it corresponds to the microscopic energy barrier of the crystalline LLTO.

So far, the published electric modulus data give $[1 - n(T)]$ for T up to 256 K, while sizeable decrease of $E_\sigma(T)$ continues up to 385 K. If the CM explanation holds, $E_a(T)$ must still be temperature independent all the way up to 385 K. Assuming this is the case and taking the temperature-independent value of $E_a = 0.175$ eV determined at temperatures lower than 256 K, $[1 - n(T)]$ must have the values shown by open squares in order that the product $[1 - n_\sigma(T)]\, E_\sigma(T)$ remains constant and is equal to $E_a = 0.175$ eV for all temperatures up to 385 K. This offers a further critical test of the CM explanation by extending the measurement of the electric modulus at higher frequencies up to the gigahertz region to determine $[1 - n_\sigma(T)]$ directly at temperatures higher than 256 K. Actually, such measurements of $M^*(\nu)$ for frequencies as high as 1 GHz and temperature reaching 385 K have been made but so far unpublished [1647(b)]. The coupling parameter $n_\sigma(T)$ obtained by fitting the electric modulus by Eq. (1.56) with $\Phi(t)$ as the Kohlrausch function at temperature above 256 K and up to 385 K is in agreement with the predicted values of the exponent $[1 - n_\sigma(T)]$ for $256 < T < 385$ K shown in the right panel of Fig. 304. New measurements confirming the same will be published in the future [1647(c)]. Using the experimentally obtained values of $E_\sigma(T)$ and $n_\sigma(T)$, the calculated products $(1 - n(T))E_\sigma(T)$ should be good estimates of the primitive energy barrier E_a. An approximately constant value of $E_a = 175 \pm 10$ meV is obtained over the whole temperature range (line in the right upper panel of Fig. 304), which is remarkably similar to the value of 170 mV previously determined from electrical conductivity relaxation and NMR spin-lattice relaxation for the microscopic energy barrier [1484]. This result strongly supports the interpretation of a decrease in ion–ion correlation with increasing temperature as the origin of the observed decrease in the exponent n, which in turn explains the parallel decrease of E_σ. For the present purpose, the primitive activation energy E_a is not only recovered from the data but also indeed independent of temperature as it should be in a crystalline ionic conductor.

3.2.6.5 The Crystalline Lithium Ion Conductor $Li_{1.2}Ti_{1.8}Al_{0.2}(PO_4)_3$

Rivera et al. [1647(c)] have also analyzed in a similar way the recent experimental conductivity data of the Nasicon-type ionic conductor $Li_{1.2}Ti_{1.8}Al_{0.2}(PO_4)_3$ obtained by Arbi et al. [1647(d)]. It also shows a non-Arrhenius temperature dependence of the dc conductivity and a decrease of the exponent n with increasing temperature, although it has been measured in a smaller temperature range (from 173 to 323 K). Figure 305 shows the temperature dependence of the dc activation energy E_σ obtained from [1647(d)] (open squares), which changes from 350 meV at low temperatures to 220 meV at the highest temperatures. Using the values of the exponent n determined by those authors (solid squares in the figure), Rivera et al. have calculated the energy barrier E_a by the product $(1 - n(T))E_\sigma(T)$ and found that again an approximately constant value of E_a (open circles in the figure) is obtained over the whole temperature range. This similar finding in a different

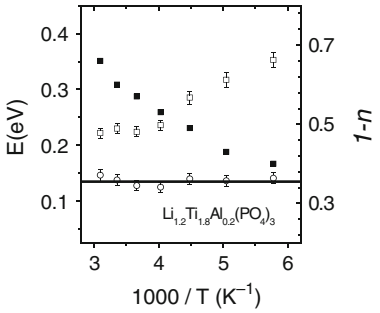

Fig. 305 Temperature dependence of the dc activation energy E_{dc} (*open squares*) and of the exponent n (*solid squares*) describing the dynamic response of ions in $Li_{1.2}Ti_{1.8}Al_{0.2}(PO_4)_3$ after Arbi et al. [1647(d)]. *Open circles* represent the microscopic activation energy estimated by using the coupling model. Reproduced from [1647(c)] by permission

ionic conductor further supports our conclusions derived from the CM analysis of temperature-dependent dynamics in LLTO.

3.2.6.6 Ionic Conductivity of Nanometer Thin Films of Yttria-Stabilized Zirconia

Discussions of the change in dynamics of various glassformers on reducing one or more dimensions to nanometer scale were made Section 2.3.2.33. There experimental data have shown the suppression of the many-body relaxation, obviously due to the reduction in its length scale, and much faster structural α-relaxation than in the bulk. Under extreme confinement or restricting to consideration of the surface layer of thin films, the suppression can be so severe that the observed α-relaxation time τ_α approaches or even assumes the primitive relaxation time τ_0 calculated from the CM or the JG β-relaxation time τ_{JG} of the bulk glassformer. The effect has been demonstrated in ultrathin poly(methylphenylsiloxane) (PMPS) and poly(ethylene oxide) (PEO) films with thickness of the order of 1.5–2.0 nm intercalated into galleries of organically modified layered silicates in Fig. 261 and PDMS confined in 2.5-nm glass pores in Fig. 260. Here we present experimental data of the oxygen ion conductivity relaxation in thin films of yttria-stabilized zirconia (YSZ) to demonstrate that the same effect is observed. This is another example of the universal dynamics manifested in relaxation of interacting systems.

Before we proceed to discuss the oxygen ion conductivity in thin films of YSZ, mention has to be made on the earlier studies by Maier and coworkers in which they found substantial increase of the dc ionic conductivity in superlattices of CaF_2 and BaF_2 when the thickness of the individual layers was decreased down to 16 nm [1648]. The first case involving YSZ is the large enhancement of the in-plane electrical conductivity σ of highly textured thin film of yttria-stabilized zirconia (YSZ) deposited onto an MgO substrate found by Kosacki et al. [1649]. The enhancement started to be observed for films with thickness d less than 60 nm, and σ increases

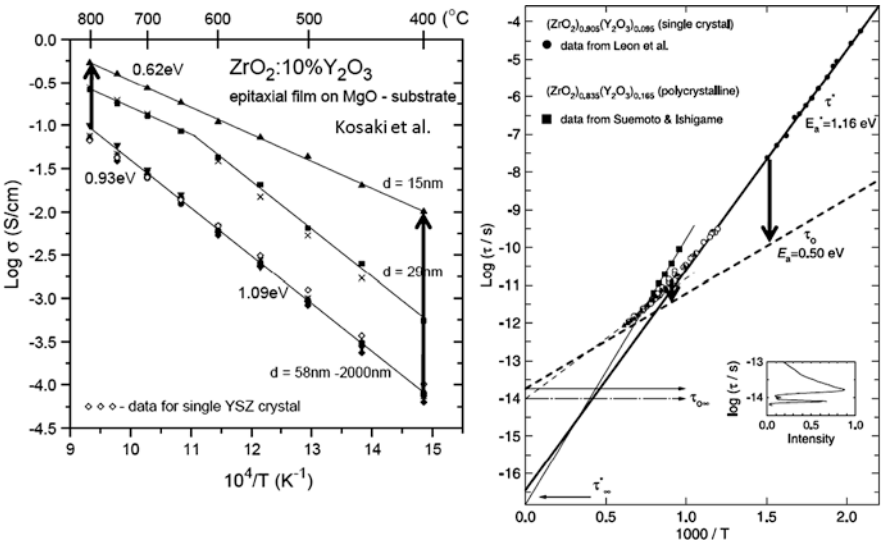

Fig. 306-1 (*Left*) Temperature dependence of the electrical conductivity determined for epitaxial YSZ thin films of different thicknesses. The *thick vertical arrows* indicate the order of magnitude increase of the conductivity at $T \sim 400$ and 800°C. Reproduced from [1649] by permission. (*Right*) Same as Fig. 288 except for the two *thick arrows* at $T \sim 400$ and 800°C to indicate that the difference between the measured conductivity relaxation time of bulk YSZ and the calculated primitive relaxation time is of nearly same order of magnitude as the increase of conductivity of the 15-nm YSZ thin film at the same temperature in the *left panel*. Note that the compositions of the samples in the two figures are not exactly the same

by orders of magnitude with decreasing d down to 15 nm as shown in the left panel of Fig. 306-1. The thick arrows at $T \sim 400$ and 800°C indicate enhancement of σ by about 2 and 0.75 decades, respectively.

The observed increase in conductivity σ was attributed by Kosacki et al. to a significant and dominating contribution from the oxygen transport at the interface, which becomes increasingly important with decrease in the film thickness. From an analysis of the data by these authors, it was estimated that the thickness of interface layer is about 1.6 nm, and interfacial conductivity can be orders of magnitude greater than the bulk-like, lattice-related conductivity depending on the temperature. In the deposited YSZ thin film, there is reduction of inter-ion coupling because of the absence of oxygen ions on one side of the air-YSZ surface as well as in the 1.6-nm interfacial YSZ layer on top of the MgO substrate. The analogy with supported polymer thin films on substrate is evident, where we have seen the surface layer has much higher segmental mobility than bulk from AFM probe of the surface layer of polystyrene thin films by Tanaka et al. [1465(c)] and Forrest and coworker [1465(d), (e)]. The reduction of coupling parameter and the relation to the primitive relaxation time have been demonstrated by Tanaka et al. This is also the case in the observed enhancement of conductivity in the 15-nm YSZ film. The two arrows in the right panel of Fig. 306-1 indicate the difference in order of magnitude between the bulk conductivity relaxation time τ_σ and the primitive relaxation time τ_0 at 400

and 800°C. They are nearly the same as the enhancement of σ observed in the 15-nm epitaxial YSZ thin film at the same temperatures in the left panel of Fig. 306-1. Also the activation energy of σ in the 15-nm epitaxial YSZ thin film is 0.62 eV, which is not far from the 0.50 eV of τ_0, considering the fact that the YSZ in the two cases does not have the same mole percentage of yttria.

Motivated by the observation of Kosacki et al. that enhancement of conductivity increases with decreasing YSZ film thickness and the suggestion that it comes from oxygen ions in the interfacial layer, Garcia-Barriocanal et al. fabricated heterostructures where YSZ layers (with 8 mol% nominal yttria content) in the thickness range from 62 nm down to 1 nm were sandwiched between two 10-nm-thick layers of insulating $SrTiO_3$ (STO) [1650(a), 1650(b)]. Also, superlattices were grown, alternating 10-nm-thick STO films with YSZ layers of thickness between 62 and 1 nm. The thickness of 1 nm corresponds to the dimension of two unit cells of YSZ. The ultrathin layer of YSZ grows rotated by 45° around the *c*-axis and strains to match the STO lattice. Because the bulk lattice constants of STO and YSZ are 0.3905 and 0.514 nm, respectively, the epitaxial growth of the YSZ on top of the STO engenders a large, expansive strain in the thin YSZ layers of 7% in the *ab* plane. The real part of the lateral electrical conductivity σ' of the thinnest 1-nm YSZ film between two 10-nm-thick STO films plotted against frequency f is shown in the left panel of Fig. 306-2. The dc ionic conductivity σ_{dc} of this [$STO_{10\ nm}/YSZ_{1\ nm}/STO_{10\ nm}$] trilayer was determined by the plateau level of σ' (f) and the values are identified by the stars in the figure. The electronic contribution to the ac measurements was negligible, and thus the measured ac transport is attributable to oxygen ion diffusion process [1650(a), 1650(b)]. In the right panel of Fig. 306-2, the temperature dependence of σ_{dc} of the [$STO_{10\ nm}/YSZ_{1\ nm}/STO_{10\ nm}$] trilayers is shown together with data from a single crystal and the 700-nm film. Whereas the bulk and the thick

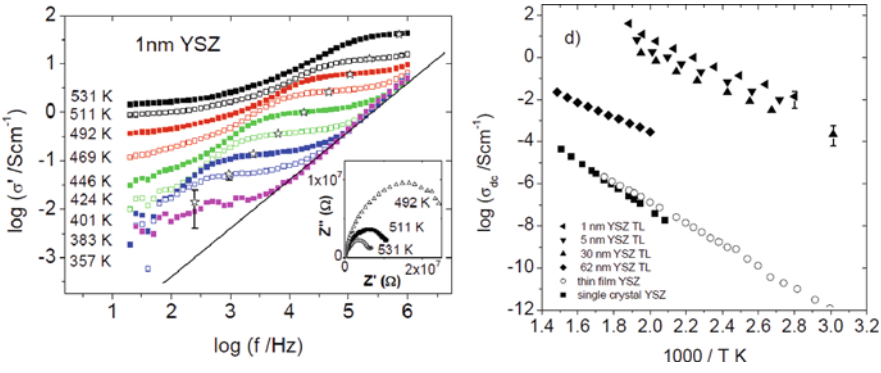

Fig. 306-2 (*Left*) Real part of the conductivity as a function of frequency at several temperatures for a 1-nm YSZ (~8 mol.% yttria content) trilayer with 10-nm STO *top* and *bottom* layers grown on a (100) STO substrate. Isotherms were measured in the range of 357–531 K. The *solid line* represents likely stray capacitance from the STO and not an NCL contribution as originally suggested in [1650(a)]. *Stars* identify the value of σ_{dc}. (*Inset*) Imaginary vs. real part of the impedance (Nyquist) plots at 492, 511, and 531 K. The high-frequency contribution is a Debye-like process characterized by a conductivity exponent $n = 0$

film of YSZ show the well-known Arrhenius behavior with an activation energy $E_\sigma \sim 1.1$ eV, the trilayers show much larger conductivity values and smaller values of the activation energy $E_{\sigma,\text{film}}$ but compensated by much larger pre-exponential factor $\sim \sigma_{\infty,\text{film}}$. The thickest trilayer (62-nm YSZ) already shows an increase of about two orders of magnitude in the high-temperature dc conductivity, and $E_{\sigma,\text{film}}$ decreases to 0.72 eV. When decreasing the thickness of the YSZ layer to 30 nm and then to 1 nm, the dc conductivity increases another three or more orders of magnitude, and $E_{\sigma,\text{film}}$ decreases further to 0.6 eV, nearly the same as 0.62 eV for the 15-nm-thin film of YSZ deposited on MgO (see left panel of Fig. 306-1) and 0.50 eV, the activation energy of the primitive oxygen ion hop. The values of the pre-exponential factor $\sim \sigma_{\infty,\text{film}}$ are as high as $\sim 10^7$ (ohm cm)$^{-1}$. Garcia-Barriocanal et al. concluded that the high conductance observed comes from some interface conduction mechanism, which they supported by conductance measurements of superlattices with [$YSZ_{1\text{ nm}}/STO_{10\text{ nm}}$] as the repeat unit. From the good epitaxial quality of the heterostructures, they believe that the large in-plane expansive strain on the YSZ interface plane, together with the high concentration of vacant oxygen positions and probable positional disorder, leads to uncorrelated ion diffusion at the interface, resulting in the reduction of the activation energy and the huge enhancement of the ionic conductivity. Here, to the cause of the effect, we add the reduction of inter-ion coupling due to the absence of ions on both sides of the YSZ thin films. Like Garcia-Barriocanal et al. have done before, the reduction in coupling parameter n from the bulk value of 0.56 [1542] accounts for the concomitant decrease of activation energy from the bulk value $E_\sigma \sim 1.1$ eV to 0.60 eV according to the CM equation (3.42). Garcia-Barriocanal et al. suggested that the very large pre-exponential factor $\sim \sigma_{\infty,\text{film}}$ is possibly due to an increase in the concentration of oxygen vacancies and a larger entropy term [$\exp(S/k_\text{B})$] is due to an increased number of available positions for the oxygen ions (enhanced positional disorder for the oxygen vacancies) [1650(b)]. Pennycook et al. reported density-functional calculations that trace the origin of the effect to a combination of lattice-mismatch strain and O sublattice incompatibility [1650(c)].

3.2.6.7 Activation Energy of the Snoek–Köster Relaxation in Cold-Worked, Body-Centered Cubic Metals

In body-centered cubic metals such as α-Fe and group-V transition metals, interstitial solute atoms (ISAs) including oxygen, carbon, and nitrogen prefer to sit on octahedral sites and give rise to local strain distortion of tetragonal symmetry. Thus an ISA contributes an elastic dipole of tetragonal symmetry, which can produce anelastic relaxation that can be observed by dynamic mechanical measurements. Recognizing this possibility, Snoek found these anelastic relaxations as peaks by internal friction measurements of Q^{-1} as a function of temperature [1651]. If the ISA concentration is low, the Snoek peak is well described by an exponential Debye relaxation with a single relaxation time τ_S, which is related to the reciprocal of the jump transition rate of the ISA to neighboring sites. It was found that τ_S has an Arrhenius temperature dependence $\tau_\text{S} = \tau_{\text{S}\infty}\exp(H_\text{S}/kT)$, where H_S is the

activation enthalpy of diffusion of the interstitial atoms. After the ISA-containing metal has been cold worked, an additional internal friction peak, called the Snoek–Köster (SK) peak, appears at a higher temperature [1652]. Both the peak position and the peak height depend on the degree of cold work and the ISA concentration [1653–1655]. The activation enthalpy H_{SK} and the width of the SK peak are usually substantially larger than the corresponding quantities of the Snoek peak [1653–1655].

It is generally agreed that the SK relaxation is caused by the bowing out of a dislocation segment under applied stress, dragging along with it the surrounding Cottrell atmosphere of rather high density of ISAs, as suggested by Schoeck [1656]. However, Schoeck's own model did not take into account of the effect that interactions and correlations between the diffusing ISAs have on the SK relaxation. In an application of the CM to the SK relaxation [1653–1655], this effect was incorporated into Schoeck's model. The primitive jump relaxation time of a single ISA without the influence of others is given by the Snoek expression. The interaction/correlation between the diffusing ISAs slows down the diffusion coefficient, resulting in the correlation function of the SK relaxation to the Kohlrausch stretched exponential form:

$$C_{SK}(t) = \exp[-(t/\tau_{SK})^{1-n}], \quad \text{with} \quad \tau_{SK} = \tau_{\infty}^{SK}\exp[H_{SK}/kT]. \tag{3.43}$$

The CM equation relates its activation energy H_{SK} to the activation enthalpy of Snoek H_S by

$$H_{SK} = H_S/(1-n). \tag{3.44}$$

Since the Snoek relaxation activation enthalpies H_S are available from the literature, the SK relaxation offers an excellent opportunity to critically test this CM relation and also to recover the primitive activation energy of the SK relaxation. To verify this relation, literature data of the internal friction peaks from SK relaxation were analyzed and fitted to those calculated from $C_{SK}(t)$. The fits yield the coupling parameters n and the activation energy H_{SK}. These quantities together with H_S are shown in Table 3.9 for α-Fe, Ta, and Nb containing nitrogen (N), carbon (C) and oxygen (O) as ISAs. The product $(1-n)H_{SK}$ in the last column is to be compared with H_S in the neighboring column. It can be seen that H_{SK} is larger than H_S, but the product $(1-n)H_{SK}$ is approximately the same as H_S.

These results of getting the primitive activation energy H_S from H_{SK} of SK relaxation in metals are analogues of the procedure used in the cases of (1) β-relaxation in side-chain liquid crystalline polymers discussed in Section 3.2.6.1 and (2) junction dynamics in Section 3.2.6.2 and Li ion dynamics in Sections 3.2.6.4 and 3.2.6.5.

Reduction of n in Snoek–Köster Relaxation by Decreasing Carbon Concentration

One way of reducing the interaction between ISAs is to decrease their concentration. This can be accomplished in ultra-high purity iron where the carbon concentration

Table 3.9 Values of the coupling parameter n and activation enthalpy H_{SK} of the Snoek–Köster (SK) relaxation together with the activation enthalpy of the Snoek relaxation H_S for α-Fe, Ta, and Nb containing nitrogen (N), carbon (C), and oxygen (O) as ISAs

High-purity specimen	Doped ISA	H_{SK}(eV)	n	H_S(eV)	$(1-n)H_{SK}$ [eV]
α-Fe	N	1.40	0.38	0.796	0.87
α-Fe	C	1.84	0.60	0.87	0.74
Ta (*A*)	O	1.45	0.30	1.10	1.02
Ta (*B*)	O	1.68	0.48	1.10	0.88
Ta monocrystal	O	2.24	0.46	1.10	1.21
Nb	O	1.49	0.40	1.15	0.90
Nb monocrystal	O	1.68	0.50	1.15	0.84

is smaller. One can expect from the CM a reduction of n and a smaller activation energy H_{SK} of the SK relaxation in the ultra pure iron from Eq. (3.44) [1655]. This expectation is fulfilled by the results of an experiment on SK relaxation in ultra-high purity iron carried out by Magalas [1655]. The data of the relaxation parameters H_{SK}, τ_∞^{SK}, and T_{max}^{SK}, of the Snoek–Köster relaxation are presented in Table 3.10. Here T_{max}^{SK} is the temperature of the SK peak at 1 Hz. It can be seen from the table that H_{SK} of the ultra pure iron is reduced to 0.95 eV, which is slightly higher than the value of $H_S = 0.87\,\text{eV}$ (see Table 3.9) and much smaller than 2.1 eV for the H_{SK} of the less pure iron.

The prefactor τ_∞^{SK} of the ultra-high purity iron is 6.26×10^{-12} s compared with 3.71×10^{-19} s of less pure iron. The latter has not only the anomalously short τ_∞^{SK} but also the large $H_{SK} = 2.12\,\text{eV}$, an example of the Meyer–Neldel rule or compensation law of relaxation time in interacting systems. These have analogues in the side-chain liquid crystalline polymers, the junction dynamics, and Li ion conductors. Let us take $n = 0.60$ from the SK relaxation of carbon ISA in Fe given in Table 3.9 from another experiment and assume that this is the same as that of 1000 ppm carbon sample of Magalas, and also assume $t_c = 10^{-11}$ s. With

Table 3.10 Relaxation parameters of stable SK peak in deformed ultra-high purity iron with carbon as ISA at concentration of 25 ppm, compared with another sample with carbon at concentration of 1000 ppm

Carbon concentration					
Total	In solid solution (at ppm)	Deformation at RT (%)	H_{SK}(eV)	τ_∞^{SK} (s)	T_{max}^{SK} (K) at 1 Hz
1000	110	24*	2.12 ± 0.04	3.71×10^{-19}	546.8 ± 0.6
25	5/10	13**	0.95 ± 0.01	6.26×10^{-12}	461.3 ± 0.4

∗ Successive deformation at RT: 13% ($T_a = 673$ K) + 6% ($T_a = 673$ K) + 6% ($T_a = 673$ K)
**First run-up to $T_a = 673$ K, deformation 13%

these assumptions, near physical value of the primitive prefactor $\tau_\infty = 10^{-14}$ s is obtained from the CM equation

$$\tau_\infty^{\mathrm{SK}} = \left[(t_\mathrm{c})^{-n}\tau_\infty\right]^{1/(1-n)} \tag{3.45}$$

and $\tau_\infty^{\mathrm{SK}} = 3.71 \times 10^{-19}$ of less pure iron.

3.2.6.8 Precipitates in Al–Ag Alloys, Ta–H, and Ti–H Systems

The thermal-activated relaxation originating from motion in solute clusters of precipitate in a number of alloys was studied by internal friction measurement at a fixed frequency. The energy loss Q^{-1} measured by internal friction plotted as a function of reciprocal temperature shows up as a broad and asymmetric peak. The shape deviates strongly from the Debye-type relaxation peak with exponential relaxation function but is well accounted for by the Lévy function, which is basically the Laplace transform of the Kohlrausch function [1657(a)]. From the best fit of the position and shape of each internal friction peak, Wang and coworkers [1657(a)] obtained the Kohlrausch exponent (1–n) and the activation energy E_a^* (fit). The results of E_a^* (fit) and n shown together with the experimentally observed value E_a^* (obs.) are given in Table 3.11 for five alloys Al–Ag, Ti–H and Ta–H. The compositions of the alloys are as follows: Al–30 wt% Ag; A1–20 wt% Ag; A1–20.1 wt% Ag; Ti–5.4 at.% H; and Ta–5 at.% H.

Because of solute clustering in the precipitates, Wang and coworkers argued the presence of interaction between the solute atoms and many-body relaxation in the motions of solute atoms, and hence the application of the CM to deduce the true activation energy E_a. Clustering of H in hydrides has been suggested in the light of neutron scattering experiment [1658]. This approach differs from the interpretations proposed by others for the internal friction peak associated with precipitates, all of which neglect the many-body relaxation aspect of the mechanism [1659, 1660]. From the results of Wang and coworkers using the CM, it is easy to understand why the internal friction peak due to the Ag clusters in Al–Ag alloys has the same peak

Table 3.11 The observed apparent activation energy E_a^* (obs.), the calculated apparent activation energy E_a^* (fit), the true activation energy E_a, and the coupling parameter n

Alloy	Structure of alloy	Structure of precipitate	E_a^* (obs.) (eV)	E_a^* (fit) (eV)	E_a (eV)	n
Al–30 wt% Ag	FCC	HCP	1.2 ± 0.1	1.3	0.91	0.3
Al–20 wt% Ag	FCC	HCP	1.2 ± 0.1	1.3	0.91	0.3
Al–20.1 wt% Ag	FCC	HCP	1.09 ± 0.02	1.3	0.91	0.3
Ta–5 at.% H	BCC	BCT	0.38 ± 0.05	0.40	0.10	0.75
Ti–5.4 at.% H	HCP	FCT	0.47 ± 0.01	0.47	0.25	0.44

temperature as that due to γ' precipitates. The latter is due to the stress-induced change in the particle shape (i.e., precipitation and dissolution) for which the rate-limiting process is atom migration around the matrix–precipitate interface. For the Ta–H system, it is puzzling why E_a^* (obs.) (=0.38 eV) in the β_2 phase is much larger than the activation energy (0.12 eV) of hydrogen in α-Ta phase (see Table 3.11). However, it becomes understandable if we take into account of the fact that the true activation energy E_a is 0.10 eV, which is comparable with 0.12 eV.

3.2.6.9 Grain Boundary Relaxation

Kong and coworkers [1657(b)–(e)] made internal friction measurements on various <111> tilt and twist grain boundaries in high-purity Al bicrystals. The temperature dependence of the grain boundary internal friction peak originating from grain boundary relaxation was determined. The activation enthalpy and the pre-exponential factor of the relaxation time are related by the compensation law, just like that discussed for the relaxation parameters of the SK peak in Table 3.10. The large values of the activation parameters measured for high-angle tilt and twist grain boundaries are attributed to a cooperative motion of atoms (group mechanism) during boundary relaxation and are explained by application of the CM.

3.2.6.10 Conformational Transition Energy Barrier of Polymers

This subject already has been touched upon in Section 3.2.5.2 and results are shown in Tables 3.4–3.6. For polymers with low T_g such as PE and PDMS, the primitive activation energy E_a, which is the conformational transition energy barrier in this case, can be obtained from the measured activation energies E_η and E_D of viscosity η and self-diffusion coefficient D by the relations $E_a = (1 - n_\eta)E_\eta$ and $E_a = (1 - n_D)E_D$, respectively The success has been demonstrated before. The value of E_a obtained is supported by measurements of the local segmental relaxation in (1) PDMS by neutron scattering [1579, 1580], (2) PE by ^{13}C-NMR measurements [1582] and molecular dynamics simulations [1581], and (3) aPP by molecular dynamics simulations [1585].

3.2.7 Changes Effected by Mixing or Interfacing

Shown in Section 2.2.5.7 are many examples from experiments and molecular dynamics simulations of the many-body structural relaxation of glassformers being modified by mixing with another glassformer, and in Section 2.3.2.38 by the interfacing with another glassformer or confining immobile solid wall. In this section, analogues of the changes in properties found for structural relaxation in glassformers on mixing or interfacing found in entirely different processes and/or systems are presented. These are other examples of universal dynamics of relaxation and diffusion in interacting systems.

3.2.7.1 Global Chain Dynamics of Each Component in Binary Polymer Blends

In the binary mixtures of glassformers, each component has its own structural α-relaxation and temperature dependence of its relaxation time. Both the relaxation time and the width of the dispersion of the more mobile or faster component increase with increasing concentration of the less mobile or slower component. These changes have been explained by enhancement of intermolecular coupling of the faster component when it is replaced in part by the slower component. In the context of the CM, enhancement of intermolecular coupling is equivalent to increase in the coupling parameter n_α, from which several predictions in agreement with experiments follow including the increased separation between the α-relaxation and the JG β-relaxation. On the other hand, the relaxation time of the slower component decreases on addition of the faster component. For polymeric glassformers, examples discussed before are local segmental α-relaxation in blends of PVME with PS (see Fig. 166), PEO with PMMA (see Fig. 157), and LB-PBD with CR-PBD (see Fig. 170). Here we show analogues of these properties of local segmental α-relaxation from polymer *chain* relaxation in binary miscible polymer blends.

A new rheo-optical technique to measure dynamic infrared dichroism was invented by Fuller and applied to binary polymer blends [1661]. The technique was able to measure not only the total relaxation modulus from global chain motion but also the contribution of each component in a bidisperse entangled polymer melt. The bulk relaxation is measured simultaneously by using birefringence. The first family of blends studied is nearly monodisperse pairs of hydrogenated and deuterated polyisoprenes of molecular weights 53,000 and 370,000, both several times the entanglement molecular weight [1661]. This study was repeated with binary blends of nearly monodisperse poly(ethylene propylene) (PEP) samples of molecular weights 53 K, 125 K, and 370 K, all above the critical molecular weight for entanglement. The results of both studies are similar, and shown in Fig. 306-3 is the relaxation dynamics of each of the two components of the blends of 53 K PEP with 370 K PEP together with the components in their pure state. The blends have compositions of $\Phi_L = 75$, 50, 30, 20, and 10% by volume of the longer chains.

It can be seen by comparing the left panel for the longer chains and right panel for the shorter chains that the global chain dynamics of the two components is different in all blends. The long-chain relaxation is significantly altered by the addition of short chains to the surrounding matrix, as had been inferred from dynamic mechanical relaxation measurement of bulk polymer [1663, 1664]. The dichroism relaxation of the long chains presented in the left panel of Fig. 306 directly shows the change to faster relaxation and narrower dispersion monotonically on increasing the volume fraction of the short chains. Another observation is that increasing presence of long chains in the blend produces a significant retardation of the relaxation of the short chains, accompanied by broadening of the dispersion (see right panel of Fig. 306). All these changes of the *global* chain relaxation properties individually of the long and short chains are analogous to those found in structural relaxation of glassformers. This serves as another example of universal properties of interacting

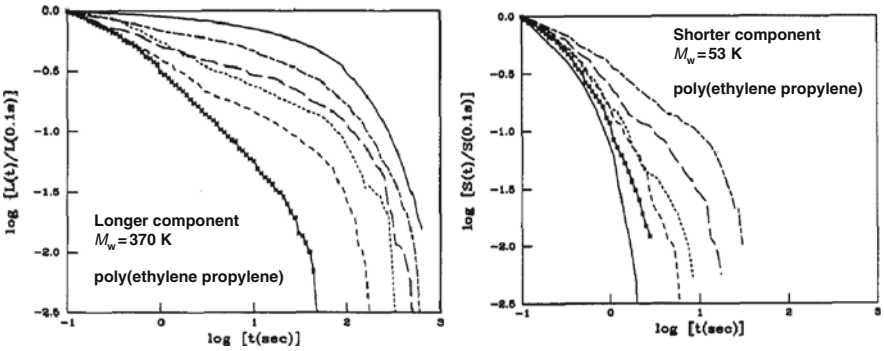

Fig. 306-3 (*Left*) Long-chain dichroism relaxation following a step strain for the S/L blends, where S and L stand for shorter and longer nearly monodisperse poly(ethylene propylene) chains with molecular weights of 53 K and 370 K, respectively. From right to left are data of long chain in the order of 100, 75, 50, 30, 20, and 10% by volume of the longer chains. (*Right*) Short-chain dichroism relaxation following a step strain for the S/L blends. From left to right are data of short chain in the order of 100, 75, 50, 30, 20, and 10% by volume of the shorter chains. Reproduced from [1662] by permission

systems. For the present case, the interaction between polymer chains of the two components comes from the entanglements as well as the short-range or nematic-like orientational coupling between the polymer chains of the two components. The nematic-like orientational coupling was known to many authors [1665–1675], and existence of such interaction has been established in the study of stress optical coefficients for rubbers [1676, 1677] before the dichroism relaxation studies of the blends published in 1989 [1661]. The effect of the "nematic interaction" is to force neighboring polymer segments to orient in the same direction. One of clearest evidence of nematic-like orientational coupling comes from deuterium nuclear magnetic resonance study [1674] of short probe polymer chains dissolved in a strained elastomer. The data showed the presence of imposed orientational anisotropy of the probe chain at very short length scales of the bond level.

Explanation from the CM

The CM applied to global chain dynamics of entangled polymers [202, 203, 359, 360, 837, 870, 872, 904] readily explains the observed changes of global chain dynamics in the blends from the decrease and increase in the entanglement coupling parameters n_L and n_S of the long and short chains respectively as follows. Short chains cannot entangle the long chains as well as long chains themselves, and hence entanglement coupling is decreased by the addition of short chains. This, together with faster motion of the short chains, should reduce the entanglement coupling and its parameter $n_L(\Phi_L)$ of the long chains in the blends by adding short chains. The CM equation, the counterpart of Eq. (3.33), for the long chains is

$$\tau_L(\Phi_L, T) = [t_c^{-n_L(\Phi_L)} \tau_{0L}(\Phi_L, T)]^{1/(1-n_L(\Phi_L))}, \tag{3.46}$$

with $t_c \approx 1$ ns for entanglement coupling (see Fig. 289). This equation together with the monotonic decrease of $n_L(\Phi_L)$ with decrease in Φ_L readily explains the changes of the dynamics of the long chains shown in Fig. 306. On the other hand, the long chains replacing short chains have much longer relaxation time. Hence, the unrelaxed modes of the long chains impose stronger constraint on the short chains, effectively enhancing the entanglement coupling parameter $n_S(\Phi_L)$. In more technical terms, the unrelaxed long chains in the blend enforce sustained orientation anisotropy on the level of Rouse segments of the short chains at times past $\tau_s(\Phi_L = 0, T)$, the global chain relaxation time of the short chains without the addition of long chains. The sustained orientation anisotropy result in prolonged relaxation of the short chains in the blend and relaxation time $\tau_S(\Phi_L, T)$ longer than $\tau_S\,(\Phi_L = 0, T)$. This effect of the long chains on the short chains originates from the short-range or nematic-like orientational coupling between polymer chains in the melt [1665–1675]. This intermolecular orientational coupling interaction between the unrelaxed long chains and the short chains is the cause of the increase of $n_S(\Phi_L)$ with increase of Φ_L in the CM description. A CM expression for $\tau_S(\Phi_L, T)$ similar to Eq. (3.46) predicts the increase of $\tau_S(\Phi_L, T)$ with increasing Φ_L.

Explanation from the Reptation-Based Model After Incorporating Nematic-Like Coupling

The component global chain dynamics found by dichroism relaxation studies of the entangled blends [1661, 1662] cannot be explained by various models which incorporate the effects of constraint release into a reptation-based model [43, 1678–1681]. An example is the strong retardation of the relaxation of the short chains with increasing Φ_L. These reptation-based models predict that the time required for a short chain to completely diffuse out from the initial "tube" of constraints imposed by the mean field just after the strain is applied should be the same for all Φ_L. This prediction is at odds with experiment as can be seen from the left panel of Fig. 306 that the measurable relaxation of the short chains in the blend with 75 vol.% long chains takes place at times more than an order of magnitude longer than those of the monodisperse short chains. Another experimental observation at variance with the reptation-based models is the terminal long-chain relaxation appearing to become single exponential with a long relaxation time for long-chain volume fractions Φ_L less than 0.5, which decreases as Φ_L decreases [1661]. In order to reconcile the dichroism relaxation of the entangled blends [1661, 1662] with the reptation-based model, Doi et al. [1682] pointed out that nematic interaction has to be incorporated into the model. This was implemented by Ylitalo et al. on top of the reptation with constraint release model of Rubinstein–Helfand–Pearson (RHP) [1678]. The RHP model describes the stress relaxation of a blend as the result of two independent mechanisms: reptation, by which the stressed chain disengages from the deformed tube, and constraint release, by which the deformed tube relaxes. With the addition of the short-range nematic interaction, the decorated reptation model can explain the data.

Difference in Spirit of the Explanations by the CM and the Reptation–Constraint Release–Nematic Interaction

It is instructive to point out the difference in spirit of the explanation of the global chain dynamics of entangled blends [1661, 1662] by the CM and the reptation–constraint release–nematic interaction model [1662]. The CM emphasizes that the global chain dynamics of entangled blends is analogous to similar results of component structural relaxation of mixtures of two glass-forming liquids. For the global chain dynamics of entangled blends, the interactions, including long-range entanglement and short-range intermolecular orientation coupling, are different from the Lennard–Jones-like interaction between repeat units in structural relaxation of polymers. Nevertheless, both are genuine many-body relaxation in interacting systems that exhibit similar dynamic properties governed by the same physics and laws. Although the CM equations are used in the explanation given here, these can be replaced by those from a more sophisticated and rigorous theory of universal relaxation of interacting systems when it appears in the future. This spirit of the CM explanation is in stark contrast to the explanation given by the reptation–constraint release–nematic interaction model. The reptation model itself, without the other mechanisms added, considered that the entangled polymer chain dynamics observed including the $M^{3.4}$ dependence of viscosity is the consequence of the topology of long linear chains and the fact that neighboring chains cannot cross. The model views each polymer chain confined by neighboring chains in a tube-like region with diameter equal to the average distance between entanglements. This tube limits the lateral motion of the chain but allows its curvilinear diffusion along its mean contour or its reptation [41–44]. Each linear chain moves like a slithering snake, basically independent of other chains. Thus, the reptation model emphasizes that the particular geometry of entangled thread-like polymer chains is the principal cause of the observed dynamics. Obviously it does not apply to other many-body relaxation processes in other interacting systems, and not even the structural relaxation in the *same* polymer. Cyclic polymers have no ends and cannot reptate, but yet the viscoelastic and diffusion properties of entangled cyclic polymers are essentially the same as linear polymers including similar molecular weight dependence. Actually the reptation model has used the geometric argument to reduce the many-chain relaxation problem to a one-chain relaxation (reptation motion) problem, which provides immediate answers to be compared with experiments [42, 44] including the time dependence of the end-to-end vector correlation function $\phi_e(t)$ given by

$$\phi_e(t) = < R_e(t) \cdot \boldsymbol{R}_e(0) > / < \boldsymbol{R}_e(0)^2 \geq \sum_{p=1,odd}^{\infty} \left(\frac{8}{p^2 \pi^2} \right) \exp \left(-\frac{p^2 t}{\tau_d} \right). \quad (3.47)$$

where τ_d is the disentanglement time of the reptation-tube model. Remarkably, this expression for $\phi_e(t)$ is the same for the Rouse model, except that τ_d is to be replaced by the Rouse time τ_R. The dispersion predicted by Eq. (3.47) of the pure reptation model is too narrow and cannot explain the terminal frequency dispersion of

monodisperse linear polymers in the dynamic modulus or creep experiment measurements. This, together with other problems including $\tau_d \propto M^{3.0}$ and not the observed $M^{3.4}$ dependence of viscosity, has led to the addition of the new mechanism of constraint release to the reptation model [43, 1678–1681] in order to bring consistency with experiment. The constraint release mechanism is due to the motion of neighboring chains that form the fixed tube of the original reptation model and has the flavor of many-chain dynamics. However, it is implemented as a correction of the chain reptative motion independent of the other chains. The reptation–constraint release model still is leaning heavily on the premise that each linear chain moves like a slithering snake, and therefore it is far from solving the problem by treating it as relaxation of many chains interacting by entanglements. Basically the problem of all reptation-based models is that they have accepted from the start that the chain motion is reptation and its predictions, and corrections are made by adding new mechanisms such as constraint release or tube renewal to bring consistency of the model with experiment in monodisperse polymers [43, 1678–1681]. The component chain dynamics of bidisperse entangled polymer blends discussed here [1661, 1662] requires another correction of including nematic interaction, leading ultimately to the reptation–constraint release–nematic interaction model. The deviation of the center-of-mass MSD data from neutron spin echo experiments by Zamponi et al. [1503] from the reptation prediction (see Fig. 281) would require another correction. Instead of correction after correction on the reptation motion, it may be worthwhile to restart anew to solve the problem as a many-chain relaxation problem, without jumping to reptation but taking into account of the limited lateral motion of thread-like molecules. Although the CM does not describe the lateral constraints as elaborately as done in the tube model [42, 44], lateral constraints and their mitigation have been considered in an attempt to rationalize the experimental results of monodisperse polymers in [837], and the component dynamics of bidisperse entangled blends here.

3.2.7.2 Other Examples of Change of Global Chain Dynamics of Entangled Polymers by Mixing

Plasticized Poly(Cyclohexy1 Methacrylate)

Polarized photon correlation measurements of high molecular weight, entangled neat and plasticized poly(cyclohexyl methacrylate) (PCHMA) by dioctyl phthalate (DOP) were able to observe both the density fluctuations caused by the local segmental relaxation and concentration fluctuations due to cooperative diffusion of chain diffusion [203]. The plasticized PCHMA contain $\Phi_{DOP} = 5,\ 10$, and 15 wt% DOP. Over a common temperature range, the data show that the local segmental relaxation time exhibits a stronger temperature dependence than does chain diffusion, a result which is consistent with the breakdown of thermorheological simplicity of polymers observed before by mechanical spectroscopy [165–171]. The other observation relevant in the present context is the time correlation function of entangled chain diffusion narrows on increasing the content of DOP in the mixture.

The trend indicates a decrease of the entanglement coupling parameter. The narrowing of the dispersion on increasing weight percentage of DOP in the plasticized PCHMA is accompanied by the observation of a weaker $(T - T_g)$ dependence of the chain diffusion relaxation time. Following the CM relation similar to Eq. (3.46), this trend corroborates the decrease of entanglement coupling parameter, which in turn is caused by the decrease in chain entanglement interaction by the presence of the plasticizer to separate the chains further apart.

Dilute Polyisoprene Probes in Networks

Adachi and coworkers [1685] studied the dielectric normal mode relaxation of nearly monodisperse PI trapped in cross-linked natural rubber networks [1684] and in PB networks. The experimental data were reviewed by Adachi and Kotaka [1686, 1687]. The PB networks used were loosely cross-linked with the molecular weight between cross-links $M_x > M_e$, where M_e is the molecular weight between entanglements. The dielectric relaxation loss curve $\varepsilon''(\omega)$ is broader than that of pure bulk monodisperse entangled PI. The experimental data of 14 K-PI trapped in a PB network labeled BR(0.1:20) are shown in Fig. 307 (filled circles). In the same figure the solid curve represents the $\varepsilon''(\omega)$ calculated by the CM with the entanglement coupling parameter n equal to 0.45 [837]. This value of n is determined by Eq. (3.32) from the observed $(M_{PI})^{3.6}$ dependence of the dielectric relaxation time of the PI chains. The dielectric loss peak in Fig. 307 is significantly broader than the loss peak of pure monodisperse PI melt, and the relaxation time of the former is much longer than the latter. These changes of PI when introduced into PB network are similar to those experienced by the short chains when long chains are present in the bidisperse entangled polymer blends studied by Fuller and coworkers [1661, 1662].

3.2.7.3 Mixed Alkali Effect in Ionic Conductors

The "mixed-alkali (MA) effect" refers to deviation from linear additivity in isotherms of several dynamic properties of ions in alkali oxide glasses as one kind of alkali ion is replaced by another kind [1689–1692]. For example, it is

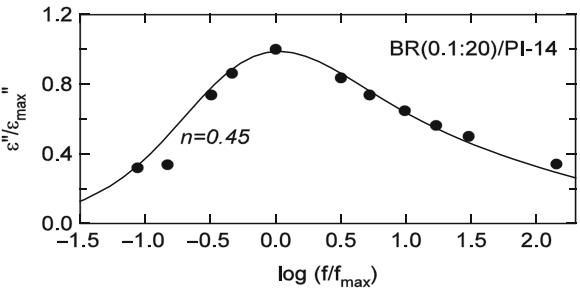

Fig. 307 Normalized $\varepsilon''(\omega)$ data of free PI chains with $M_{PI} = 13,500$ trapped in loosely cross-linked polybutadiene network with $M_x = 11,000$ (*solid circles*). Normalized $\varepsilon''(\omega)$ curve calculated with $n = 0.45$ by the CM. Reproduced from [837] by permission

frequently observed that the electrical conductivity σ of a single alkali ion glass rapidly decreases when a small amount of the alkali A is replaced by alkali B. A similar effect occurs on the other composition extreme with the roles of A and B interchanged, giving rise in many cases to a deep minimum in σ at some intermediate composition. The left panel of Fig. 308 shows the MA effect on the dc conductivity of the $0.2[x\mathrm{Na_2O}–(1–x)\mathrm{Rb_2O}]–0.8\mathrm{B_2O_3}$ mixed-alkali borate glasses with x= 0.0, 0.2, 0.4, 0.6, 0.8. The right panel shows tracer diffusion coefficients of ^{22}Na and ^{86}Rb at 653 K in these glasses. The data come from the work of Imre et al. [1693], and similar results had been obtained by Jain et al. [1694].

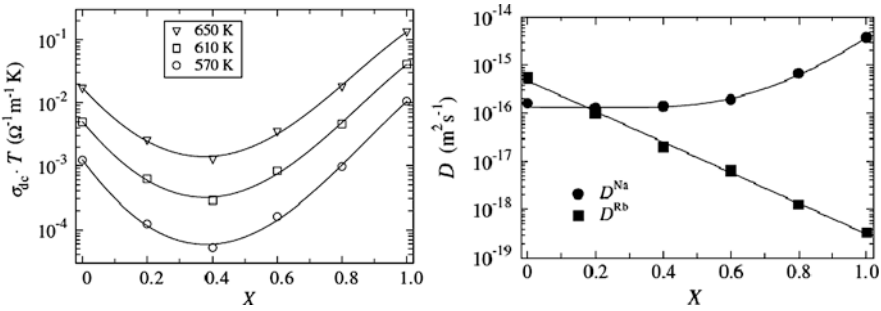

Fig. 308 (*Left*) Isotherms of the product $\sigma_{dc}T$ of $0.2[x\mathrm{Na_2O}–(1–x)\mathrm{Rb_2O}]–0.8\mathrm{B_2O_3}$ glasses for three temperatures. (*Right*) Composition dependence of the tracer diffusion coefficients of ^{22}Na and ^{86}Rb at 653 K in these glasses at 653 K. Reproduced from [1693] by permission

The effect turns out to be more general and has been found in glasses with other mobile non-alkali monovalent cations and anions (such as $F^–$) and in crystalline ionic conductors (such as alkali β-alumina). Various experimental techniques have shown that the local environments of the two different alkali ions in the MA glasses are different [1695–1700]. The alkalis retain more or less the same local environment as in the respective single alkali (SA) glasses, and they are randomly distributed in the glass structure. Since there is a large difference between the sites for the two alkali ions with large differences in their site energies [1701, 1702], jumps of an alkali ion to the sites of a different alkali ion cannot occur. This implies that ions of one kind tend to block the pathways for the other kind of ions and vice versa, as found out also by reverse Monte Carlo method [1703]. It follows that there are fewer sites for ionic motion of the more mobile alkali species when some of them are replaced by the less mobile alkali species, and these fewer sites are more separated in space. This is one of the main causes of the MA effect. The other is the immobilization or the reduction of mobility of ions of one kind by the presence of relatively immobile ions of the other kind [1704, 1705]. Both effects lead to decrease in the number of mobile ions and increase in their average distance of separation, resulting in diminishing ion–ion interaction and correlation. The situation can be likened to the effect found on the reduction of ion concentration in single alkali glasses, where it is well known that reduction of ion concentration

increases the activation energy of conductivity due to lower level of cooperativity between ions [115, 1706]. Thus the MA effect, when considered in terms of the change in activation enthalpy and isothermal conductivity, can be qualitatively understood by its similarity to the effect of decreasing the alkali ion concentration of an SA glass, a suggestion that was made earlier by Greaves and Ngai [1706(b)]. The reduction of cooperativity or the degree of many-ion dynamics of ions by the presence of immobile ions of another kind is observed by molecular dynamics simulation [1707]. More recent results that enhance understanding of the MA effect come from molecular dynamics simulations [1707–1711] and experiments [1693, 1711], some of which will be further discussed.

Consistent with the purpose of this chapter of showing universal relaxation and diffusion properties on interacting systems presented here are some of those experimental facts and simulation results of MA effect that either support the importance of ion–ion interaction or show analogous properties in other interacting systems.

Mixed Alkali Effect in the Dilute Foreign Alkali Regime Requires Ion–Ion Interaction for Explanation

The derivative $(\partial \ln \sigma_{dc}/\partial x)$ is a measure of how rapid the conductivity changes with replacement of the majority ions. Here x is the fraction of the majority ions and $(1–x)$ the fraction of the minority ions. The most rapid change measured by the largest value of $(\partial \log \sigma_{dc}/\partial x)$ occurs at $x = 1$, i.e., the dilute limit of the foreign alkali region. This very rapid decrease in σ_{dc} by replacement of the host alkali ions by a small amount of foreign alkali ions indicates that many host ions suffer large decreases of mobility (or are immobilized) per single foreign alkali ion introduced. Such a very large number Z of host alkali ions immobilized by a foreign alkali ion was deduced from the experimental values of the limiting rate of change of σ_{dc} with the host ion fraction x, $\lim_{x\to 1}(\partial \ln \sigma_{dc}/\partial x)$, by Moynihan et al. [1693], assuming that the single alkali (SA) silicate glass they studied was a strong electrolyte. Z increases with decreasing temperature and reaches values of order of around 50 at the lowest temperature studied. However, at that time it was difficult for Moynihan et al. to understand how a single foreign alkali can immobilize so many host alkali ions. In fact, this puzzling result led Moynihan et al. to conclude that it was unacceptable and that the faulty result originated from the assumption that the SA glass is a strong electrolyte. However, very recent NMR chemical shift measurements of MA glasses by Eckert [1712] have confirmed that indeed many host alkali ions are affected by every single foreign ion. Thus, it appears to be true that a single foreign alkali ion can immobilize a large number of host alkali ions. Furthermore, we have confirmation from molecular dynamics simulations of diffusion of Li ions in Li_2SiO_3, where a small proportion of Li ions randomly chosen were frozen, and also of Li in $(Li_{1-x}K_x)2SiO_3$ with small x [1707]. This is an important experimental fact, because it can be used to rule out immediately some current models of the MA effect by showing that in the dilute foreign alkali region the models do not predict a large number of host ions being immobilized by a single foreign ion.

An explanation of largest value of $(\partial \log \sigma_{dc}/\partial x)$ occurs in the dilute limit of the foreign alkali region was provided [1705] by drawing the analogy to the simulation results of mobile particles confined by walls formed by immobile particles [322, 1463]. All immobile and mobile particles interact with each other by the same Lennard–Jones potential, and the effects of immobile particles on the mobile particles are obtained from the simulation. The immobile or frozen particles were made to form a "wall," and the effects that the immobile particles have on the dynamics of the mobile particles at any distance z away from the wall were obtained from the spatially resolved self-part of the intermediate scattering function $F_s(z, t)$ with wave vector at the maximum in the static structure factor. The results have been discussed before in Section 2.3.2.38 and results shown in Fig. 265. Particles in the layer closest to the wall (smallest z) have their relaxation time increased by orders of magnitude. The immense slowing down of the particles by the immobile particles does not stop at the first layer at the interface. From Fig. 265 one can see that the effect propagates to the next layer and so on, although the increase of relaxation time becomes less with increasing distance away from the wall. The immobilizing effect of the immobile wall particles on the initially (before the wall is introduced) mobile particles is not limited to the immediate layer but propagates further away to affect more layers.

In the MA glass in the dilute foreign alkali limit, the foreign alkali has mobility orders of magnitude smaller than the host ions (see right panel of Fig. 308 for the case that Rb is the foreign ion in $0.2\,[x\mathrm{Na_2O} - (1-x)\mathrm{Rb_2O}] - 0.8\mathrm{B_2O_3}$, and there is interaction between the Rb ion and the host Na ions. Thus, if this result from Lennard–Jones liquid can be used as an indication of the effect that an immobile foreign alkali ion can have on the dynamics of the initially mobile host ions, we are led to conclude that not just the five or six nearest neighbor host alkali ions will be severely immobilized by the foreign alkali ion but also second nearest neighbor host alkali ions will be immobilized, although to a lesser extent, and so on. The immobilizing effect propagates and dies off with distance away from the foreign alkali ion. It is now conceivable in the glasses of composition $0.242\,[x\mathrm{K_2O} + (1-x)\mathrm{Na_2O}] - 0.758\mathrm{SiO_2}$ studied by Moynihan et al. [1693] in the dilute Na^+ ion composition range that an Na^+ ion can effectively immobilize 48 K^+ ions, as the data at 25°C of the value of $\lim_{x\to 1}(\partial \ln\ \sigma/\partial x)$ require, under the assumption that the alkali silicate glass is a strong electrolyte. The early work [1693] did not have the benefit of recent progress in the knowledge of the change in dynamics of interacting systems, but only the crude concept of immobile complexes of alkali composition NaK_Z. This large number Z of K^+ ions immobilized by an Na^+ ion required by the data at 25°C was considered inconceivable in the framework of this crude concept and led Moynihan et al. to fault the assumption that the alkali silicate glasses are strong electrolytes [1693]. However, in the intervening years and at the present time, the structural and dynamic studies of alkali oxide glasses seem to show that they are indeed strong electrolytes. Now, with the justification that the large Z is reasonable when ion–ion interactions are taken into account, the data at 25°C can be rationalized without rejecting the presumption that alkali silicate glasses are strong electrolytes.

The dynamics of L–J particles confined by walls made of immobile L–J particles show interesting temperature dependence. The large increase of relaxation time compared to the bulk was shown before at a low temperature in Fig. 265, but the increase diminishes rapidly with increasing temperature. In the inset of Fig. 309, the ratio of the relaxation times τ of particles at $z = 0.8$ close to the wall to that at $z = 7.5$ at the center of the confined liquid is plotted as a function of temperature. The data are taken again from [1463]. It can be seen that the ratio $\tau(z = 0.8)/\tau(z = 7.5)$ decreases rapidly with temperature. Thus, the degree of immobilization caused by the frozen particles in the wall decreases with increasing temperature. When this temperature dependence of immobilization is applied to the mixed alkali effect, the observed decrease of $\lim_{x\to 1}(\partial \ln \sigma/\partial x)$ or the corresponding Z with temperature [1693] as shown in Fig. 309 can be rationalized by the same explanation as given before for the confined L–J liquid [900].

The discussion of the results above serves the purpose of highlighting the importance of ion–ion correlation/interaction in considering the MA effect. Maass [1713]

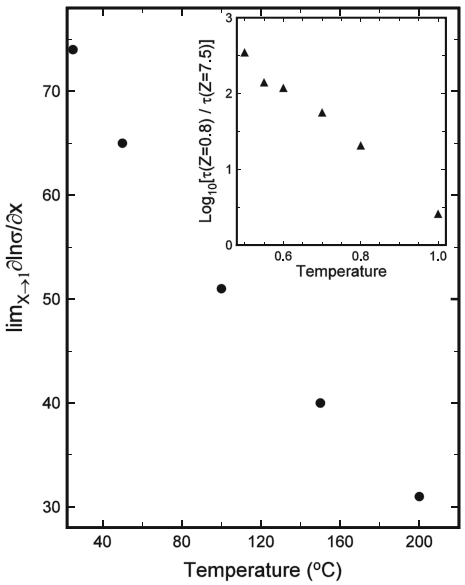

Fig. 309 Temperature dependence of the limiting slopes $\lim_{x\to 1}(\partial \ln \sigma/\partial x)$ of $\ln\sigma$ vs. x isotherms obtained for $0.242[xK_2O + (1 - x)Na_2O] - 0.758SiO_2$ glasses by Moynihan et al. [1693] in the dilute Na^+ ion composition range. This quantity, an indication of how many host K^+ ions are immobilized by a single foreign Na^+ ion, is a decreasing function of temperature. The *inset* shows ratio of the relaxation time $\tau(z = 0.8)$ of particles in the L–J liquid located at $z = 0.8$ close to the frozen L–J glass forming the wall to $\tau(z = 7.5)$ far from the wall. The ratio, an indication of the extent of the immobilization of particles in the L–J liquid, is also a decreasing function of temperature like $\lim_{x\to 1}(\partial \ln \sigma/\partial x)$ in the main figure. Results in the *inset* are obtained from data of molecular dynamics simulation result of Schneider et al. [322, 1463] on $F_s(z, t)$ and shown in Fig. 265. Reproduced from [1705] by permission

had called attention to interaction between the moving ions in considering the MA effect, although for a different reason than we discussed here. Swenson et al. also mention this point made by Maass in their work [1714]. Ion–ion correlation certainly plays an important role in determining the ionic conductivity and its frequency dispersion in SA glasses, as indicated by various experimental facts discussed in Sections 3.2.2–3.2.6 and incorporated into the coupling model.

Immobilization of Li Ions by Frozen Li Ions in the Confining Walls

The immobilization of more mobile ions by less mobile ions in the MA effect has been rationalized by analogy to similar effect found in L–J particles confined by frozen L–J particles forming the walls. To demonstrate the physics of two systems closer, a molecular dynamics simulation was made on the dynamics of Li ions in Li_2SiO_3 glass confined by parallel walls formed by the same glass except that the Li ions therein were frozen but still interacting with the Li ion in the confined Li_2SiO_3 glass [1707]. The geometry of the systems is illustrated in the left panel of Fig. 310. The self-part of the density–density correlation function $F_s(k,t;z)$ was obtained at any distance z from the wall for Li ions located at $z \leq 0$. The unit of z is $L/10$, where L is the side length of the basic cell of the simulation. The $F_s(k,t;z)$ obtained has the Kohlrausch stretched exponential time dependence $\exp[-(t/\tau(k;z))]^{\beta(k,z)}$. The frozen Li ions in the walls cause slowing down of Li ion as seen by the increase of $\tau(k;z)$ in the middle panel of Fig. 310 and the concomitant increase in stretching of $F_s(k,t;\ z)$ as seen by the decrease of $\beta(k;z)$ in the right panel for two chosen values of $k = 2\pi/10$ and $2\pi/3$. The effect is largest for the Li ions closest to the wall and decreases monotonically with distance from the wall. The values of $\tau(k,z)$ for Li ions residing in the innermost $z=5$ region are close to those for the unmodified bulk Li_2SiO_3 glass, which are $\tau(k) = 1292$ ps for $k = 2\pi/10$ and 340 ps for $k = 2\pi/3$. Values of $\beta(k;z)$ in the innermost $z=5$ region are also close to those

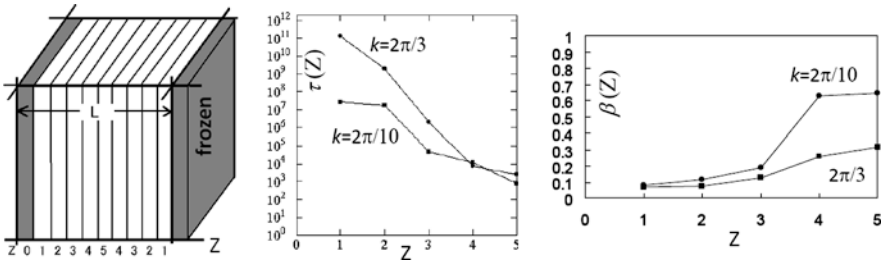

Fig. 310 (*Left*) Li metasilicate glass confined by two walls of the same Li metasilicate glass except that the Li ions therein are frozen. (*Middle*) Plot of $\tau(z)$ against z for the stretched exponential region of $F_s(k,t)$ of Li ions in Li_2SiO_3 glass (in ps). *Filled circle*: $k = 2\pi/10$. *Filled square*: $k = 2\pi/3$. (*Right*) $\beta(z)$ against z for the stretched exponential region of $F_s(k,t)$ of Li ions. *Filled circle*: $k = 2\pi/10$. *Filled square*: $k = 2\pi/3$. The values of $\beta(z)$ in the z=5 region are close to the values for the bulk Li_2SiO_3, which are $\beta = 0.67$ and 0.32 for $k = 2\pi/10$ and $2\pi/3$, respectively. Data from [1707] are replotted in all figures here

for the unmodified bulk system, which are $\beta(k) = 0.67$ for $k = 2\pi/10$ and 0.32 for $k = 2\pi/3$. The changes in the dynamics of Li ions interacting with the frozen Li ions in the confining walls are exact analogues of the L–J particles confined by frozen L–J particles in the confining walls obtained by Scheidler et al. [322, 1463]. This becomes obvious when comparing the dependence of $\tau(k;z)$ and $\beta(k;z)$ on distance from the wall in Fig. 310 with that of the same quantities for the confined L–J particles in Fig. 265. Thus, this is another example of universal behavior of relaxation in interacting systems.

Additional Evidence of Immobilization of Ions and Reduction of Ion–Ion Interaction of Mobile Ions in MA Effect

In MA glasses there are two kinds of ions and even the more mobile kind has some immobilized, less mobile, and more mobile ions. The electric modulus representation is known to suppress low-frequency contributions, not only from the electrode polarization but also from the less mobile and the immobile ions in the MA glasses. The story is different, however, when the same MA data are shown in the $\varepsilon^*(f)$ or the complex impedance Z^* vs. $\log f$ representation. In these representations of the data, the low-frequency contributions from less mobile and immobile ions are emphasized and show up prominently as large deviations from the prediction of the Kohlrausch relaxation at low frequencies well below the frequency maximum in the M'' vs. $\log f$ plot. The large deviations from Kohlrausch relaxation were first seen in the complex impedance plots of Z'' vs. Z' of MA glasses and later at lower frequencies in $\varepsilon'(f)$, the real part of $\varepsilon^*(f)$. Whereas Z'' vs. Z' plots of actual data for the single alkali glasses or Z'' vs. Z' curves predicted by the Kohlrausch fit to the SA glass electric modulus data display approximately the shape of a submerged semicircle, the data for MA glasses show large deviations from this shape. This deviation was pointed out by Moynihan and Boesch [1716] and by Tomozawa and coworkers [1717, 1718]. Tomozawa and coworkers further showed enormous differences between SA and MA glasses in $\varepsilon'(f)$ and $Z^*(f)$ at low frequencies by comparing the data of Li_2O–$2SiO_2$ and [$0.5Na_2O$+$0.5LiO_2$]–$2SiO_2$ glasses. The dielectric relaxation strength $(\varepsilon_s - \varepsilon_\infty)$ of the MA glass is much higher than that of the SA glass, suggesting the presence of an additional relaxation contribution in MA glasses at lower frequencies, over and above the normal conductivity relaxation from mobile ions. They showed that this additional relaxation was responsible for the large value of $\varepsilon'(f)$ in MA glasses at low frequencies and corresponded to a large polarization contributed by ions of low mobility, which are the alkali ions immobilized to various degrees in the neighborhoods of the other kind alkali ions discussed above.

Therefore, when shown as $\varepsilon'(f)$ vs. $\log f$, the data of MA glasses support the presence of contributions to polarization from immobilized or partially immobilized alkali ions that are not accounted for by the electric modulus $M^*(f)$ due to its suppression of the low-frequency polarizations from the immobilized or partially immobilized ions. In effect, by showing the data as $M^*(f)$ one has selected only the faster dielectric response of the mobile ions in the MA glass. Kohlrausch fit to the $M^*(f)$ data of MA glasses is often found to be successful, but the Kohlrausch

exponent β of the fit merely reflects the width of the dispersion because of contributions from ions with different mobility. The frequency dispersion of $M^*(f)$ data of MA glasses is narrower than the parent single alkali glasses as found in experiments by many workers [1704, 1717, 1719–1725]. This can be considered as evidence for the reduced ion–ion interaction due to fewer mobile ions and wider separations between them in the MA glasses mentioned before. An example is shown in the left and middle panels of Fig. 311 by the variation of the Kohlrausch exponent β with x from fits using the Kohlrausch function to the electric modulus of the alkali silicate glasses $[xK_2O + (1-x)Na_2O] - 3SiO_2$. Here β for all x are obtained from electric modulus data that have nearly constant values of τ (within a factor 2 of 3×10^{-3} s). The data show that β increases or the dispersion narrows with increasing amounts of foreign alkali in the dilute foreign-alkali region, leading to a maximum in β at an intermediate composition close to the minimum of dc conductivity. The same was found by Karlsson et al. in mixed alkali $Li_xRb_{1-x}PO_3$ glasses [1725], and they also consider this as indicating that the mixed alkali glasses behave as single alkali glasses of effectively lower concentrations. Another example in the right panel of Fig. 311 shows the narrower loss modulus $M''(f)$ data of the MA glass, $0.242[xK_2O+(1-x)Na_2O]-0.758SiO_2$ with $x = 0.950$, in the dilute Na^+ ion composition range compared with the parent SA with $x = 1.00$ studied by Moynihan et al. [1693].

Decrease of the Strength of MA Effect with Increase in Ion–Ion Distance

If ion–ion interaction/correlation is an important element in determining the MA effect, then a natural consequence is that the MA effect should go away on

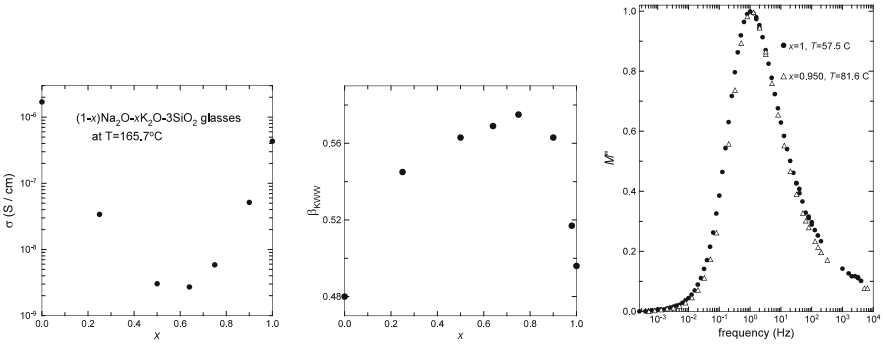

Fig. 311 (*Left*) The variation of the dc conductivity with x for the alkali silicate glasses $[xK_2O + (1-x)Na_2O] - 3SiO_2$. Data taken from [1726] and replotted. (*Middle*) The variation of the Kohlrausch exponent β with x from fits using the Kohlrausch function to the electric modulus. Here β for all x is obtained from electric modulus data that have nearly constant values of τ (within a factor 2 of 3×10^{-3} s). The data show that β increases or the dispersion narrows with increasing amounts of foreign Na in the dilute foreign Na region, leading to a maximum in β at an intermediate composition. Data taken from [1726] and replotted. (*Right*) Electric modulus spectra of the MA glass, $0.242[xK_2O + (1-x)Na_2O] - 0.758SiO_2$ with $x = 0.950$, in the dilute Na^+ ion composition range compared with the parent SA with $x = 1.00$ studied by Moynihan et al. [1693]

increasing the mean ion–ion separation distance. Tomozawa et al. [1722, 1727] measured the MA effect in alkali germanate glasses of molar percentage composition $0.019[xK_2O + (1-x)Na_2O] - 99.981GeO_2$ with an extremely low (0.019 mol%) total alkali content for x values of 0, 0.44 and 0.71. Their results at a temperature of 350°C show that the log σ vs. x plot did not exhibit the minimum associated with the MA effect. In glasses with low alkali content there is a negligible effect of ion–ion interaction on the dynamics of ion transport in the SA or the MA cases. After mixing the alkalis, the ions remain far apart, and there is no immobilization of one kind of alkali ions by another kind as supported by the normal semicircular trace of the data in a plot of Z'' vs. Z'. This trend of decreasing magnitude of the MA effect on increasing separation of the ions was verified by Voss et al. [1711] by measurements of a number of Na–Rb alumino-germanate glasses and Na–Rb borate glasses that permit wide range of the values of $< d_{\text{ion}} > / < d_{\text{network}} >$, the average Na–Na distance to the network distance. The left panel of Fig. 312 shows the strength of the mixed-alkali effect Δ_{MAE} as a function of $< d_{\text{ion}} > / < d_{\text{network}} >$.

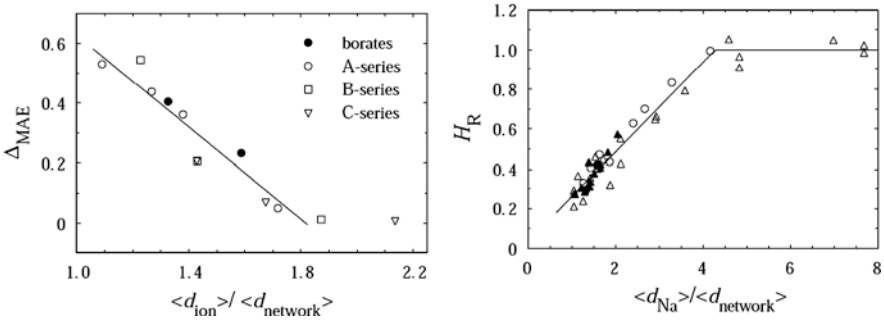

Fig. 312 (*Left*) Strength of the mixed-alkali effect Δ_{MAE} as a function of the average Na–Na distance to the network distance $< d_{\text{ion}} > / < d_{\text{network}} >$. *Open symbols* represent Na–Rb alumino-germanate glasses, whereas the *two filled circles* refer to Na–Rb borate glasses. Reproduced from [1711] by permission. (*Right*) Haven ratio H_{R} as a function of the ratio of the average Na–Na distance to the network distance $< d_{\text{Na}} > / < d_{\text{network}} >$. Values for Na-borate glasses: •, Voss et al. [1715] ($T = 380$°C); ○, Kelly et al. [1728] ($T = 300$°C). Na-alumino-germanate glasses: ▲, from [1711] ($T = 380$°C), Δ, Kelly et al. [1728] ($T = 300$°C). Reproduced from [1711] by permission

3.2.8 Evidence of Ion Transport Governed by Ion–Ion Interaction from Molecular Dynamics Simulation

To further support ion–ion interaction and the many-ion relaxation governing ion transport in glassy ionic conductors, we cite an important observation by Binder [1732(a)] and Horbach et al. [1732(b)] from the results of molecular dynamics simulations on the Na_2O–SiO_2 melt.

From the simulations, Horbach et al. obtained the probability function $P_{\text{Na-Na}}(t)$ that a "bond" that exists between a Na ion and another Na ion at $t = 0$ is also

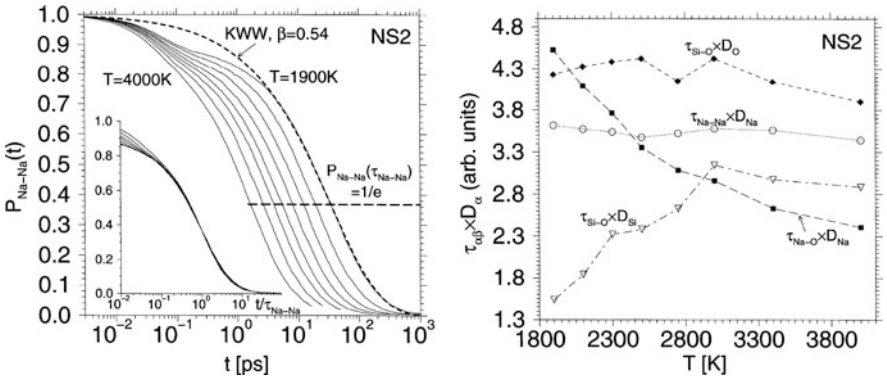

Fig. 313 (*Left*) Time dependence of $P_{\mathrm{Na-Na}}$, the probability that a bond between two sodium atoms which exists at time zero is also present at time t, for all temperatures investigated. *Inset*: plot of the same data vs. the scaled time $t/\tau_{\mathrm{Na-Na}}$, as a function of temperature. (*Right*) Temperature dependence of the products $\tau_{\alpha\beta}D_\alpha$ shows whether or not the diffusion constant D_α is correlated with the lifetime of a bond $\tau_{\alpha\beta}$. Reproduced from [1732(b)] by permission

present at time t. The time dependence of $P_{\mathrm{Na-Na}}(t)$ are shown in the left panel of Fig. 313, together with the fits to the Kohlrausch function having exponent $\beta_{\mathrm{KWW}} = (1 - n) = 0.54$ and relaxation time $\tau_{\mathrm{Na-Na}}$. The two Na ions are considered as "bonded" if their distance is less than $r_{\min}$, the location of the first minimum of the pair distribution function $g_{\mathrm{Na-Na}}(r)$. They also obtained the probability functions $P_{\alpha\beta}(t)$ for other atoms (ions), where α and β range over Na, Si, and O, and the corresponding lifetimes $\tau_{\alpha\beta}$ of the α–β bonds for different temperatures. The lifetimes $\tau_{\alpha\beta}$ can now be correlated with the diffusion constants by plotting different products $\tau_{\alpha\beta}D_\alpha$ vs. temperature, which are shown in the right panel of Fig. 313. The product $\tau_{\mathrm{Na-Na}}D_{\mathrm{Na}}$ is essentially constant over the whole temperature range. Therefore, the sodium diffusion constant seems to be linked to Na–Na "bonds," and the role of Na-Na interaction/correlation in governing Na ion transport is clear.

On the other hand $\tau_{\mathrm{Na-O}}D_{\mathrm{Na}}$ increases with decreasing temperature. This means that the elementary diffusion step for the sodium diffusion is not related to that of a Na–O bond, although the nearest neighbor distance is smaller for $\mathrm{Na-O}(r_{\mathrm{Na-O}} = 2.2\,\mathring{\mathrm{A}})$ than for $\mathrm{Na-Na}\,(r_{\mathrm{Na-O}} = 3.3\,\mathring{\mathrm{A}})$. In other words, Na ion diffusion is decoupled from the silicate matrix.

3.2.9 Haven Ratio, Breakdown of Nernst–Einstein Relation: Analogue of Breakdown of Stokes–Einstein Relation

The breakdown of the Stoke–Einstein relation in molecular glassformers discussed in Section 2.2.5.6 has been considered to be one of the most important and general characteristics by the glass transition research community. It occurs not only in molecular glassformers such as OTP and tri-naphthyl benzene but also in metallic

glasses [812], where the diffusing entities are atoms. An analogue of this anomaly in glass-forming systems can be found in glassy and crystalline ionic conductors by the fact that the self (tracer)-diffusion coefficient D^* and the conductivity diffusion coefficient D_σ are not the same. In glassy single-alkali ionic conductors, D^* is measured by tracer diffusion of an radioactive isotope of the same alkali, and D_σ is calculated from the measured dc conductivity σ_{dc} via the Nernst–Einstein relation $\sigma_{dc} = (Nq^2/k_BT)D_\sigma$ between conductivity and diffusion coefficient that holds for non-interacting systems. Here N is the number density of alkali ions, q the ion charge, k_B the Boltzmann constant, and T the temperature. The experimental fact that D^* is larger than D_σ in many glassy ionic conductors with large concentration of mobile alkali ions is evidence of the breakdown of the Nernst–Einstein relation, which should be $\sigma_{dc} = (Nq^2/k_BT)D^*$. The degree of breakdown is usually indicated by the Haven ratio $H_R = D^*/D_\sigma$, which has values less than equal to one [1490]. The smaller the H_R is, the larger is the breakdown. Since ion–ion interaction and many-ion dynamics have been identified as important in glassy and crystalline ionic conductors containing high concentration of mobile ions, it is natural to consider it as the cause of the breakdown. Simulation of Li ion motion in lithium silicate glasses by Heuer et al. [1728] has also concluded that the inverse of the Haven ratio can be considered as a measure of the degree of "collectivity" in ionic motion.

One way to support this is consistency of the prediction that H_R should increase with decreasing ion–ion interaction strength as can be realized by increasing the average separation between ions. The limit of $H_R = 1$ is reached and Nernst–Einstein relation holds when ion–ion interaction becomes negligible. The equivalent of this in the CM description is the expected increase of H_R with decrease of the coupling parameter n with decreasing ion concentration, where n can be obtained from the fit to the electric modulus data by the Kohlrausch function $\exp\left[-(t/\tau)^{1-n}\right]$. The decrease of n with decreasing ion concentration in the same family of glassy ionic conductors has been verified before in [1706(a), 1721] and in crystalline ionic conductors in [150]. The reader may recall that there is an analogous example in the breakdown of the Stokes–Einstein relation. As mentioned before in Section 2.2.5.6, silica having smaller n than OTP exhibits no breakdown of the Stokes–Einstein relation [822]. For glassy ionic conductors, the support of the ion–ion interaction as the cause of the breakdown of the Nernst–Einstein relation can be drawn from the collection of experimental data of the dependence of H_R on total alkali content of alkali borate, germinate, and silicate glasses by Kelly et al. [1729] and Na alumino-germanate and Na borate glasses by Voss et al. [1711]. Kelly et al. have reported for each family of alkali oxide glass that H_R increases with decreasing total alkali content for alkali borate, germanate, and silicate glasses. Voss et al. combined their Haven ratio data of Na borate and Na alumino-germanate glasses with the data of Kelly et al. and plotted all data of H_R altogether against the ratio of the average Na–Na distance to the network distance $< d_{Na} > / < d_{network} >$. This plot shown here in the right panel of Fig. 312 verifies the expected increase of H_R on increasing ion–ion distance, and the limit $H_R = 1$ is attained at low alkali concentration.

The degree of breakdown of the Stokes–Einstein relation of glassformers increases with decreasing temperature toward T_g (see Section 2.2.5.6). Similar T

dependence of the degree of breakdown of the Nernst–Einstein relation was found by simulation and experiment. Decrease of the Haven ratio with decreasing temperature was found by Knödler et al. [1730] by simulation of a stochastic lattice gas model with ion–ion interaction included into the Hamiltonian and by experimental measurements in a Rb borate glass $0.2Rb_2O–0.8B_2O_3$ [1731] However, H_R of the corresponding Na borate glass $0.2Na_2O–0.8B_2O_3$ shows no temperature dependence.

Explanation of the breakdown of the Stokes–Einstein relation in glassformers given by the CM was based on the correlation functions for center-of-mass diffusion and viscosity which weigh differently the effects of the many-body relaxation, resulting in different coupling parameters and relaxation times. A similar reasoning was given to explain the difference in relaxation times between nuclear spin relaxation and conductivity relaxation of glassy ionic conductors (see Section 3.2.5.1). The origin of the Haven ratio being less than unity in glassy ionics may also be explained by the slight difference between the tracer diffusion correlation function $C_D(t) =< \boldsymbol{r}_i(0)\boldsymbol{r}_i(t) >$ and the conductivity correlation function $C_\sigma(t) = (1/N)\Sigma_{ij} < \boldsymbol{v}_i(0)\boldsymbol{v}_j(t) >$, where $\boldsymbol{r}_i$ and $\boldsymbol{v}_i$ are the position and the velocity of the diffusing ions, respectively. The $i \neq j$ cross-correlation terms in $C_\sigma(t)$ do not appear in the $C_D(t)$.

3.2.9.1 The Haven Ratio for Mixed Alkali Glass

Having shown for single alkali glasses that the Haven ratio H_R anti-correlates with ion–ion interaction and many-ion cooperative dynamics, here the "common" Haven ratios of the mixed alkali glasses $0.2\,[x\mathrm{Na_2O} - (1-x)\mathrm{Rb_2O}] - 0.8\mathrm{B_2O_3}$ obtained by Imre et al. [1693] are used to further support the decrease of ion–ion interaction and many-ion dynamics in the mixed alkali effect.

The common $H_R(x)$ of the mixed alkali glass with composition x is defined by

$$H(x) = \left(\frac{Nq^2}{k_B T \sigma_{dc}(x)}\right)\left[xD^{Na}(x) + (1-x)D^{Rb}(x)\right], \tag{3.48}$$

where D^{Na} and D^{Rb} are the tracer diffusion coefficients of Na and Rb, respectively. The right panel of Fig. 314 shows that H_R increases on introducing foreign alkali into the host, and it peaks at the same composition ($x = 0.4$) as the activation enthalpy ΔH_σ of dc conductivity (see left panel). These properties of H_R and ΔH_σ corroborate in indicating the decrease of ion–ion interaction and many-ion dynamics as one of the manifestations of the mixed alkali effect.

3.2.10 Caged Dynamics, Nearly Constant Loss, and Termination by the Primitive Relaxation

For glassformers, we have discussed in Sections 2.3.2.6 and 2.3.2.33 the short time regime when the molecules are still caged and the local JG β-relaxation has not yet

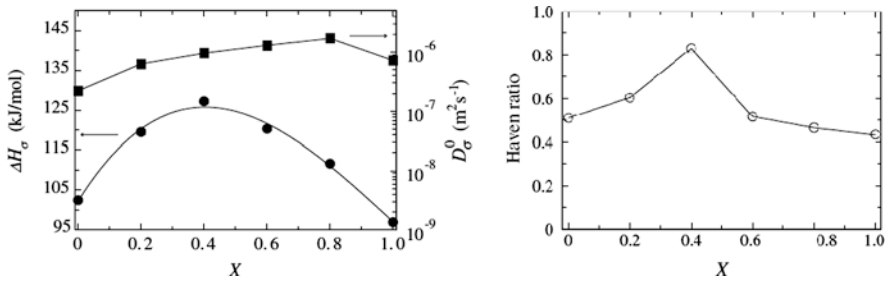

Fig. 314 (*Left*) Activation enthalpy ΔH_σ and pre-exponential factor D_σ^0 of the conductivity diffusion coefficient as a function of composition below the glass transition temperature for $0.2\,[x\mathrm{Na_2O} - (1-x)\mathrm{Rb_2O}] - 0.8\mathrm{B_2O_3}$ glasses. (*Right*) Composition dependence of the common Haven ratio of the same glass. Reproduced from [1693] by permission

appeared. In this caged regime, the dynamics shows up in susceptibility generally as the nearly constant loss (NCL) over an extended range of frequencies at lower temperatures. The lower bound of the frequency range of NCL is higher but not by much in frequency than the JG β-relaxation frequency ν_{JG} or the primitive frequency ν_0. This relation between the lower bound of NCL and ν_{JG} or ν_0 found in general for various glassformers supports the interpretation of the JG β-relaxation or the primitive relaxation terminates the caged dynamics regime and the NCL. Examples can be found in Figs. 1, 247, and 276 for colloidal particle suspensions; Fig. 119 for propylene carbonate; Fig. 135 for PIB; Fig. 241 for threitol and NMEC; and Figs. 243 and 244 for $0.4\mathrm{Ca(NO_3)_2} - 0.6\mathrm{KNO_3}$ (CKN). More examples from metallic glasses (see Fig. 170 for $\mathrm{Zr_{65}Al_{7.5}Cu_{27.5}}$) and ionic liquids can be found in Section 2.3.2.33. On increasing temperature, both ν_α and ν_{JG} increase and they tend to merge together, and this also increases the lower bound of the frequency regime in which the NCL can be detected. At high enough temperatures, the NCL regime is shrunk to the extent that it cannot be seen and is replaced by a susceptibility minimum. In time-domain experiments such as optical Kerr effect (OHD-OKE), the counterpart of the NCL is the term pt^{-1+c} with $c \approx 0$, called the intermediate power law (IPL), that usually appears at temperature below the critical temperature T_c of MCT and at times before the $\mathrm{d}t^{b-1}\exp(-t/\tau_\alpha)$ term, which accounts for the α-relaxation at high temperatures (see Section 2.3.2.33).

In glass-forming systems involving long-range diffusion such as binary mixtures of L–J particles and Li ion in Li metasilicate glass at low temperatures by simulations and colloidal particle suspensions at high concentrations by confocal microscopy, the counterpart of the NCL is the mean-square displacement $< r^2(t) >$ having the t^c dependence with $c \approx 0$ shown in Figs. 275 and 276. For the glass-forming ionic molten salt CKN, the NCL of caged dynamics was shown before by data of dielectric loss $\varepsilon''(\omega) \propto \omega^{-c}$ with $c \approx 0$ in Figs. 243 and 244, consistent with $< r^2(t) > \propto t^c$. This is because the relation between $< r^2(t) >$ and the complex conductivity $\sigma^*(\omega)$ shown in Eq. (3.3). The t^c dependence of $< r^2(t) >$ gives rise to the ω^{1-c} dependence of $\sigma'(\omega)$, the real part of $\sigma^*(\omega)$, from which the ω^{-c}-dependence of $\varepsilon''(\omega)$ follows from the Maxwell relation $\sigma^*(\omega) = \mathrm{i}\varepsilon_0\varepsilon^*(\omega)$. For

CKN, also shown in the figures is the relation of the lower bound of the NCL regime to the primitive relaxation frequency. The latter is slightly lower than the former. For colloidal particle suspension at volume fraction $\phi = 0.56$, the primitive relaxation time can be identified with the average time τ_c of 500 s for a typical particle to shift position and leaves the cage given by Weeks et al. from their experiment [141]. This time, indicated in the log–log plot of MSD in Fig. 247, clearly terminates the $t^{0.13}$ dependence of the MSD, which ends at about 250 s. The cage correlation function obtained by Weeks and Weitz [141(b)] also starts its decay at about 500 s as shown in the inset of the figure. The characteristics of the NCL and its termination by some primitive relaxation are common to relaxation in different families of interacting systems, the majority of examples come from the glassformers.

In this section, experimental conductivity relaxation data of NCL in glassy, molten, and crystalline ionic conductors are presented to show exactly the same behavior as the other interacting systems. For the benefit of making clear comparison of the characteristics of the NCL in ionic conductors with other systems, the rich dielectric loss data of the glassformer *N*-methyl-ε-caprolactam (NMEC) [508, 1733] are presented once more in Fig. 315. The data show clearly the NCL, the excess wing (i.e., the unresolved JG β-relaxation), and the structural α-relaxation.

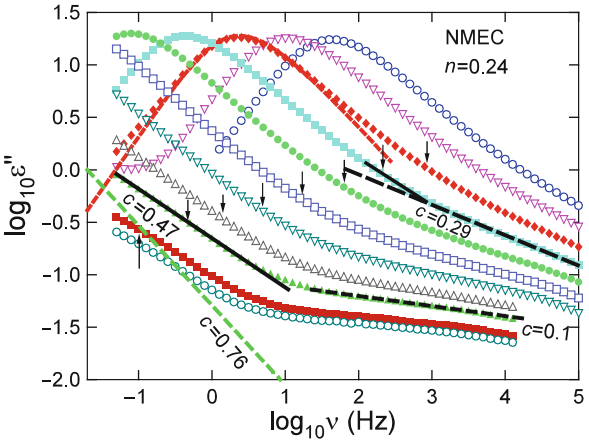

Fig. 315 Dielectric loss spectra of NMEC at temperatures above and slightly below T_g (*from right to left*: 186, 184, 182, 180, 178, 176, 174, 172, 170, 168, 164, 162 K) showing the following three distinct relaxation mechanisms. (1) The α-loss peaks and the fits (*red and pale blue dashed lines*) at two temperatures by the Fourier transform of the KWW function $\varphi(t) = \exp[-(t/\tau_\alpha)^{1-n}]$, with $n = 0.24$. (2) The excess loss $\varepsilon''(\nu) \sim \nu^{-c}$ with $c = 0.29$ (*long dashed line*) at 178 K and with $c = 0.47$ (*solid line*) at 168 K. The very different slopes of the excess loss at the same levels at the two temperatures rule out frequency–temperature superposition of the loss data of the excess loss in this region. (3) The emergence of the NCL $\varepsilon''(\nu) \sim \nu^{-c}$ with $c \approx 0.1$ (*black short dashed line*) with lower intensity at lower temperatures. The *green dashed line* with the label $c \approx 0.76$ shows the frequency dependence of the high-frequency flank of the KWW fit to the (unobserved) loss peak at 168 K. The *vertical arrows* indicate the relaxation time of the unresolved Johari–Goldstein β-relaxation suggested by the coupling model. Data are supplied by R. Richert and replotted here

Indicated by arrows in the figure, the locations of the primitive relaxation frequency calculated from the CM equation (3.1) are consistent with the interpretation that the NCL is terminated by the primitive relaxation.

Actually the best systems to show the NCL of caged dynamics are the glassy and crystalline ionic conductors. In contrast to glass-forming liquids, the existence of NCL in glassy ionic conductors has been known for more than half a century. Evidences for its existence were suggested repeatedly over the span of several decades starting from 1946 by Garton [1529] and many to follow [56(a), 115(b), 146, 149, 467, 1055–1061, 1424, 1522, 1523, 1530–1535, 1730, 1734–1751]. Not only there is an abundance of experimental data available but also the measurements are made over wide range of frequency and temperature in which the NCL has been detected. In many cases the spectral information is also complete to allow the primitive relaxation frequency/time to be calculated from the relaxation time and stretch exponent of the Kohlrausch function used to fit the electric modulus data and show the primitive relaxation terminates the NCL regime. Examples demonstrating this can be found in [1057–1059] and will be further discussed here. The existence of NCL in crystalline or polycrystalline ionic conductor including Na β-alumina [1486], YSZ [1484, 1755], LLTO [1059, 1755] and $LiAlSi_2O_6$ [1060] is particularly instructive to demonstrate that they exhibit the same caged dynamics as found in glass-forming systems. Some examples of the universal properties of caged dynamics will be presented later on in this section. Thus, any theory of caged dynamics, with applicability restricted to liquids such as MCT or to glasses such as random energy barrier model [1478], is not general enough to address the apparently universal properties of caged dynamics. To address the dynamics of ions beyond caged regime, ion–ion interaction and the many-ion dynamics generated have to be included, as has been demonstrated in several subsections above.

One general properties of the NCL in glassy as well as crystalline ionic conductors is its weak T dependence that can be described by either a power law, T^{α} with α not much greater than unity, or $\exp(T/T_0)$ [1056, 1058, 1059, 1060, 1752], similar to the temperature dependence of the NCL found in glassformers by dielectric relaxation [508, 971, 1026] and OHD-OKE (see Fig. 253). More examples of general properties of NCL in ionic conductors that are analogous to glassformers are presented below.

NCL exists not only in glassy $LiAlSi_2O_6$ but also in polycrystalline $LiAlSi_2O_6$. The magnitude of the NCL in polycrystalline $LiAlSi_2O_6$ is only about a factor between 2 and 3 times smaller than that in the glassy $LiAlSi_2O_6$ at the same temperature [1060]. It is not necessary to have structural disorder as in a glass or a liquid to generate the NCL. The comparable magnitudes of the NCL in polycrystalline and glassy $LiAlSi_2O_6$ suggest that the mechanism that gives rise to the NCL is somehow related to the local motion of the ion confined within the cage formed by the other ions. The cage defined by the anharmonic potential confining the ion is likely the only characteristic shared by both forms of $LiAlSi_2O_6$ as far as the NCL is concerned. Anharmonicity of the potential as well as mean-square displacement of the caged ion is expected to be larger in the glassy state than in the polycrystals, and this may explain the larger NCL observed in the former rather than in the latter.

The discussion and the analysis of conductivity relaxation data of crystalline and glassy ionic conductors follow the same line as those for CKN in Section 2.3.2.33. There two characteristic times t_{x1} and t_{x2} and the corresponding frequencies ν_{x1} and ν_{x2} are used to delineate three dynamic regimes. These two times are also involved in the description of the motions of ions in the space–time pictures generated by molecular dynamics simulations of Li metasilicate glass. The pictures presented in Fig. 280 are helpful when reading the following description. The very first dynamic regime is located at frequencies ν higher than ν_{x1} or at times t shorter than $t_{x1} \equiv 1/(2\pi\nu_{x1})$, where $\varepsilon''(\nu) = p\nu^{-c}$ or $\sigma'(\nu) \propto \nu^{1-c}$, and c is small. This is the caged ion regime or the NCL regime. The cage decays after t_{x1} by the onset of the primitive relaxation, which is an independent ion hop to neighboring sites in the case of ionic conductors. Naturally, we have $\tau_0 > t_{x1}$ or $\nu_{x1} > \nu_0$. The NCL regime is followed by the transition region defined by $\nu_{x1} > \nu > \nu_{x2}$ or $t_{x1} < t < t_{x2} \equiv 1/(2\pi\nu_{x2})$, in which more ions are hopping to neighboring sites and the motions become increasingly more cooperative with time. Here t_{x2} is the onset time of the "fully cooperative regime," where the Fourier transform of the derivative of the Kohlrausch function $\exp\left[-(t/\tau_K)^{1-n}\right]$ fits well the data in the complex modulus $M^*(\nu)$ representation for all $\nu < \nu_{x2}$. Perhaps it is appropriate to call this the "fully cooperative regime" because the Kohlrausch function is the characteristic function of the stable Levy distribution, a generalization of the Gaussian distribution [223]. Although τ_0 and ν_0 have been mentioned earlier, after all they can be calculated by Eq. (3.1) using the parameters τ_K and n of the Kohlrausch function, together with $t_c \approx 2\,\text{ps}$ or $\nu_c \approx 10^{11}\,\text{Hz}$ from high-frequency/high-temperature measurements shown in Section 3.2.3.1. If conductivity relaxation data are presented in terms of $\varepsilon''(\nu)$ or $\sigma'(\nu)$, instead of $M''(\nu)$, then ν_{x2} is defined as the frequency above which the power laws $\varepsilon''(\nu) \propto \nu^{-1+n}$ and $\sigma'(\nu) \propto \nu^n$ no longer hold. Demonstration of the evolution of the dynamics in the order of the frequencies ν_{x1}, ν_0, ν_{x2}, and $\nu_K = 1/\tau_K$ has been given before for CKN in several figures of Section 2.3.2.33. For data presented as the MSD, $< r^2(t) >$, t_{x2} is the onset time of the t^n dependence of $< r^2(t) >$. It has been shown together with t_{x1} and τ_0 in the plot of $< r^2(t) >$ vs. time for Li ions in metasilicate glass (Fig. 277), binary mixtures of L–J particles (Fig. 275), and colloidal particle suspensions (Fig. 276) in Section 3.2.1 before.

Conductive relaxation data of some crystalline and glassy ionic conductors are now shown to have the same time evolution of dynamics as glassformers in support of the universal dynamics in interacting systems. To familiarize the reader with such data given in terms of $\sigma'(\nu)$, the same data of the molten salt, CKN, presented before in terms of $\varepsilon''(\nu)$ and $M''(\nu)$ in Figs. 243 and 244 are recast in this form in the left panel of Fig. 316. Shown also are the locations of ν_{x1}, ν_0, ν_{x2}, and ν_K. The line with slope equal to 1 is drawn to indicate $\sigma'(\nu) \propto \nu^{1-c}$ with $c << 1$, corresponding to the NCL. The dashed line represents $\sigma'(\nu)$ exactly calculated from the Kohlrausch fit to $M^*(\nu)$, and it gives the dc conductivity at low frequencies and the power law $\sigma'(\nu) \propto \nu^n$ at high frequencies. Actually, $\sigma'(\nu)$ data of glassy ionic conductors $0.44LiBr–0.56Li_2O–B_2O_3$ at 323 and 573 K and $0.5Ag_2S–0.5GeS_2$ glass at 273 K in Fig. 282 have shown some of the same features already. Here we show in more detail the $\sigma'(\nu)$ data of other glassy ionic conductor $0.80LiF–0.20Al(PO_3)_3$ from

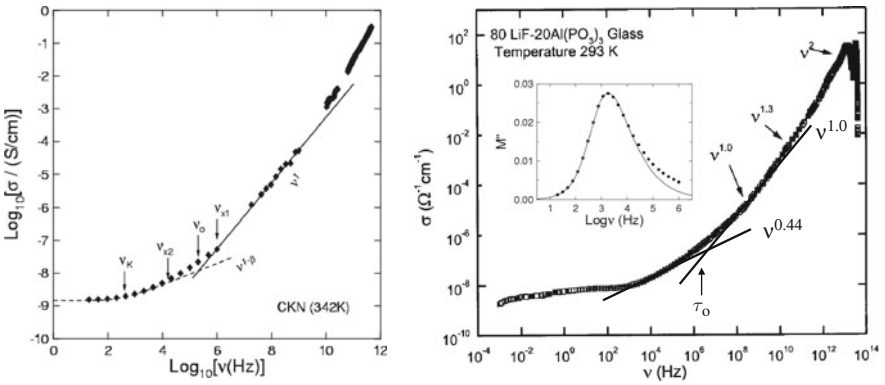

Fig. 316 (*Left*) Replotting the CKN data of Fig. 243 as $\log \sigma(\nu)$ vs. log(frequency/Hz) to show the nearly linear frequency dependence of the NCL. The *dashed line* that includes the dc conductivity and the high-frequency power law $\nu^{1-\beta}$ or ν^n corresponds to the Kohlrausch fit to the electric modulus with n=0.34. Reproduced from [1057] by permission. (*Right*) Log $\sigma(\nu)$ at several temperatures of a glassy ionic conductor 0.80LiF–0.20Al$(PO_3)_3$ vs. log(frequency/Hz). The data show a near linear frequency ($\nu^{1.0}$)-dependent conductivity and a broad crossover to the $\nu^{0.44}$ dependence (obtained from the Kohlrausch function fit to the electric modulus in the *inset*) and finally to the dc conductivity. ν_0 (erroneously replaced by τ_0) is the independent relaxation frequency of an ion hopping out of its cage, which is calculated from the CM. Redrawn from data of Kulkarni et al. [1756]. Reproduced from [1057] by permission

the work of Kulkarni et al. [1756] in the right panel of Fig. 316, the data of glassy $0.5Ag_2S$–$0.5GeS_2$ from the work of Ribes et al. [1757] in the left panel of Fig. 317, and the data of $0.48(AgI)_2$–$0.52Ag_2SeO_4$ from the work of Cramer and Buscher [1528] in the right panel of Fig. 317. In all cases, $n = (1-\beta)$ was determined by the fit to the *same* data in the electric modulus representation by the Fourier transform of the Kohlrausch function $\Phi(t)$ in Eq. (1.56), and τ_0 is calculated from the CM equation.

The reader may recall that $0.5Ag_2S$–$0.5GeS_2$ was discussed before in Section 3.2.3 on the comparison between activation energies of short-time silver ion diffusion measured by quasielastic neutron scattering and long-time conductivity relaxation (see Table 3.2). The glass $0.48(AgI)_2$–$0.52Ag_2SeO_4$ was also discussed in Section 3.2.3 in a similar context. As an aside, the dielectric loss data of this glassy ionic conductor was shown to fit the MCT predictions (see Fig. 284), even though MCT does not apply to ionic conductivity relaxation in glasses. This warns the possibility that good fits to susceptibility minima to MCT predictions in supercooled liquids do not necessarily validate MCT as the uniquely correct description of caged dynamics of glassformers.

In all the ionic conductors shown in Figs. 316 and 317, the caged dynamics (NCL) regime ending at ν_{x1} is terminated by the primitive relaxation as evidenced by the location of its relaxation frequency ν_0 not much longer than ν_{x1}. At frequencies lower than ν_0, there is a gradual transition of $\sigma'(\nu)$ before it finally assumes the frequency dependence of the cooperative Kohlrausch ion hopping starting at ν_{x2}.

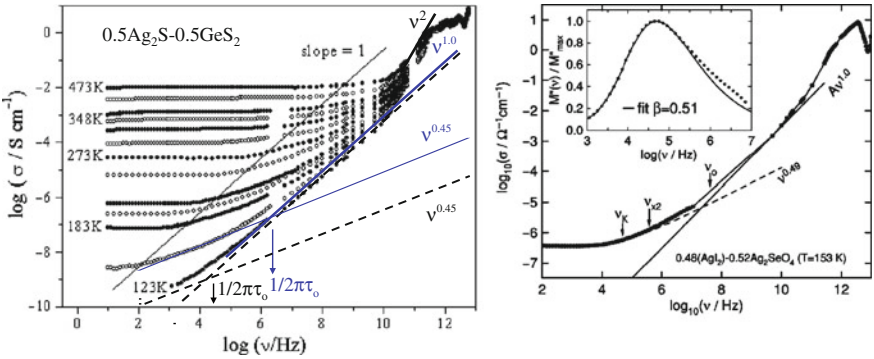

Fig. 317 (*Left*) Log $\sigma(\nu)$at several temperatures of a glassy ionic conductor, $0.5Ag_2S–0.5GeS_2$, from the work of Ribes et al. [1757] vs. log(frequency/Hz). The data show a near-linear frequency ($\nu^{1.0}$)-dependent conductivity and a broad crossover to the $\nu^{0.45}$ dependence (obtained from the Kohlrausch function fit to the electric modulus) and finally to the dc conductivity. $\nu_0(= 1/2\pi\tau_0)$ is the independent relaxation frequency of an ion hopping out of its cage, which is calculated from the CM. Reproduced from [1057] by permission. (*Right*) Log $\sigma(\nu)$vs. log(frequency/Hz) at 153 K of a glassy ionic conductor $0.48(AgI)_2–0.52Ag_2SeO_4$ from the work of Cramer and Buscher [1528]. The data show a near-linear frequency ($\nu^{1.0}$)-dependent conductivity and a broad crossover to the $\nu^{0.49}$ dependence (obtained from the Kohlrausch function fit to the electric modulus) and finally to the dc conductivity. $\nu_0(= 1/2\pi\tau_0)$ is the independent relaxation frequency of an ion hopping out of its cage, which is calculated from the CM. The *dashed line* is the cooperative ion conductivity relaxation. Reproduced from [1057] by permission

The latter begins with the fractional power $\sigma'(\nu) \propto \nu^{-n}$ and on decreasing frequency it flattens out to assume the frequency-independent dc conductivity σ_{dc} at low frequencies. This behavior is clearly demonstrated in Figs. 316 and 317.

The examples of glassy ionic conductors discussed above all have sizeable n in the exponent (1–n) of the Kohlrausch function, $n = 0.34, 0.44, 0.45$, and 0.49 for CKN, $0.80LiF–0.20Al(PO_3)_3$, $0.5Ag_2S–0.5GeS_2$, and $0.48(AgI)_2–0.52Ag_2SeO_4$, respectively. The sizeable n values are expected from significant many-ion cooperative relaxation in these ionic conductors containing high concentration of mobile ions. It is instructive to compare them with the dynamics of ions in conductors with lower ion concentrations. In Section 3.2.2.1, the decrease of n reflecting diminishing many-ion cooperative dynamics with decreasing ion concentration has been discussed. Here, at constant ν_K, the dependence of the magnitude of the caged dynamics (NCL) on ion concentration (or n) is discussed, as well as the dependences of the characteristic frequencies ν_{x1}, $\nu_{0,}$ and ν_{x2}. This comparison is analogous to the comparison made before for the glassformers, NMEC ($n = 0.24$), threitol ($n = 0.36$), and xylitol ($n = 0.46$) in Fig. 241, and for CKN vs. $ZnCl_2$, and CKN vs. B_2O_3 in Fig. 250 at constant or approximate constant structural relaxation frequency ν_α. Although ν_{x1}, $\nu_{0,}$ and ν_{x2} are not illustrated in these figures, it can be gathered by inspection of the spectra that glassformer with smaller n has lower values of ν_{x1}, $\nu_{0,}$ and ν_{x2} as well as lower NCL (relative to the α-relaxation). In addition, the NCL is also terminated by the primitive or JG relaxation frequency in each of these

glassformers. Although similar trend can be deduced from several comparisons of NCL in ionic conductors at the same temperature [1056, 1060, 1061], the cogent comparison has to be made at the same ν_K. An example is given as follows.

A comparison of the entire range of dynamics including the NCL of two glassy oxide Na ion conductors with very different ion concentrations is shown in Fig. 318. Plotted in the left panel of the figure are $\log[\sigma'(\nu)]$ vs. $\log \nu$ of a Na_2O–$3SiO_2$ glass at –0.5°C with a high concentration of mobile Na^+ ions [1518] and of a Vycor glass $x Na_2O - (1 - x)[0.04B_2O_3 - 0.96SiO_2]$ at 313°C with small $x = 0.00044$ and hence containing very few Na^+ ions [1506]. The conductivity relaxation frequency ν_K of the two glasses at these temperatures has been determined by the Kohlrausch fit to the *same* data in the electric modulus representation, which is shown in the right panel of Fig. 318. ν_K is practically the same as the peak frequency ν_{max} at the maximum of $M''(\nu)$. The ν_K of the two glasses differ only by a factor of about 2, and thus this near-isoconductivity relaxation time condition is satisfied for making objective comparison of the NCL in these two ionic conductors.

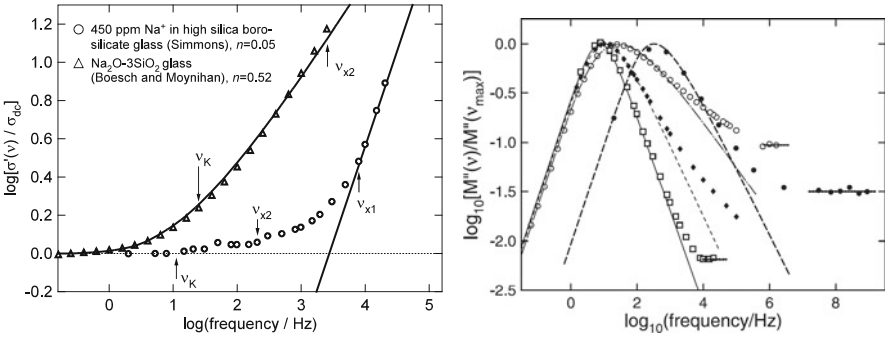

Fig. 318 (*Left*) Isothermal electrical relaxation data shown as plots of $\log\left[\sigma'(f)/\sigma_{dc}\right]$ vs. $\log f$ for a Na_2O–$3SiO_2$ glass at –0.5°C and for a Vycor glass $x Na_2O-(1-x)[0.04B_2O_3-0.96SiO_2]$ at 313°C with $x = 0.00044$. Reproduced from [1057] by permission. (*Right*) Scaled $M''(\nu)$ data of several ionic conductors. The Na trisilicate glass (*open circles*) and the Kohlrausch fit with $n = 0.50$ (*dashed-dotted line*). Vycor glass $x Na_2O - (1 - x)[0.04\,B_2O_3 - 0.96\,SiO_2]$ with $x = 0.00044$ (*open squares*) and the Kohlrausch fit with $n = 0.05$ (*solid line*). The CKN data at 333 K (*closed diamonds*) and at 342 K (*closed circles*), together with the Kohlrausch fits with $n = 0.28$ (*thinner dashed line*) and 0.33 (*thicker dashed line*), respectively. The *horizontal lines* indicate the levels of NCL. Reproduced from [1482] by permission

In the left panel of the figure, the $M''(\nu)$ data of the Na trisilicate glass, the Vycor glass, and CKN at two temperatures 333 and 342 K are compared after normalizing $M''(\nu)$ by $M''(\nu_{max})$, the maximum value at the loss peak. The NCL appearing at the high-frequency end, $A_M \nu^{-c}$ with $c << 1$, is indicated for each case by the horizontal line. It can be seen from the comparison that ionic conductor with broader dispersion or large n in $M''(\nu)$ has higher level of NCL relative to the $M''(\nu_{max})$. In the order of increasing ratio NCL/$M''(\nu_{max})$, Vycor glass has $n = 0.05$, CKN has n=0.28 and 0.33, and the Na trisilicate glass has $n = 0.50$. The reader may recognize the similarity between the trend of the NCL in ionic conductors shown in the left

panel of Fig. 318 and that of the NCL in glassformers in Figs. 241 and 250 at constant or approximate constant structural relaxation frequency ν_α. The correlation between NCL and n found in the dynamics of the two systems is another evidence for universal properties of interacting systems.

In the plot of $\left[\sigma'(\nu)/\sigma_{\rm dc}\right]$ against log ν in the left panel of Fig. 318, it can be seen that the Vycor glass has ν_{x2} much closer to $\nu_{\rm K}$ than the Na_2O–$3SiO_2$ glass, which is another indication of much narrower dispersion of the former compared with the latter. The same is true for ν_{x1}; the location of it for the Vycor glass is well inside the range of frequencies shown, while that for the Na_2O–$3SiO_2$ glass is outside and not shown (data at higher frequencies are truncated in this plot). The NCL appears in this plot as $\sigma'(\nu)/\sigma_{\rm dc} \approx A_\sigma \nu^{1-c}$, with $c << 1$. The larger NCL of Na trisilicate glass than Vycor glass is reflected in this plot by larger value of A_σ of the former compared with the latter. A similar situation was found by Jain et al. in the comparison of $\sigma'(\nu)$ for two $xK_2O - (1-x)GeO_2$ glasses with $x = 0.20$ and 0.0023 [1512]. Whether considered by $A_{\rm M}\nu^{-c}$ in $M''(\nu)/M''(\nu_{\rm max})$ at constant $\nu_{\rm K}$ or by $A_\sigma \nu^{1-c}$ in $\sigma'(\nu)/\sigma_{\rm dc}$, NCL is smaller in ionic conductor having smaller n. This trend is the same as that found for the glassformer such as the pair NMEC and xylitol in Fig. 241, and the pair CKN and $ZnCl_2$ in Fig. 250 (at the same ν_α). For ionic conductors, the trend has been rationalized in [1058, 1417] by the fact that ν_0 terminates the NCL and ν_0 is located at higher frequency (at constant ν_K). A similar explanation for glassformer is by the fact that $\nu_{\rm JG}$ or ν_0 terminates the NCL and $\nu_{\rm JG}$ or ν_0 is located at higher frequency (at constant ν_α) for glassformer with smaller n [507]. Incidentally, this trend in glassformers readily explains the deep and sharp susceptibility minimum found in "strong" glassformers having small n such as $ZnCl_2$ or B_2O_3 (Fig. 250–1). This is because the depth of the minimum is determined by the NCL which is low in these glassformers. That is also the reason why the idealized MCT fails to fit the susceptibility minimum $\chi''(\nu)$ of these "strong" glassformers because the predicted spectral shape of the minimum is given by $\chi''(\nu) = \chi''_{\rm min}\left[a(\nu/\nu_{\rm min})^{-b} + b(\nu/\nu_{\rm min})^a\right]/(a+b)$. Since a has to be less than 0.395, MCT cannot explain the sharp minimum seen in the "strong" glassformers. Conversely, the higher level of NCL of "fragile" glassformers with larger n can produce a shallower minimum satisfying the condition $a < 0.395$, and MCT fit can be successful. The main point is that NCL is responsible for the susceptibility minimum, which can be shallow or deep depending on the NCL level controlled by n. This is another example of the connection of the faster dynamics to the ultimate many-body relaxation dynamics characterized by its dispersion or the coupling parameter n.

The examples from CKN, $0.80LiF$–$0.20Al(PO_3)_3$, $0.5Ag_2S$–$0.5GeS_2$, and $0.48(AgI)_2$–$0.52Ag_2SeO_4$ have been chosen to elucidate the NCL in isothermal spectra because the measurements were made over enormous broad frequency range for us to see the relation between the characteristic frequencies ν_{x1}, ν_0, ν_{x2}, and $\nu_{\rm K}$. If measurement is made over a limited range of frequency typically from 10 Hz to 1 MHz, fast and slow processes only can be seen together in isochronal spectra of $\sigma'_\nu(T)$ at constant ν. The faster caged dynamics appears in $\sigma'_\nu(T)$ at lower temperatures, and it is unmistakably the NCL because $\sigma'_\nu(T)$ has the frequency

dependence of ν^{1-c} with $c << 1$ at constant T [1059, 1758]. The crossover from NCL to primitive ion relaxation and subsequently to cooperative ion dynamics can be seen from the progressive change in T dependence of $\sigma'_\nu(T)$. The best example is the analysis of $\sigma'_\nu(T)$ measured over finely spaced temperatures down to 8 K in the frequency range 10 Hz–1 MHz reported by León and coworkers on two different Li ionic conductors, one is the crystalline $Li_{0.18}La_{0.61}TiO_3$ (LLTO) and the other is the glassy $61SiO_2$–$35Li_2O$–$3Al_2O_3$–$1P_2O_5$ [1059], and by Rivera et al. in $(Y_2O_3)_{0.16}(ZrO_2)_{0.84}$ and glassy Li, Na, K, and Rb triborate glasses [1755]. At lower temperatures, an NCL corresponding to linear frequency-dependent ac conductivity is the dominant contribution. As temperature is increased, a crossover from the NCL to a fractional power law frequency dependence of the ac conductivity ν^n is observed at fixed T (see left panel of Fig. 319 for LLTO).

The data in the left panel of the figure also show the weak dependence of the NCL that is proportional to $\exp(T/T_o)$. For each isochronal at a fixed frequency ν, the open square indicates the crossover point $(T_x, \sigma'_\nu(T_x))$ from the weak T dependence of NCL to the stronger activated T dependence of the ac conductivity ν^n with a criterion explained in [1758]. Naturally, the crossover can be identified with termination of the NCL regime. The coordinates of the crossover points are shown again as open squares in the Arrhenius plot of conductivity in the right panel of Fig. 319. The closed circles are additional crossover points at higher frequencies determined by a method discussed in [1758]. Shown also is the dc conductivity as a function

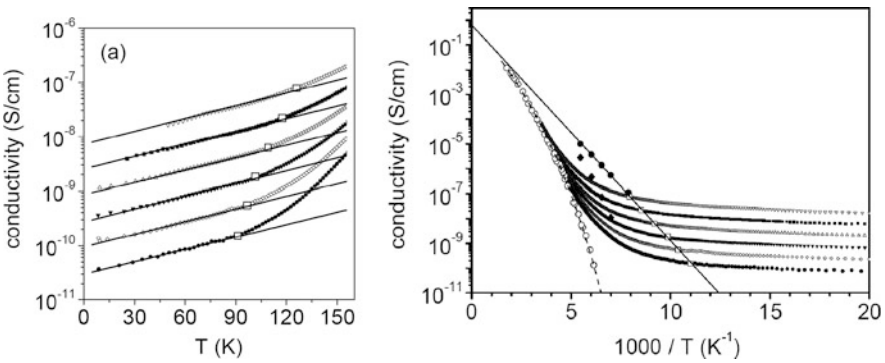

Fig. 319 (*Left*) Conductivity vs. temperature plots for LLTO. Conductivity data are shown for different frequencies (300 Hz, 1, 3, 10, 30, and 100 kHz, from *bottom* to *top*) in a linear temperature scale. *Open square symbols* represent the crossover between the linear frequency-dependent conductivity (NCL regime) and the power law ν^n regime, which is due to ionic hopping. *Solid lines* are fits to exponential temperature dependence of conductivity data in the NCL regime. (*Right*) Arrhenius plots of conductivity data of LLTO at different frequencies (300 Hz, 1, 3, 10, 30, and 100 kHz, from *bottom* to *top*). *Open square symbols* represent the crossover points obtained from the *left panel*, and *solid circles* are the crossover points at higher frequencies determined by method discussed in [1758]. The *solid line* is a fit to an Arrhenius law for the crossover temperature dependence. *Open circles* are dc conductivity data. *Closed diamonds* are the crossover points calculated by assuming the validity of the augmented Jonscher equation, which shows an activation energy close to that observed for the dc conductivity. Reproduced from [1758] by permission

of temperature (open circles), which is non-Arrhenius as the reader may recall from Section 3.2.6.4.

The solid line is a fit to an Arrhenius law for the crossover points, showing the relation $\sigma'_\nu(T_x) = \sigma_\infty \exp(-E_m/kT_x)$, where $E_m = 0.17 \pm 0.03$ eV, and $\sigma_\infty \approx 1$ S/cm, which corresponds to a conductivity relaxation time τ of the order of magnitude of 10^{-11} s from the Maxwell relation $\sigma = \varepsilon_0\varepsilon_\infty/\tau$. It turns out that E_m is nearly the same as the temperature-independent primitive activation energy $E_\mathrm{a} \approx 0.175$ eV of the independent ion hopping relaxation time τ_0 that was calculated by the products $[1 - n_\sigma(T)]\,E_\sigma(T)$ over a range of temperatures for LLTO (see Section 3.2.6.4 and Fig. 304, upper right). Hence E_m is identified with the energy of the barrier preventing the Li^+ ions to abandon their cages, and the relaxation time corresponding to $\sigma'_\nu(T_x)$ is the primitive ion relaxation time τ_0. The result is another indication that the NCL occurs while most of the ions are still caged and is terminated by the primitive ion relaxation. Naturally an estimate in order of magnitude of the time for the ions to leave their respective cages is given by the primitive relaxation time of the CM. At a longer time t_{x2} after which essentially all ions have high probability of successfully jumping out of their cages, they start the cooperative ion conductivity relaxation process well described by the Kohlrausch correlation function.

3.2.10.1 Caution for Those Who Prefer Data Represented by $\sigma'(\nu)$ than $M^*(\nu)$

Before leaving Fig. 316, it is instructive to consider a popular expression of Jonscher [124], often used to interpret conductivity relaxation of ionic conductors. Jonscher's expression for the real part of the conductivity is

$$\sigma(\nu) = \sigma_0[1 + (\nu/\nu_\mathrm{p})^n], \tag{3.49}$$

where σ_0 is the dc conductivity, ν_p the characteristic relaxation frequency, and n the fractional exponent. At higher frequencies the ν dependence given by Eq. (3.49) no longer works and is replaced by ν^{1-c} with $c << 1$, the NCL term. To include the NCL, some workers add a term $A\nu$ to the right-hand side of Eq. (3.49):

$$\sigma'(\nu) = \sigma_0\left[1 + \left(\frac{\nu}{\nu_p}\right)^n\right] + A_\sigma \nu. \tag{3.50}$$

Recalling Fig. 245, where it is shown the NCL in glassformers is not an additive contribution to the susceptibility, one would be skeptical of this approach in ionic conductors. Since σ_0 and ν_p are thermally activated with the dc activation energy E_σ, meanwhile A_σ shows a much milder temperature dependence, it can be shown from Eq. (3.50) that the crossover between the two terms should be thermally activated with the energy E_σ. The crossover point is readily obtained by equating the NCL term to the real part of the ac conductivity given by the Jonscher's expression at the crossover frequency. The locations of the crossovers shown by the closed diamonds in Fig. 319 indeed have the T dependence of σ_dc and do not correspond in any way to the NCL.

Jonscher's expression for the $\sigma'(\nu)$ in Eq. (3.49) gives no characteristic times explicitly. Users of this expression usually define a characteristic time via the characteristic frequency ν_c by the equation $\sigma'(\nu_c) = 2\sigma_{dc}$. The ν_c so defined may be close to ν_K in ionic conductors having higher concentrations of ions and larger n like Na_2O–$3SiO_2$ glass shown in the left panel of Fig. 318, and has activation energy nearly the same as σ_{dc}. However, when $\sigma'(\nu_c) = 2\sigma_{dc}$ is applied to ionic conductors with low concentration of ions and small n such as the Vycor glass $x\mathrm{Na_2O} - (1-x)[0.04\mathrm{B_2O_3} - 0.96\mathrm{SiO_2}]$, ν_c is more than two decades higher than ν_K and it has much weaker T dependence than σ_{dc}. Thus, $\sigma'(\nu_c) = 2\sigma_{dc}$ yields ν_c associated with different dynamics for ions with different concentration and/or width of dispersion and n. Imre et al. [1693] applied this to determine ν_c, which they called ν_{on}, to the series of the mixed alkali glasses $0.2[x\mathrm{Na_2O} - (1-x)\mathrm{Rb_2O}] - 0.8\mathrm{B_2O_3}$ with $x = 0.0$, 0.2, 0.4, 0.6, and 0.8. The mixed alkali (MA) effects were shown before in Figs. 308 and 311. The activation enthalpies ΔH_σ of dc conductivity show a maximum at some $X = 0.4$ in Fig. 311 and also in Fig. 320, but the activation enthalpies $\Delta H_{\nu_{on}}$ of ν_{on} do not, which is almost independent of composition. Thus ΔH_σ shows the mixed alkali effect as usual, but $\Delta H_{\nu_{on}}$ do not. Imre et al. were taken by surprise. But this is no surprise in view of the discussion above. The number of mobile ions in the mixed alkali glasses is fewer than that in the single alkali glasses, and ν_{on} in the MA glasses no longer corresponds to dc conductivity. Consequently, the activation enthalpy $\Delta H_{\nu_{on}}$ of MA glasses is smaller than ΔH_σ, and it shows no MA effect or at least smaller effect than ΔH_σ. The danger of using the Jonscher's expression to interpret deeper properties of ion dynamics is made clear by this example.

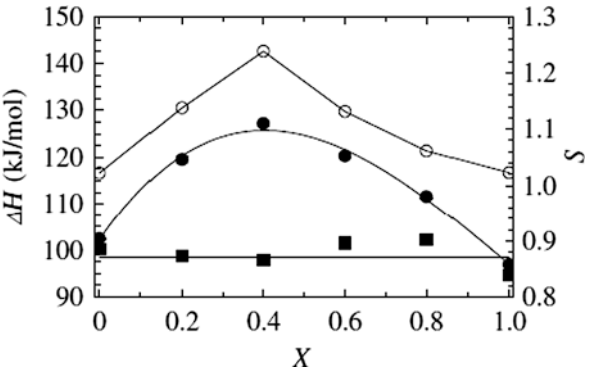

Fig. 320 Composition dependence of activation enthalpies ΔH_σ (●) and $\Delta H_{\nu_{on}}$ (■) for the $0.2[x\mathrm{Na_2O}$–$(1\text{-}x)\mathrm{Rb_2O}]$–$0.8\mathrm{B_2O_3}$ mixed alkali glasses – *left axis*. The quantity S (○) – *right axis* is of no interest here and not discussed in the text. Reproduced from [1693] by permission

3.2.10.2 Rationalization of the Observed Properties of NCL by Its Relation to the Primitive Relaxation

Crystalline and Ionic Conductors

From the close relation between $t_{x1}(T)$ and $\tau_0(T)$, $t_{x1}(T)$ has the same activation energy as E_a of $\tau_0(T)$. This has been demonstrated in Fig. 319 for Li ion dynamics

in LLTO and other crystalline and glassy ionic conductors [195, 1058, 1059, 1755, 1758], and hence we have $t_{x1}(T) = t_\infty \exp(E_a/kT)$. Given the fact that the NCL is terminated at $t_{x1}(T)$) by the same process (i.e., the primitive ion hop), $< r^2(t_{x1}(T)) >$ is expected to have the same value independent of temperature or $t_{x1}(T)$. From its onset at t_{on} and up to $t_{x1}(T)$, $< r^2(t_{x1}(T)) >$ or the NCL increases by the same amount for all temperatures. However, because t_{x1} is thermally activated, this same increase of $< r^2(t_{x1}(T)) >$ is spread over a number of decades of time given by $\{\log_e [t_{x1}(T)] - \log_e(t_{on})\}/2.303$. Therefore $< r^2(t_{x1}(T)) >$ is inversely proportional to $\log_e \left[t_{x1}(T)/t_{on}\right]$. From this proportionality and the relation between conductivity and mean-square displacement (Eq. (3.4)), the magnitude A of the NCL, $\varepsilon''(\nu) = A\nu^{1-c}$ with $c << 1$, is given by the proportionality relation [1058]

$$A \propto \frac{1}{E_a}[1 - (kT/E_a)\log_e(t_{on}/t_\infty)]^{-1}. \tag{3.51}$$

This expression is well approximated by

$$A \propto (E_a)^{-1}\exp(T/T_0), \quad \text{for} \quad T << T_0 \tag{3.52}$$

with

$$T_o \approx E_a/k \log_e(t_{on}/t_\infty). \tag{3.53}$$

Note that T_0 is a positive number because $\log_e(t_{on}/t_\infty)$ is a positive number from the fact that $t_{x1} < \tau_0$, and hence t_∞ is even shorter than τ_∞, the prefactor of τ_0, which is the reciprocal of a vibrational attempt frequency. Thus the weak temperature dependence of the NCL is captured by the interpretation of the origin of the NCL within the framework of the CM. Since the result given by Eqs. (3.51) and (3.52) is obtained from a qualitative argument, we do not expect that it will accurately describe the temperature dependence of the NCL, particularly if considered over a very extended temperature range where another source of contribution to NCL may come into play at very low temperatures and high frequencies, such as transitions between the asymmetric double-well potentials (ADWPs) [1744, 1755, 1759]. Of course, the ADWPs constitute a different source of the NCL than the slow cage decay process discussed here.

Note that according to Eq. (3.51), at constant temperature, A should decrease with increasing E_a, had other factors like ion concentration that determines the absolute value of A are the same for the ionic conductors to be compared. If this condition holds for many ionic conductors, then an approximate anticorrelation between A and E_a may exist at constant T. This is an important prediction and can be tested by experiment. Previously, Rivera et al. [1061] measured the intensity of the NCL A in four alkali triborate glasses M_2O–$3B_2O_3$, with M = Li, Na, K, and Rb. They observed that A approximately has the $m^{-1/3}$-dependence and this dependence led them to speculate vibrational relaxation as the origin of the NCL. The new interpretation of the NCL given in this work was not available at the time of writing

[1061]. Now it replaces the earlier speculation. Its prediction, $A \propto 1/E_a$, replaces the less general observation that $A \propto m^{-1/3}$. The former can be rigorously tested by the alkali triborate glasses data of Rivera et al. [1061]. This test has been done by calculating E_a from the experimental determined activation energy E_a^* of τ_K by using the relation $E_a = (1-n)E_a^*$ and $(1–n)$ from the Kohlrausch fit of the electric modulus loss peak [1752]. The results of E_a in fact is inversely proportional to A in the family of alkali triborate glasses investigated by Rivera et al., and this is shown in the left panel of Fig. 321 among other ionic conductors.

The predicted approximate correlation between the magnitude A of the NCL and the reciprocal of primitive activation energy E_a by Eq. (3.51) can be tested beyond the family of alkali borate glasses. This has been carried out by León et al. at $T = 100$ K for many ionic conductors [1752]. The results in the left panel of Fig. 321 show the remarkable agreement between experimental data for a variety of ionic conductors and the correlation predicted. The solid line in the figure represents an exact inversely proportional relation. It is indeed noteworthy that such a correlation holds considering there may be other factors which affect the magnitude of the

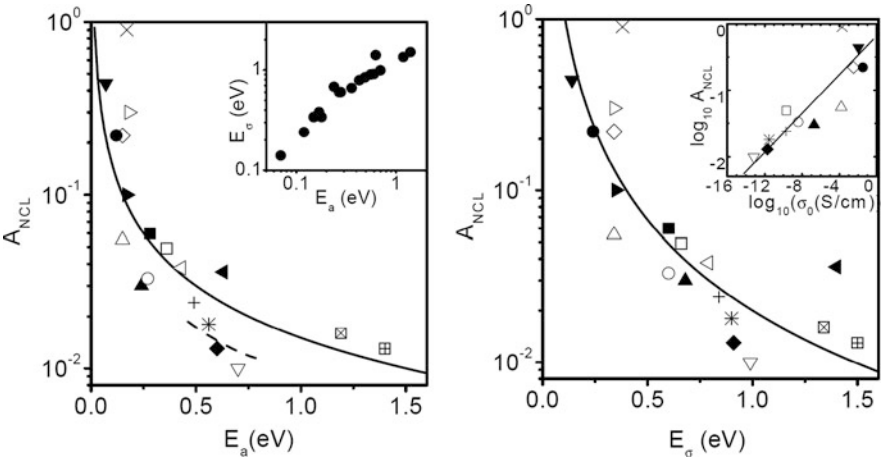

Fig. 321 (*Left*) A remarkable correlation is observed when plotting the magnitudes A of the NCL at $T = 100$ K vs. the activation energy E_a for a variety of ionic conductors. $Li_2O-3B_2O_3$ (+), $Na_2O-3B_2O_3$ (∗), $K_2O-3B_2O_3$ (♦), $Rb_2O-3B_2O_3$ (▽), $LiPO_3$ (▲), $35Li_2O-61SiO_2-3Al_2O_3-P_2O_5$ (◯), $Li_{0.18}La_{0.61}TiO_3$ (×), $(ZrO_2)_{0.84}(Y_2O_3)_{0.16}$ (◀), $Na_2O-3SiO_2$ (□), $(AgI)_{0.3}-(AgPO_3)_{0.7}$ (▷), $(AgI_2)_{0.48}-(Ag_2SeO_4)_{0.52}$ (◇), $Na-\beta Al_2O_3$ (▼), $(Li_2S)_{0.56}-(SiS_2)_{044}$ (▶), $(Ag_2S)_{0.5}-(GeS_2)_{0.5}$ (△), Ag_7GeSe_5I (•), $(LiF)_{0.8}(Al(PO_3)_3)_{0.2}$ (■), $xK_2O-(1-x)GeO_2 (x = 0.2)$ at T = 381 K (◁), $xK_2O-(1-x)GeO_2$ $(x = 0.02)$ at T = 367 K (⊠), $xK_2O-(1-x)GeO_2$ $(x = 0.0023)$ at $T = 374$ K (⊞). *Solid line* represents an inversely proportional relation as derived from the model for the NCL (see Eq. (3.51)). *Dashed line* represents a fit to Eq. (3.51) for the family of alkali triborate glasses. The *inset* shows that the smaller the value of E_a, the smaller the activation energy E_σ for the dc conductivity for the set of ionic conductors shown in the main panel. (*Right*) Main figure shows the correlation between the magnitude A of the NCL at $T = 100$ K and the activation energy, E_σ, of the dc conductivity. *Symbols* are the same as those used in the *left panel*. The *inset* shows the same NCL data vs. the dc conductivity at room temperature. *Lines* are guides for the eye. Reproduced from [1752] by permission

NCL and have not been taken into consideration. The question arises if the correlation still holds when considering the activation energy E_σ for the dc conductivity instead of E_a. It has been shown [1706(a)] for different families of ionic conductors that the one with smaller activation energy E_σ has larger coupling parameter n and hence correspondingly smaller E_a, and rationalized therein by enhanced inter-ionic coupling in ionic conductors with smaller primitive energy barrier E_a. This correlation between E_a and E_σ is obeyed by the ionic conductors considered here and is shown in the inset of the left panel of Fig. 321. From this empirical relation between E_a and E_σ, and the correlation that holds between A and E_a, we also expect a correlation between A and E_σ. The magnitude A of the NCL is plotted in the right panel of Fig. 321 vs. the activation energy E_σ, and a strong correlation indeed exists between them. This correlation is noteworthy because very different time and spatial scales are involved in dc conductivity and the NCL. While the dc conductivity is related to charge transport over long range at long times, the NCL observed at high frequencies in the ac conductivity originates from motion while the ions are still caged. The inset shows that a correlation is also observed between A and the logarithm of the dc conductivities at room temperature σ_o. Since $\sigma_0(T) = \sigma_\infty \exp(-E_\sigma/kT)$ and the prefactor σ_∞ takes not too different values in all ionic conductors, the rule that higher the E_σ, the smaller the dc conductivity at room temperature is usually obeyed. Therefore, the correlation observed between A and the dc conductivities at room temperature can also be considered simply to follow from the correlation between A and E_a deduced from Eq. (3.51).

Even though NCL originates in the caged ions regime, yet its magnitude correlates with the dc conductivity either via its activation enthalpy or its value at room temperature. This happens because NCL is connected to the primitive ion hopping motion, which in turn is connected to the many-ion cooperative hopping motions and finally the dc conductivity. Without this insight, the correlation of the NCL with dc conductivity may have tempted others to jump to the conclusion that the NCL is associated with ion hopping motions of the mobile ions. In fact this erroneous conclusion was proffered by Murugavel and Roling [1760] from their own findings of a correlation between the magnitude of the NCL at T=173 K and the dc conductivity at room temperature of Li, K, and Na alumino-silicate and alumino-germanate glasses. These authors also found that the magnitude of the NCL is higher for the sodium ion conducting glass as compared to the lithium ion conducting glass. This observation clearly is opposite to alkali mass dependence of the NCL found by Rivera et al. [1061] for the alkali triborate glasses. Interestingly, in the case of the alumino-silicate glasses, the dc conductivity of the sodium ion conducting glass is approximately twice as high as the dc conductivity of the lithium ion conducting glass. This is opposite for the alkali borate glasses, where lighter alkali has larger dc conductivity at room temperature (see inset in the right panel of Fig. 321). The reversal of trend in the alkali alumino-silicate glasses is caused by the replacement of silicon by the trivalent aluminum, which changes the structure of the oxide glass. Thus, the results of the alkali alumino-silicate glasses from Murugavel and Roling [1760], as well as the alkali borate glasses from Rivera et al., are in accord with the prediction stemming from Eq. (3.51). Here, the NCL is loss due to ions while still caged due to the anharmonic potential and fluctuations of the cages.

Glassformers

Experimentally, the NCL found in non-ionic glassformers in the equilibrium liquids state or the glassy state is no different from the NCL of crystalline, molten, or glassy ionic conductors. Conceptually they have similar origin due to caging by anharmonic potential and fluctuations of cages, and are terminated by the primitive relaxation. Therefore the same steps leading to the magnitude and temperature dependence of the NCL in ionic conductors given above can be applied to deduce the properties of the NCL in non-ionic glassformers.

Let us now consider two non-ionic glassformers of the same family but having two different coupling parameters. For the same structural relaxation time τ_α, it follows from Eq. (3.1) that the glassformer with the larger coupling parameter has a shorter primitive relaxation time τ_0, and hence also a shorter t_{x1}. Since $< u^2 >_{\rm NCL}$ increases by the same amount in the period $t_{\rm on} < t < t_{x1}$ in the two glassformers, the magnitude of $< u^2 >_{\rm NCL}$ is inversely proportional to $[\log_e(t_{x1}) - \log_e(t_{\rm on})]$. Thus, under the condition of isochronal α-relaxation, the glassformer having larger n is predicted to have larger $< u^2 >_{\rm NCL}$. If the glass transition temperature T_g of all glassformers is defined uniformly to be the temperature at which τ_α has reached the same long time, say 10^3 s, then the prediction is larger $< u^2(T_g)_{\rm NCL}$ for glassformer having larger n. This prediction is supported by experimental data of mean-square displacement in various glassformers obtained from neutron scattering by spectrometers of the same frequency resolution shown in the left panel of Fig. 248 and by other spectroscopies in Figs. 249 and 250. Although the vibrational contribution has not been subtracted off from $< u^2(T) >$, it can be inferred from the data of polymers in the main part of Fig. 248 that $< u^2(T_g) >_{\rm NCL}$ increases in ascending order from PIB, *cis*-PB, aPP, and PS. This trend correlates with the corresponding increase of n at T_g from 0.45 for PIB, 0.50 for *cis*-PB, 0.60 for aPP, and 0.64 for PS [112, 165]. The same holds for the data from IN6 in the inset of Fig. 248, with B_2O_3 having the smallest n equal to 0.40 [112] and polycarbonate the largest $n = 0.65$. The IN10 and IN16 data in the right panel of Fig. 248 as well as the IN13 data in the inset tell the same story. The inset compares $< u^2(T) >$ data of glycerol, which has $n = 0.29$ [195], with that of OTP, which has $n = 0.50$ (from dielectric relaxation) or 0.45 (from photon correlation spectroscopy), and it can be seen that $< u^2(T_g) >$ of OTP is significantly larger than that of glycerol.

3.2.11 A Problem Related to Glass Transition: Breakdown of Thermorheological Simplicity and Associated Viscoelastic Anomalies in Polymers

Any theory of glass transition should be applicable to amorphous polymers because the phenomena are no different from other classes of glassformers as shown here and there in Chapter 2. In addition to structural relaxation and JG secondary relaxation, polymers have slower relaxation (viscoelastic) mechanisms involving longer length

scales up to the entire chain length. The relationship between the structural relaxation and these other relaxation modes is a basic problem in polymer viscoelasticity. This is because of the presence of several viscoelastic anomalies throughout the viscoelastic spectrum, which become more prominent when temperature is lowered towards T_g, suggesting relation to glass transition. Some of these anomalies have been discussed in Section 2.2.5.9. There, the purpose is to show that the degree in their manifestation is governed by or dependent on the characteristic of the structural (local segmental) relaxation, including its width of the dispersion (or n), which in turn depends on the chemical structure of the repeat unit. The reader is just reminded in here of these viscoelastic anomalies and the fact that they are caused by the structural (local segmental) relaxation of the polymer, and hence are related to the glass transition problem. We have already said that any viable theory of glass transition must be general enough to be applicable to polymers. Moreover, it should be able to explain the breakdown of thermorheological simplicity and associated viscoelastic anomalies near T_g, because these are caused by the rapid increase of the relaxation time of the structural relaxation with decreasing temperature toward vitrification, which is the core of the glass transition problem.

Before closing this section, we discuss an apparent conundrum encountered [1582] and also an invalid explanation [1761, 1762] offered by other researchers in recent consideration of the difference in the temperature dependences of the local segmental relaxation time τ_α and the viscosity η, or the temperature dependence of their shift factor $a_{T,\alpha}$ and $a_{T,\eta}$ of polymers.

3.2.11.1 A Conundrum

Polyethylene (PE) is a very flexible carbon backbone polymer, and its viscosity and $a_{T,\eta}$ have Arrhenius temperature dependence instead of the VFTH dependence. The viscosity of high molecular weight polyethylene (PE) was discussed in Section 3.2.5.2 and results given in Tables 3.4 and 3.5. The Arrhenius temperature dependence of η has activation enthalpy $E_A = 6.4$ kcal/mol or 26.8 kJ/mol [833]. On the other hand, ^{13}C-NMR measurements of unentangled polyethylene, $C_{44}H_{90}$, and another one with $M_w = 2150$ in the nanosecond range by Qiu and Ediger [1582] found that the local segmental relaxation is best described by an exponential correlation function $\exp(-t/\tau_\alpha)$, and τ_α has an Arrhenius temperature dependence with activation enthalpy $E_{A,\alpha}$ equal to 4 kcal mol or 16.7 kJ/mol. Similar value of 14.8 kJ/mol for activation energy of conformational transitions in PE was obtained by Boyd et al. [1581]. Evidently, $E_{A,\alpha}$ is less than $E_{A,\eta}$, showing once more that the temperature dependences of $a_{T,\alpha}$ and $a_{T,\eta}$ are different. Their own result from PE posed a problem for Qiu and Ediger [1582], who were led to make the drastic conclusion: "The activation energy for the conformational dynamics was found to be 4 kcal/mol, which is significantly less than the flow activation energy. Therefore, in contrast to some other well-studied examples, conformational transitions are not the fundamental motions for flow in polyethylene." The result also creates a conundrum for us because it is opposite to the stronger T dependence of $a_{T,\alpha}$ than that of $a_{T,\eta}$ found by mechanical (shear creep) measurements in high molecular weight PS,

PVAc, and atactic poly(propylene) and explained by the CM equations (2.59) and (2.65) in Section 2.2.5.9.

The conundrum can also be resolved by the CM as follows. In contrast to the mechanical measurements at times longer than 0.1 s and temperatures near T_g, the ^{13}C-NMR experiment was carried out at short times of the order of nanosecond. From the exponential correlation function $\exp(-t/\tau_\alpha)$ observed by ^{13}C-NMR, it is clear that $n_\alpha \approx 0$ for the local segmental relaxation at the short time range. Therefore from Eq. (1.59) now with $n_\alpha \approx 0$, the measured activation energy of 4 kcal/mol by the ^{13}C-NMR experiment should be close to the primitive activation energy $E_a \approx 3.6$ kcal/mol deduced in Section 3.2.5.2, or the potential energy barrier of 3.5 kcal/mol (14.8 kJ/mol) for conformational transition in bulk polyethylene obtained by molecular dynamics simulation [1581]. Moreover, 4 kcal/mol can be explained by the CM with $E_a = 3.6$ kcal/mol and $n_\alpha = 0.1$. On the other hand, the entanglement coupling parameter $n_\eta \approx 0.40$ does not change with temperature because the chains are always entangled, and hence from Eq. (1.65), $E_{A,\eta} = E_a/(1 - n_\eta) = 6.4$ kcal/mol. This is the reason why $E_{A,\eta}$ is *larger* than the activation energy for the conformational dynamics determined by the ^{13}C-NMR experiment. The conundrum is resolved. The conformational transition is still the fundamental motions for flow in polyethylene, albeit many-chain relaxation caused by entanglement interaction slows down the flow and enhances its activation energy $E_{A,\eta}$ over and above E_a of the conformational transition.

3.2.11.2 Problems Encountered in an Explanation of the Breakdown of Thermorheological Simplicity

Although the breakdown of thermorheological simplicity discovered by Plazek and coworkers and confirmed by others to be general phenomenon, solution of the problem was largely put aside by the polymer physics research community. Since the phenomenon occurs when temperature is approaching T_g and it involves the structural relaxation, there is every reason to believe that it has strong connection to the glass transition problem. This connection is innate in the CM explanation [206, 209, 837, 868–872]. Despite the fundamental nature of the problem, the CM is the one and only theoretical attempt that both addresses the glass transition problem and has given an explanation of the various breakdowns of thermorheological simplicity and associated viscoelastic anomalies of entangled and unentangled polymers. In contrast, the reptation theory of viscoelasticity of polymers neither touches the glass transition problem nor offers explanation for the viscoelastic anomalies. Other theories and models of glass transition made no effort to solve the viscoelastic anomalies either. This challenge is largely ignored by the majority of the research community. However there are still many colleagues who recognized the importance of this fundamental problem in polymer viscoelasticity. One notable person is the late Prof. John D. Ferry, who discussed this problem in his textbook *Viscoelastic Properties of Polymers*, 3rd ed. [29]. He gave me much needed encouragement to tackle the problem during my visit to the University of Wisconsin in 1992, and thereafter. After Don Plazek and I finished writing a draft of the review on the viscoelastic anomalies of polymers [165], we sent it to Prof. Ferry for his comments before submitting

it for publication. He sent us back valuable comments to improve the review, and the most memorable one is his suggestion of the title of the review *Identification of Different Modes of Molecular Motion in Polymers That Cause Thermorheological Complexity* [165]. It is most appropriate for the review and we used it exactly as he suggested.

Among other researchers who recognized the fundamental importance of the viscoelastic anomalies to both viscoelasticity of polymers and glass transition are Sokolov and Schweizer. I thank them for reviving interest of this fundamental problem to the research community by offering their own explanation [1761]. They recognized the connection of the breakdown of thermorheological simplicity to the glass transition problem and proposed the weaker temperature dependence of relaxation times of chain modes compared with local segmental relaxation, in their own words, as follows: ". . .. decoupling of the temperature dependence of the local and chain scale relaxation times in polymer liquids is the combined consequence of heterogeneous dynamics on the nanometer segmental scale and the diffusive nature of macromolecular relaxation for which heterogeneities are temporally and spatially averaged out. This idea provides an explanation for the long-standing puzzle of the breakdown of time-temperature superposition in polymer melts." "The underlying qualitative idea is that chain relaxation is a mean-field process in the sense that heterogeneous dynamics and local chain stiffness effects are (largely) averaged over, in contrast to nanometer-scale segmental relaxation."

Unfortunately, the explanation proffered by SS is not viable for several reasons [1762]. The temperature dependence of the chain dynamics coming from temporal and spatial averaging of the heterogeneous segmental dynamics, suggested by Sokolov and Schweizer (SS), is no different from the effective friction factor of the averaged segmental dynamics. In other words, the observed segmental dynamics is also an average over its temporal and spatial heterogeneities, and thus the friction factor of its averaged relaxation time $< \tau_\alpha >$ has the same temperature dependence as that obtained by the averaging performed for the chain modes suggested by Sokolov and Schweizer. The anomaly remains unexplained.

There are other problems in the explanation given by SS. One is posed by the viscosity η and self-diffusion coefficient D data of high molecular weight PE and HPB discussed in Section 3.2.5.2. According to the averaging proposed by SS, they should have the *same* chain friction obtained by averaging out the spatially heterogeneous dynamics of the local structural relaxation, but this is contradicted by experiments showing that η has higher activation energy than D (see Table 3.4). The explanation of SS rests on the assumption that the decoupling of translational and reorientational motions in *non-polymeric* liquids is due to heterogeneity of the local dynamics. However, for three well-known cases of such decoupling, *o*-terphenyl [456], tris(naphthyl)benzene [455, 820, 821], and sucrose benzoate [457], the distribution of relaxation times is unchanged with variation in temperature over the range of T/T_g from about 1.02 to 1.2. As acknowledged by Mapes et al. [454]: "The dielectric relaxation and photon correlation spectroscopy results imply a relaxation time distribution whose shape is too temperature independent to cause [translational-rotational decoupling], at least within the framework of

current approaches." Thus dynamic heterogeneity fails to explain even the decoupling of viscosity from self-diffusion in non-polymeric glassformers. Lest the reader forgets, a viable explanation of this has been given by the CM [797]. The point herein is that it is premature for SS to explain a second phenomenon using an explanation that does not yet satisfactorily account for the first phenomenon. Next, SS support their ansatz by its consistency with "the almost universal behavior of the temperature dependence of chain relaxation" [1762]. This universal behavior is the putative equivalence of the T_g-normalized temperature dependence (fragility) of the viscosity η or global relaxation time τ_c for all polymers. However, with the exception of polystyrenes of different molecular weights (wherein temperature dependences of low molecular weight samples reflect contributions from a changing compliance and the sub-Rouse modes), in addition to the usual friction factor [832], the fragility of the chain dynamics of polymers differs substantially as shown in [1763]. Thus, while coarse averaging of T_g-normalized temperature dependences can yield single curves with large error bars (Fig. 3b in [1761]), the data points per se exhibit substantial scatter. For example, the ordinate value of a fragility plot of τ_c poly(vinyl ethylene) is more than twice that of poly(methylphenylsiloxane) at $T_g/T \sim 0.92$; there is a similar difference between polyisobutylene and polystyrene at $T_g/T \sim 0.95$ [1763]. Other examples can be cited; there is no universal behavior.

In spite of the shortcomings of the explanation from SS, they are commended for their recognition of the importance of this fundamental and valiant attempt to solve it.

3.2.12 Looking Out for Universal Dynamics in Other Complex Interacting Systems

Demonstrated in the preceding subsections of this chapter, similar relaxation and diffusion dynamics are shared by diverse interacting systems. Among the systems exhibiting similar dynamics, the class of glassformers is the most intensively and extensively studied, and has by far the most examples to support universal properties. But even the lesser systems discussed before, there are sufficient experimental studies to provide evidence of similar properties. All the results suggest universality of relaxation and diffusion in interacting systems. Therefore, it is a worthwhile pursuit to look for universal dynamic properties in other interacting systems that have not been either explored or attracted enough attention. This pursuit can bring tremendous benefits to any of these systems because the dynamic properties particularly the anomalous ones can be immediately understood or explained by the knowledge gained from the better known systems. Caution must be exercised when considering complex interacting systems possessing extraneous factors to complicate the observed dynamics and obscure the vestige of the universal many-body relaxation. The contributions from the extraneous factors such as multicomponents and spatial heterogeneity have to be separated or removed before the universal dynamics can be revealed. Before closing this chapter, we give two examples of such complex interacting systems that show features in the dynamics resembling those of glassformers.

3.2.12.1 Charge Density Wave Systems

The system is the modulated electronic superstructure called charge-density wave (CDW) that appears in some quasi-one-dimensional materials such as $K_{0.3}MoO_3$ and orthorhombic TaS_3 at low temperatures [1764–1770]. The first evidence of glass state in CDW systems have been found in the heat capacity C_p measurements at low temperature [1765] showing up as the excess contribution above the Debye contribution from vibrations, $C_p \sim T^3$, like in glasses related to the Boson peak in susceptibility found at high frequencies.

CDW is electronic in origin and far flung from any of the systems discussed before. The first indication of similarity of dynamics in CDW to glassformers was put forth by Kriza and Mihály in 1986 [1766] including the stretched exponential dielectric relaxation they observed in $K_{0.3}MoO_3$ and the connection with the CM. More striking resemblance of dynamics with glassformer was found by Starešinić et al. from dielectric relaxation measurements of semiconducting CDW systems in orthorhombic TaS_3 [1768] and $K_{0.3}MoO_3$ [1769]. They found two relaxations α and β in the dielectric loss spectra (see the example for TaS_3 in the left panel of Fig. 322) and also in thermally stimulated current spectra of *o*-TaS_3 and $K_{0.3}MoO_3$ (right panel of Fig. 322).

The relaxation time τ_α of the α-process increases rapidly with decreasing temperature and reaches very long time at some temperature T_g (see left panel of Fig. 323) like structural relaxation of glassformers undergoing glass transition. The relaxation time τ_β of the faster β-relaxation changes T dependence near T_g to assume an Arrhenius dependence at temperatures below T_g, resembling the behavior of the JG β-relaxation of glassformers. Starešinić and Biljaković [1771] explained their results by the model of cooperatively relaxing CDW domains of coherent phase

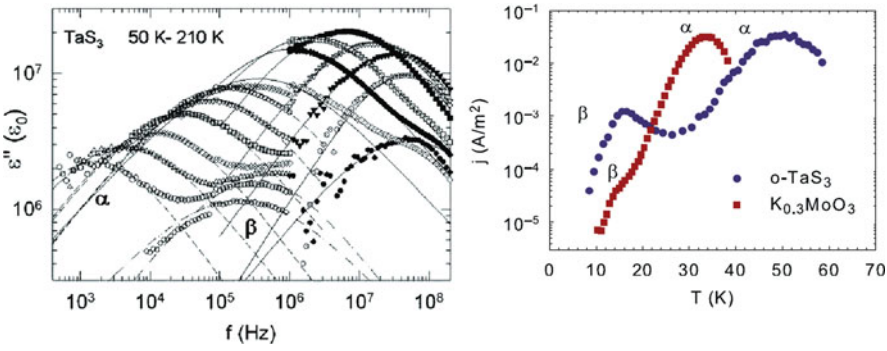

Fig. 322 (*Left*) Imaginary part ϵ'' of the dielectric function of orthorhombic TaS_3 as a function of frequency at several temperatures. The *lines* represent single-process Cole–Cole fits of the dielectric loss data for $T > 50$ K. The *solid lines* correspond to the α-process above 1 MHz, the *dashed lines* to the α-process below 1 MHz, and the *dash-dotted lines* correspond to the β-process seen below 60 K. Reproduced from [1768] by permission. (*Right*) Thermally stimulated current spectra of *o*-TaS_3 and $K_{0.3}MoO_3$. The sample is cooled in the external electric field and heated in short-circuit configuration and the depolarization current is recorded. Maxima correspond to the "melting" of frozen relaxation processes. Reproduced from [1770] by permission

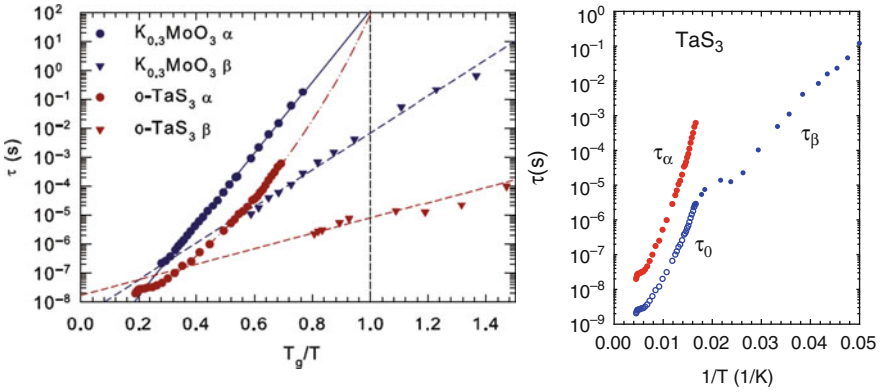

Fig. 323 (*Left*) Characteristic relaxation times τ_α and τ_β of the α and β processes in CDW systems *o*-TaS_3 and $K_{0.3}MoO_3$ as a function of the inverse temperature normalized to the glass transition temperature T_g. T_g is 42 K for *o*-TaS_3 and 23 K for $K_{0.3}MoO_3$. *Full line* represents the activated increase of τ_α in $K_{0.3}MoO_3$ and *dash-dotted line* the Vogel–Fulcher increase of τ_α in *o*-TaS_3. *Dashed lines* represent the activated increase of τ_β in both systems. Reproduced from [1770] with permission. (*Right*) Data of τ_α and τ_β in *o*-TaS_3 (*filled circles*, same as in the *left panel*). The *open circles* are the primitive relaxation time τ_0 in *o*-TaS_3 calculated by Starešinić and Biljaković (unpublished) using the CM relation with the parameters given in the text

coupled through electrostatic interaction. At lower temperatures, in the absence of free carrier screening, this causes slowing down and subsequent freezing of the elastic degrees of freedom, i.e., the α-process. The β-process represents the dynamics of topological defects developed on the domain boundaries. They used the CM relation to calculate the primitive relaxation time τ_0 from the experimental values of τ_α of TaS_3 by using the CM equation $\tau_0 = (t_c)^n(\tau_\alpha)^{1-n}$. They obtained an approximate value of $(1 - n) = 0.67$ from the spectra and took $t_c = 2 \times 10^{-11}$ s, the reciprocal of the real pinning resonance frequency, because above this frequency, CDW is depinned. The calculated values of τ_0 shown in the right panel of Fig. 323 are in agreement with τ_β. Despite the progress made by Starešinić, Biljaković, and coworkers [1768–1770] in the dynamics of CDW system through the analogy to glassformers and the possible connection to the CM, more study has to be made before we can arrive at a full understanding.

3.2.12.2 Aqueous Colloidal Dispersions of Magnetic Nanoparticles

The nanometric magnetic particles dispersed in water have many applications in technology [1772, 1773] and are also systems of fundamental interest as interacting hard spheres in which the inter-particle interactions can be tuned by varying external parameters. One class of these colloidal dispersions is constituted of chemically stable nanocrystals of γ-Fe_2O_3 oxidized in maghemite with diameter of about 10 nm or less dispersed in water and stabilized by electrostatic repulsion [1773]. The last step was achieved by coating the surface of the nanoparticles with citrate molecules,

which ensures a negative charge at neutral pH, compensated by sodium counterions. The inter-particle interactions can be continuously tuned by varying the osmotic pressure π through the ionic strength [1774]. With the ionic strength held constant, the viscosity increases with the volume fraction Φ until the samples no longer flow, and the state was referred to as the "macroscopic solid."

Each particle bears a dipole moment $\mu(\sim 10^4\,\mu\mathrm{B})$ and an uniaxial optical anisotropy linked to μ through the magnetic energy of anisotropy of the nanocrystal. In a fluid dispersion, without field, the crystal axes are oriented at random and no optical birefringence is observed. The orientation of the particles via their magnetic moment under an applied field induces a magnetobirefringence Δn in the solution due to the mechanical orientation of the nanoparticle axes. The rotational relaxation of the nanoparticles was studied by the relaxation of the magneto-induced birefringence signal. Indeed, the birefringence response of the suspension to a small external field pulse is a transient orientation followed by a relaxation to a randomly orientated state. If the sample is monodisperse and dilute (independent particles), the relaxation of the birefringence is well described by a linear exponential decay according to Perrin [12] with the relaxation time $\tau_\mathrm{R} = 3\eta V_\mathrm{H}/kT$, where η is the solvent viscosity and V_H the hydrodynamic volume of the particle. The samples studied by Mériguet et al. [1775, 1776] were polydisperse, and polydispersity induces a distribution of the τ_R, and hence departure from the ideal single exponential decay is observed even for dilute dispersion. For a dilute dispersion of particles with a volume fraction close to $\Phi \sim 0.01$ with a mean diameter of 7 nm, a relaxation time of $\tau = 4\,\mu\mathrm{s}$ was measured. Because of polydispersity ($\sigma = 0.35$) of the sample, the relaxation function is not a single exponential. This can be seen in the right panel of Fig. 324 at low Φ. The data for all Φ are shown in Figs. 324 and 325. On the left panel of Fig. 324 are the normalized optical intensity $I(t)/I_0$ for citrate concentrations of 0.03 mol l^{-1} at increasing volume fraction of nanoparticles. The right panel of Fig. 324 shows the decrease of the Kohlrausch stretch exponent $\alpha \equiv (1-n)$ vs. normalized volume fraction Φ/Φ^*, where $\Phi^* = 0.18$.

On increasing Φ, the relaxation is slowed down. Up to a volume fraction of 11%, the relaxation function and the relaxation time depend weakly on Φ. On further increase of Φ, a dramatic slowing down was observed by the stretching of the relaxation function to longer times (see Fig. 324) and the rapid increase of the relaxation time τ_2 (see left panel of Fig. 325). This occurs before the macroscopic solidification of the sample. The decay of the optical intensity was well fitted by a sum of a single exponential accounting for the short-time relaxation and a stretched exponential of Kohlrausch for the long-time behavior:

$$I(t) = I_1 \exp\left(-\frac{t}{\tau_1}\right) + I_2 \exp\left[-\left(\frac{t}{\tau_2}\right)^{1-n}\right],$$

where $I_1 + I_2 = I_0 = I(t=0)$. The reader may recall this time dependence of the correlation function is the same as in other systems including the aqueous colloidal

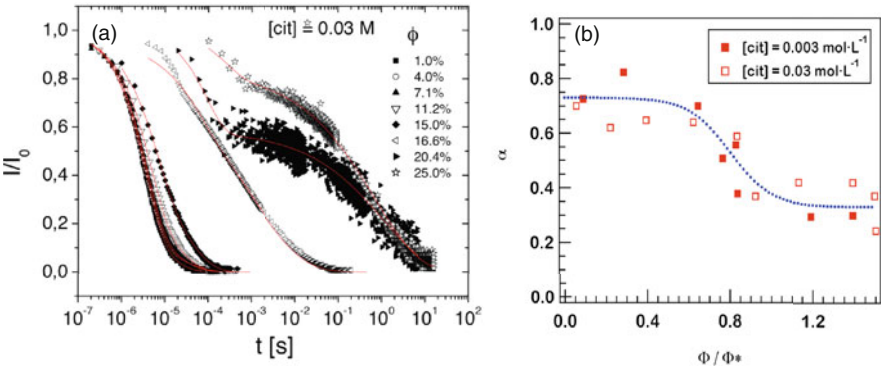

Fig. 324 (*Left*) Normalized optical intensity $I(t)/I_0$ for citrate concentrations of 0.03 mol/l at increasing volume fraction of nanoparticles. Here ϕ is Φ expressed as percentage. (*Right*) Variation of the Kohlrausch stretch exponent $\alpha \equiv (1 - n)$ vs. normalized volume fraction Φ/Φ^*, where $\Phi^* = 0.18$. The *dotted line* is guide to the eyes. Reproduced from [1775] by permission

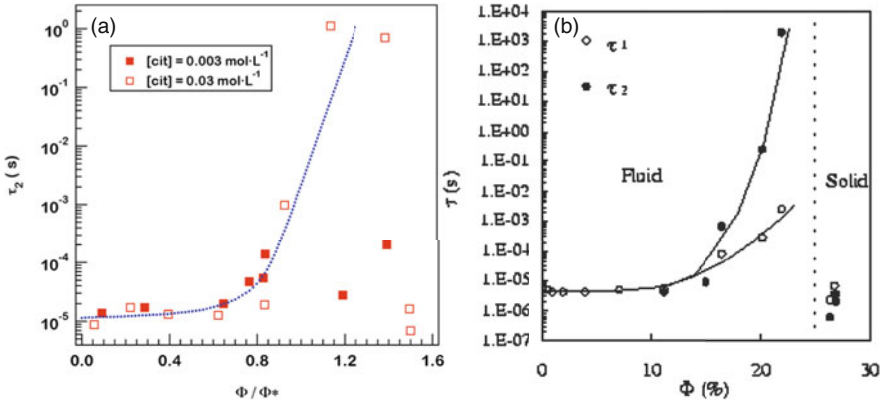

Fig. 325 (*Left*) Variation of the relaxation time τ_2 with the normalized volume fraction Φ/Φ^*, where $\Phi^* = 0.18$. Reproduced from [1775] by permission. (*Right*) Variation of the relaxation times τ_1 and τ_2 with the volume fraction Φ. Reproduced from [1776] by permission

suspensions of a synthetic clay, Laponite (see Section 2.3.2.39), and in associating or aggregating polymers solutions in Section 3.2.3.6.

The exponent $\alpha \neq (1 - n)$ of the stretched exponential exhibits a significant decrease starting near the same $\Phi/\Phi^* = 1$ (Fig. 324), where the relaxation time τ_2 also shows the rapid increase (left panel of Fig. 325). This is another example of the correlation between the width of the dispersion (or n) and the relaxation time found in many cases discussed before including the aqueous colloidal suspensions of Laponite and the associating or aggregating polymers solutions. The right panel of Fig. 325 shows variation of both the relaxation times τ_1 and τ_2 with the volume fraction Φ. It can be seen that the separation between the two relaxation times

increases as n increases with Φ. Again this trend is found in many other interacting systems.

A more recent paper by Wandersman et al. of the same group [1777] studied the freezing of the orientational degrees of freedom of strongly interacting magnetic and charged nanoparticles by magneto-induced birefringence measurement, as the colloidal glass transition is approached. Using a magneto-induced birefringence technique, they show that the rotational dynamics drastically slows down following a modified Vogel–Fulcher law with the volume fraction Φ replacing T, for Φ above a threshold, the value of which depends on the range of electrostatic repulsion between nanoparticles. The birefringence measurement provides the time correlation of the orientational degrees of freedom of the the nanoparticles, which is given by $C_2(t) =< P_2(\vec{e}_i\ (t) \cdot\ \vec{e}_i\ (0)) >$, where P_2 is the second Legendre polynomial and $\vec{e}_i$ is the direction of the optical axis of the ith nanoparticle. For dilute ferrofluids, the magneto-induced birefringence relaxations are nearly exponential. The relaxation becomes increasingly more non-exponential and stretched to longer times on increasing volume fraction, but at short times it remains exponential component. For this reason, the time dependence of the relaxation was fitted by the function $A\exp(-t/\tau_1) + (1-A)\exp[-(t/\tau_2)^{1-n}]$, like the earlier study by Mériguet et al. [1775, 1776]. The data are shown in Fig. 326 (left). In the fitting process, A, τ_2, and $(1-n)$ are treated as fitting parameters, while the short characteristic time τ_1 is assumed to be constant and set equal to its value at low volume fraction. This latter assumption is different from that of [1776], where τ_1 increases with volume fraction as shown in Fig. 325 (right). The changes of the fitting parameters τ_2 and $(1-n)$ with the volume fraction are reproduced from [1777] in Fig. 326 (right).

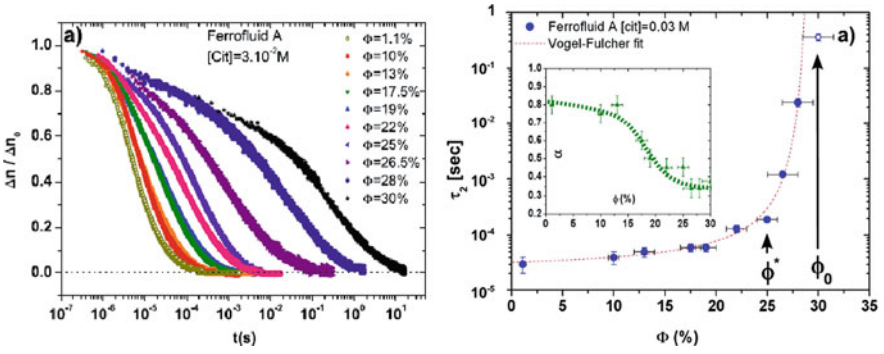

Fig. 326 (*Left*). Normalized birefringence relaxations of ferrofluids A at different volume fractions Φ increasing from left to right. The initial time $t = 0$ is defined when the magnetic field is cut off. (*Right*) Rotational characteristic time τ_2 extracted from the fit of birefringence relaxations as a function of the volume fraction Φ. The *open symbol* is the sample at volume fraction $\Phi = 30\%$ for which no stationary birefringence can be reached after a pulse of magnetic field. The *dashed line* is a Vogel-Fulcher fit of the data. *Inset*: Evolution of the stretched exponent $\alpha \equiv (1-n)$ as a function of the volume fraction. The *dotted line* is a guide for the eye. Reproduced from Ref. [1777] by permission.

Despite the assumption in fitting the data in [1777] that is different from that in [1775, 1776], both experiments essentially show the same universal features of relaxation in other interacting systems. There are more interacting systems exhibiting the universal properties but are not discussed in this volume.